Perturbed KdV equations and their integrability properties

TER-BRAAK, FLORIS

Perturbed KdV equations and their integrability properties

Floris ter Braak

A Thesis presented for the degree of
Doctor of Philosophy

Department of Mathematical Sciences
Durham University
United Kingdom

March 2018

Perturbed KdV equations and their integrability properties

Floris ter Braak

Submitted for the degree of Doctor of Philosophy

March 2018

Abstract: In this thesis we investigate the integrability properties of the regularized long-wave (RLW) equation and modified regularized long-wave (mRLW) equation as perturbations of the integrable Korteweg-de Vries (KdV) equation. We study various properties of numerical mRLW three-soliton scattering and compare these with the corresponding RLW soliton solutions. We find that the numerical mRLW solitons behave much like integrable solitons in the sense that the only result of the three-soliton interaction is the phase shift each soliton experiences, which is approximately equal to the sum of pairwise phase shifts. Furthermore, we investigate the so-called quasi-integrability properties of these RLW and mRLW simulations. Using both analytical and numerical methods, we argue that these models possess an infinite amount of asymptotically conserved charges, i.e., quasi-conserved charges, which are observed in multi-soliton interactions. Finally, we also simulate numerical RLW and mRLW solutions in the presence of additional perturbing terms. This allows us to study soliton-radiation interactions and we find that for certain perturbations, these interactions preserve the quasi-conservation laws to a certain extend.

Declaration

The work in this thesis is based on research carried out in the Department of Mathematical Sciences at Durham University. No part of this thesis has been submitted elsewhere for any degree or qualification. The work presented in this thesis is partially based on two papers, one in collaboration with W. J. Zakrzewski and one in collaboration with L. A. Ferreira and W. J. Zakrzewski. To be specific, subsection 1.3.3, chapter 2 and chapter 6 are based on [4], and chapters 3 and 4 are based on [5]. I collaboratively investigated the results presented in chapter 2, developed the algorithm presented in chapter 3, and executed all the numerical calculations presented in chapters 4 and 6. Furthermore, I played a key role in the interpretation of these numerical results under the supervision of W. J. Zakrzewski and with the help of L. A. Ferreira.

Acknowledgements

This thesis would not have been possible without the support of my supervisor Prof Wojtek Zakrzewski. From suggesting the topic of this thesis and helping me solve the seemingly unavoidable computational problems one encounters when doing numerical work, to having fascinating conversations about the history of Eastern Europe, I, first and foremost, want to thank Wojtek for his supervision during my PhD.

Through Wojtek, I had the opportunity to meet and work with Prof Luiz Ferreira. His sharp insights in the topic of quasi-integrability have been immensely important for the work presented in this thesis. I would like to thank him for this and for introducing me to the more mathematical aspects of quasi-integrability.

I would like to thank my parents for their encouragement during this adventure. I am grateful for their unconditional support. The way in which my father has developed an interest in physics, and in my subject in particular, has meant a lot to me. My mother's encouragement to embark on this journey has been invaluable.

I am also grateful to Alex for helping me set up the Mira service in order to run large simulations, and he has guided me in the right direction to learn C++.

Lastly, but not least, I am grateful to Natasha for the help she has given me whenever I struggled with English grammar.

Contents

Chapter 1

Introduction

1.1 The perturbed KdV equation

The aim of this thesis is to investigate various aspects of the following nonlinear partial differential equation (PDE)

$$u_t + u_x + \left[\frac{\alpha}{2}u^2 + \varepsilon_2\frac{\alpha}{4}w_x v_t + u_{xx} - \varepsilon_1(u_{xt} + u_{xx})\right]_x = 0\,, \tag{1.1.1}$$

where the subscripts x and t denote partial differentiation with respect to position and time, the field $u = u(x,t)$ is a real-valued function, and w and v are antiderivatives of the u-field, defined by

$$u = w_t = v_x\,. \tag{1.1.2}$$

Furthermore, $\alpha \in \mathbb{R}$ is a scaling parameter, and $\varepsilon_1, \varepsilon_2 \in \mathbb{R}$ are perturbation parameters.

When $\varepsilon_1 = \varepsilon_2 = 0$, equation (1.1.1) reduces to the Korteweg-de Vries (KdV) equation [19]

$$u_t + u_x + \left[\frac{\alpha}{2}u^2 + u_{xx}\right]_x = 0\,. \tag{1.1.3}$$

The standard form of the KdV equation can be recovered by setting $\alpha = 6$ and letting $u = -\bar{u} - \frac{1}{6}$, that is,

$$\bar{u}_t - 6\bar{u}\bar{u}_x + \bar{u}_{xxx} = 0\,. \tag{1.1.4}$$

One of the interesting properties of the KdV equation is that it admits analytical N-soliton solutions for any positive integer N [14], where solitons are defined as localised waves that scatter elastically, and preserve their shape and velocity asymptotically. As we will discuss in more detail below, the KdV soliton solutions exist because the model gives rise to an infinite number of conservation laws, which is closely related to the concept of integrability.

If we set $\varepsilon_1 = 1$ and $\varepsilon_2 = 0$, then equation (1.1.1) reduces to

$$u_t + u_x + \left[\frac{\alpha}{2}u^2 - u_{xt}\right]_x = 0\,, \tag{1.1.5}$$

which is known as the regularized long-wave (RLW) equation [2, 24]. This equation plays an important role as a model in many areas of physics and the study of nonlinear dispersive waves. One advantage of the RLW equation is that it has a linear dispersion relation that is better posed than the dispersion relation for the KdV equation; the phase velocities of RLW solitons with a large wavenumber tend to zero, whereas KdV solitons with a large wavenumber propagate with negative and unbounded velocities. On the other hand, this is a nonintegrable model that admits only one-soliton solutions [6]. Furthermore, this model has only exactly three conserved charges [23], given by

$$Q_1^{\mathrm{RLW}} = -\frac{\alpha}{2}\int_{-\infty}^{\infty}\mathrm{d}x\, u\,, \tag{1.1.6}$$

$$Q_2^{\mathrm{RLW}} = -\frac{\alpha^2}{2}\int_{-\infty}^{\infty}\mathrm{d}x\, \left(u_x^2 + u^2\right)\,, \tag{1.1.7}$$

$$Q_3^{\mathrm{RLW}} = \frac{\alpha^2}{2}\int_{-\infty}^{\infty}\mathrm{d}x\, \left(\frac{\alpha}{3}u^3 + u^2\right)\,. \tag{1.1.8}$$

These charges correspond, respectively, to the mass, momentum and Hamiltonian of the RLW equation.

Equation (1.1.1) corresponds to the modified regularized long-wave (mRLW) equation [15] when $\varepsilon_1 = \varepsilon_2 = 1$, that is,

$$u_t + u_x + \left[\frac{\alpha}{2}u^2 + \frac{\alpha}{4}w_x v_t - u_{xt}\right]_x = 0\,. \tag{1.1.9}$$

The mRLW equation has similar properties as the RLW equation because they admit the same family of single-soliton solutions with the same short wavelength properties. However, the difference between the two models is that the mRLW equation also admits analytic two-soliton solutions. Another difference is that no Hamiltonian structure has been found for this system, and its only known conservation laws are given by

$$Q_1^{\mathrm{mRLW}} = \int_{-\infty}^{\infty} \mathrm{d}x\; u = -\frac{2}{\alpha} Q_1^{\mathrm{RLW}} \equiv Q_1\,, \tag{1.1.10}$$

and

$$Q_2^{\mathrm{mRLW}} = \int_{-\infty}^{\infty} \mathrm{d}x\; w_x \equiv Q_2^{\varepsilon_2}\,, \tag{1.1.11}$$

where we have assumed that u, w_x and v_t vanish sufficiently fast when $x \to \pm\infty$. In fact, note that Q_1 and $Q_2^{\varepsilon_2}$ are conserved for any $\varepsilon_1, \varepsilon_2 \in \mathbb{R}$.

To sum up, we see that equation (1.1.1) can be thought of as a family of perturbations of the KdV equation that contains the RLW and mRLW equations as special cases. The aim of this thesis is to investigate various aspects of integrability and quasi-integrability related to analytical and numerical solutions of this equation. Integrability in the context of nonlinear PDEs often manifest itself in the properties of their (soliton) solutions. These general concepts will be discussed in the remaining part of this chapter. Furthermore, using Hirota's method, we obtain analytical soliton solutions of the perturbed KdV equation that are valid only for certain values of ε_1 and ε_2, and we discuss some of their properties. Finally, we introduce the (relatively new) concept of quasi-integrability.

In chapter 2, we use analytical methods to investigate the quasi-integrability aspects of the perturbed KdV equation. We introduce Lax potentials that give rise to a so-called 'anomalous' zero curvature equation. Using this curvature, we generate quantities that are potentially quasi-conserved. In fact, for the special case of the mRLW two-soliton solutions, we prove that the charges are indeed quasi-conserved. To our knowledge, this is the first analytic proof of quasi-integrability in the context of exact two-soliton solutions. In the last two sections of the chapter, we analyse

the quasi-integrability aspects of solutions that are an expansion around some exact KdV solution that satisfies special symmetry properties.

In chapter 3, we introduce two finite difference schemes in order to approximate the perturbed KdV equation. The first scheme that we discuss is first-order accurate in time and second-order in space, whereas the second scheme is second-order accurate in both space and time. We compare various numerical simulations with the corresponding analytic values to test the accuracy and stability of the schemes. The results show that the first-order scheme is unstable. The second-order scheme, on the other hand, appears to be stable and give reliable results.

We use the second-order scheme to simulate multi-soliton solutions governed by the RLW and mRLW equations. These results will be discussed in chapter 4. We test the stability of these solutions by checking for visible loss of radiation. Furthermore, we determine the phase shift of the numerical solitons during two- and three-soliton interactions. Finally, we test the soliton resolution conjecture for both models to further investigate their stability properties.

In chapter 5, we investigate the numerical (multi-)soliton solutions in the presence of perturbing terms. We investigate this for both the RLW and mRLW one-, two- and three-soliton solutions. We check if these systems are stable or if they blow up. Furthermore, by analysing multi-soliton interactions, we can see how the stable soliton-like components of the initial conditions interact with the other soliton- and radiation-like components.

For the next chapter, we numerically analyse the quasi-integrability properties of the simulations presented in chapters 4 and 5. This is the first time, to our knowledge, that the quasi-integrability properties of numerical three-soliton solutions are investigated. Furthermore, we find that for certain perturbations, the interactions between soliton-like and radiation-like components also appears to preserve quasi-integrability.

In our final chapter, we sum up our results. Furthermore, we discuss various aspect that we think are interesting and fruitful to research in the future. Finally,

in the appendix, we summarise the parameters that we used for all the simulations presented in this thesis.

1.2 Integrability

Although there is no universally accepted definition of integrability, we will refer to a system as completely integrable if it has infinite many non-trivial conserved quantities that are in involution with respect to each other. The KdV equation is an example of a completely integrable model [10].

An important feature of complete integrable models is that they admit N-soliton solutions for any positive integer N. Furthermore, for a given N-soliton solution, the infinite amount of conservation laws prevent the creation or destruction of any solitons and ensure that the set of outgoing solitons regain the shape and velocity of the incoming solitons. In fact, the only result of the scattering of integrable solitons is the phase shift each soliton experiences. Furthermore, when more than two solitons interact with each other at the same time, the total phase shift each soliton experiences is the sum of pairwise phase shifts [22]. This is due to the absence of 'many-particle' effects.

Note that some nonintegrable models also admit (multi-)soliton solutions. However, they do not admit analytical N-soliton solutions for any positive integer N. Numerical investigations have shown that these nonintegrable solitons are often less stable in the sense that when they are perturbed, their amplitudes might continuously increase until the system blows up, or their amplitudes might continuously decrease while simultaneously emitting radiation. On the other hand, when integrable solitons move in the presence of some small perturbation, this might cause their amplitudes and velocities to change while emitting some radiation but, asymptotically, the remaining structure will move away from the radiation without blowing up. In fact, after an integrable soliton emits its radiation, the resulting structure still looks and behaves like a soliton, albeit with a slightly different amplitude, velocity

and phase as the initial configuration [28, and references therein]. Strictly speaking, the 'soliton' solutions of nonintegrable models are solitary waves, but they are not solitons. However, as is common in the physics literature, solitary waves are also referred to as solitons, and we adopt this terminology as well.

Another remarkable property of the KdV equation is that numerical and analytical investigations have shown that any localised pulse, used as initial conditions, eventually decouples into a sum of soliton- and radiation-like structures [14, 21]. We can think of the solitons as the stable part of the initial configuration. This property has been observed for many integrable models, and is known as the soliton resolution conjecture [1, 27, and references therein].[1]

1.2.1 Zero curvature condition

The definition of integrability, as discussed in this thesis, is closely related to the so-called zero curvature equation. In this section, we discuss the zero curvature equation, and we show that when this condition is satisfied, it leads to a function that generates infinitely many conserved quantities. To this end, we consider nonlinear PDEs in $(1+1)$ dimensions, that is,

$$F(u, u_x, u_t, \cdots) = 0\,, \tag{1.2.1}$$

for some given function F. Let us now suppose the PDE admits two $N \times N$ matrices, $A_x = A_x(x,t,\lambda)$ and $A_t = A_t(x,t,\lambda)$, which depend on the field u (and its derivatives) and a spectral parameter λ, such that equation (1.2.1) is satisfied if, and only if,

$$\mathcal{F}_{tx} \equiv \partial_t A_x - \partial_x A_t + [A_t, A_x] = 0\,. \tag{1.2.2}$$

This is the zero curvature equation, where $\mathcal{F}_{tx}$ denotes the curvature, and A_x and A_t are known as the Lax potentials. This equation leads to an infinite amount of conserved quantities, as we will show below.

To this end, let us assume that u is periodic in x with period 2π. Next, we

[1] We thank A. Hone for drawing our attention to this conjecture.

introduce the monodromy matrix $T = T(t, \lambda)$, defined by

$$T = \mathcal{P} \exp\left(- \int_0^{2\pi} \mathrm{d}x \, A_x \right) , \tag{1.2.3}$$

where $\mathcal{P}$ denotes the path ordering operator. Taking the derivative with respect to time gives

$$\begin{aligned}
\partial_t T &= - \int_0^{2\pi} \mathrm{d}x \; \mathcal{P}\, e^{-\int_x^{2\pi} \mathrm{d}y \, A_x} \left(\partial_t A_x\right) \mathcal{P}\, e^{-\int_0^{x} \mathrm{d}y \, A_x} \\
&= - \int_0^{2\pi} \mathrm{d}x \; \mathcal{P}\, e^{-\int_x^{2\pi} \mathrm{d}y \, A_x} \left(\partial_x A_t - [A_t, A_x]\right) \mathcal{P}\, e^{-\int_0^{x} \mathrm{d}y \, A_x} \\
&= - \int_0^{2\pi} \mathrm{d}x \, \partial_x \left(\mathcal{P}\, e^{-\int_x^{2\pi} \mathrm{d}y \, A_x} A_t \, \mathcal{P}\, e^{-\int_0^{x} \mathrm{d}y \, A_x} \right) \\
&= -A_t(2\pi, t, \lambda) T(t, \lambda) + T(t, \lambda) A_t(0, t, \lambda) \\
&= \left[-A_t(2\pi, t, \lambda), T(t, \lambda) \right] ,
\end{aligned} \tag{1.2.4}$$

where we have used the periodicity of the field u to get to the last line. Let $\mathcal{T} = \mathcal{T}(\lambda)$ denote the trace of the monodromy matrix, that is,

$$\mathcal{T} = \mathrm{Tr}\left(T\right) . \tag{1.2.5}$$

Note that $\mathcal{T}$ is not dependent on time due to the cyclicity of trace, that is,

$$\partial_t \mathcal{T} = \mathrm{Tr}\left(\left[-A_t(2\pi, t, \lambda), T(t, \lambda) \right] \right) = 0 . \tag{1.2.6}$$

Therefore, expanding $\mathcal{T}$ generates infinitely many conserved charges. Note that the zero curvature condition is not sufficient proof for complete integrability. To make this distinction, we say a system is kinematically integrable if it can be represented as a zero curvature condition [9].

The zero curvature condition of the KdV equation described by equation (1.1.4) can be represented by

$$A_x = \begin{pmatrix} 0 & 1 \\ \lambda + \bar{u} & 0 \end{pmatrix} \quad \text{and} \quad A_t = \begin{pmatrix} \bar{u}_x & -4\lambda + 2\bar{u} \\ -4\lambda^2 - 2\lambda\bar{u} + 2\bar{u}^2 - \bar{u}_{xx} & -\bar{u}_x \end{pmatrix} \tag{1.2.7}$$

such that

$$\mathcal{F}_{tx} = \begin{pmatrix} 0 & 0 \\ \bar{u}_t - 6\bar{u}\bar{u}_x + \bar{u}_{xxx} & 0 \end{pmatrix} . \tag{1.2.8}$$

It can be shown that the charges generated by A_x are in involution, and so the KdV equation is in fact a complete integrable system [9, e.g.]. We will use the expression for A_x in the next chapter to construct the so-called anomalous curvature equation of the perturbed KdV equation.

1.3 Hirota integrability

As it turns out, for PDEs there is no definition of integrability that applies to every model. Therefore, one instead often focusses on methods that lead to soliton solutions. One technique to construct soliton solutions is known as Hirota's method (and we will, when it is important to stress this fact, refer to them as Hirota solutions). In this section, we discuss Hirota's method and how it is related to the concept of integrability. Furthermore, we construct the N-soliton Hirota solutions of the KdV equation, and we construct families of one- and two-soliton solutions that solve the perturbed KdV equation for certain values of the perturbations parameters ε_1 and ε_2.

1.3.1 Hirota's method

In this subsection, we briefly discuss the Hirota method for constructing N-soliton solutions [18, e.g.]. First, let us consider a nonlinear PDE in $(1+1)$ dimensions

$$F(u, u_x, u_t, \cdots) = 0 \,, \tag{1.3.1}$$

and define Hirota's D-operator in the following way

$$\mathrm{D}_x^n f \cdot g = (\partial_{x_1} - \partial_{x_2})^n f(x_1) g(x_2)|_{x_2 = x_1 = x} \,, \tag{1.3.2}$$

for any two functions f and g. The idea behind Hirota's method is to write u in terms of the so-called τ-function, $\tau = \tau(x,t)$, such that the nonlinear PDE can be

written as

$$P(\mathrm{D}_x, \mathrm{D}_t)\, \tau \cdot \tau = 0\,, \tag{1.3.3}$$

where P is a polynomial in the D_x and D_t operator. This expression is known as Hirota's bilinear equation. Note, however, that it is not always possible find a transformation such that the nonlinear PDE can be rewritten in Hirota's bilinear form.

To construct the soliton solutions, we express the τ-function as a power series in the expansion parameter η, that is,

$$\tau = 1 + \sum_{n=1}^{\infty} \eta^n \tau_n = 1 + \eta\tau_1 + \eta^2\tau_2 + \cdots\,, \tag{1.3.4}$$

and choose the τ_i functions appropriately. When the system under consideration admits an N-soliton solution, the series truncate in the sense that $\tau_n = 0$ for $n > N$ so that τ is defined by a finite expansion.

It turns out that if the system under consideration admits one-soliton Hirota solutions, then the corresponding τ-function will be of the form

$$\tau = 1 + \eta e^{\Gamma_1}\,, \tag{1.3.5}$$

where Γ_1 is defined by

$$\Gamma_i = k_i x - \omega_i t + \delta_i\,. \tag{1.3.6}$$

The parameter k_i denotes the wavenumber, ω_i the angular frequency and δ_i the arbitrary phase constant of each corresponding soliton.

Assuming that the system also admits two-soliton Hirota solutions, then the corresponding τ-function will be of the form

$$\tau = 1 + \eta e^{\Gamma_1} + \eta e^{\Gamma_2} + \eta^2 A_{12} e^{\Gamma_1+\Gamma_2}\,, \tag{1.3.7}$$

where A_{12} is a constant. In fact, it turns out that the τ-function for any N-soliton Hirota solution can be written as

$$\tau = \sum_{\mu_i=0,1} \exp\left(\sum_{i=1}^{N} \mu_i\Gamma_i + \sum_{i<j}^{(N)} \mu_i\mu_j \ln A_{ij}\right)\,, \tag{1.3.8}$$

where the first summation is over all possible combinations of

$$\mu_1 = 0, 1;\ \mu_2 = 0, 1;\ \ldots;\ \mu_N = 0, 1\,, \tag{1.3.9}$$

and $\sum_{i<j}^{(N)}$ denotes the sum over all possible pairs (i, j) chosen from the set $\{1, 2, \ldots, N\}$ with $i < j$. Furthermore, the wavenumber k_i and angular frequency ω_i of every soliton in an N-soliton solution is constrained only by the dispersion relation of the form

$$P(k_i, \omega_i) = 0\,. \tag{1.3.10}$$

It has been conjectured that Hirota's method is related to the integrability of a model. To understand this relationship, suppose a system can be written in Hirota bilinear form, with the one-soliton solution given by equation (1.3.5). Furthermore, suppose that for any positive integer N, the system admits an N-soliton solution of the form

$$\tau = 1 + \sum_{i=1}^{N} e^{\Gamma_i} + \text{ finite number of higher order terms.} \tag{1.3.11}$$

We then say that the system is Hirota integrable. It has been observed that if a set of equations is Hirota integrable, it also satisfies the more conventional definitions of integrability [17]. However, no proof of this conjecture has been found so far.

Furthermore, it is often claimed that the existence of the exact one-, two- and three-soliton Hirota solutions of a given model is a sufficient condition for the model to be Hirota integrable [17, e.g.]. On the other hand, nonintegrable PDEs that only possess one- and two-soliton Hirota solutions are said to be partial integrable models [16]. (Note that this does not necessarily mean that solutions describing three or more solitons do not exist for these models; it only shows that they cannot be obtained using the Hirota method.) The mRLW equation is an example of a partial integrable model, as we will discuss in more detail in subsection 1.3.3.

1.3.2 Hirota solutions of the KdV equation

In this subsection, we construct the well-known one-, two- and three-soliton Hirota solutions of the KdV equation [18, e.g.], with the aim to investigate the parity properties of these solutions in the next chapter.

We find that defining the τ-function as

$$u = \frac{12}{\alpha} \left(\ln \tau\right)_{xx} , \tag{1.3.12}$$

and substituting it into the KdV equation (see equation (1.1.3)), yields

$$\begin{aligned} 0 = {} & 2\tau_x^3 + 8\tau_{xxx}\tau_x^2 - \tau_x \left[6\tau_{xx}^2 + \tau \left(2\tau_{xt} + 3\tau_{xx} + 5\tau_{xxxx}\right)\right] \\ & + \tau_t \left(2\tau_x^2 - \tau\tau_{xx}\right) + \tau \left[2\tau_{xx}\tau_{xxx} + \tau \left(\tau_{xxt} + \tau_{xxx} + \tau_{xxxxx}\right)\right] . \end{aligned} \tag{1.3.13}$$

As described in the previous subsection, we make the following one-soliton ansatz

$$\tau = 1 + \eta e^{\Gamma_1} . \tag{1.3.14}$$

After making this ansatz, we find that the equation (1.3.13) is trivially satisfied for the lowest order in terms of η (i.e., η^0). Looking at the next order (i.e., η^1), the equation is non-trivially satisfied if k_i and ω_i, for $i = 1$, satisfy the following dispersion relation

$$\omega_i = k_i(1 + k_i^2) . \tag{1.3.15}$$

Imposing these constraints implies that all the higher order terms vanish trivially, showing that equation (1.3.14) leads to a family of exact one-soliton solutions.

As discussed in the previous subsection, we choose

$$\tau = 1 + \eta e^{\Gamma_1} + \eta e^{\Gamma_2} + \eta^2 A_{12} e^{\Gamma_1 + \Gamma_2} \tag{1.3.16}$$

to construct the two-soliton solution. Subsequently, we find that if we impose equation (1.3.15) on the frequencies of each soliton and define A_{ij}, for $i = 1$ and $j = 2$, in the following way

$$A_{ij} = \frac{(k_i - k_j)^2}{(k_i + k_j)^2} , \tag{1.3.17}$$

then the two-soliton τ-function solves the KdV equation exactly.

Loking at equation (1.3.8), the three-soliton ansatz takes the following form

$$\begin{aligned}\tau = 1 + \eta e^{\Gamma_1} + \eta e^{\Gamma_2} + \eta e^{\Gamma_3} + \eta^2 A_{12} e^{\Gamma_1+\Gamma_2} + \eta^2 A_{13} e^{\Gamma_1+\Gamma_3} + \eta^2 A_{23} e^{\Gamma_2+\Gamma_3} \\ + \eta^3 A_{12} A_{13} A_{23} e^{\Gamma_1+\Gamma_2+\Gamma_3}\,.\end{aligned} \tag{1.3.18}$$

Then we find again that by imposing equations (1.3.15) and (1.3.17), this τ-function solves the KdV equation analytically.

1.3.3 Hirota solutions of the perturbed KdV equation

In this subsection, we construct the known analytical soliton solutions of the RLW and mRLW equation, and we also construct a new family of one-soliton solutions that analytically solve equation (1.1.1) for any value of ε_2 and $\varepsilon = 1$.

To construct these solutions, we introduce the following Hirota τ-function

$$u = -\frac{8\beta}{\alpha}\left(\ln\tau\right)_{xt}\,, \tag{1.3.19}$$

where β is a real parameter that will have to be determined. Note that using equation (1.1.2), we can write

$$w = -\frac{8\beta}{\alpha}\left(\ln\tau\right)_{x} + g_1(x) \quad \text{and} \quad v = -\frac{8\beta}{\alpha}\left(\ln\tau\right)_{t} + g_2(t)\,, \tag{1.3.20}$$

where $g_1(x)$ and $g_2(t)$ are the 'constants' of integration with respect to t and x, respectively. Since $u \propto \left(\ln\tau\right)_{xt}$, the solution in terms of the u-field is not affected when we scale the τ-function as $\tau \to f_1 f_2 \tau$, for any function $f_1 = f_1(x)$ and $f_2 = f_2(t)$. Hence, we can ignore the integration 'constants' in equation (1.3.20). Armed with this observation, it will be convenient to introduce the field $q = q(x,t)$ that is proportional to the antiderivative of the u-field in the following way

$$u = -\frac{8}{\alpha} q_{xt}\,, \tag{1.3.21}$$

and so w and v can be written as

$$w = -\frac{8}{\alpha} q_x \quad \text{and} \quad v = -\frac{8}{\alpha} q_t\,. \tag{1.3.22}$$

Substituting the above expressions for u, w, and v into equation (1.1.1) yields a total x-derivative of the following equation

$$q_{tt} + q_{xt} - 4q_{xt}^2 - 2\varepsilon_2 q_{xx} q_{tt} + q_{xxxt} - \varepsilon_1 \left(q_{xxtt} + q_{xxxt}\right) = 0\,. \tag{1.3.23}$$

This implies that any solution of equation (1.3.23) also solves equation (1.1.1).

Now, using equation (1.3.21), we can rewrite equation (1.3.19) as

$$q = \beta \ln \tau\,. \tag{1.3.24}$$

Substituting this expression for q into equation (1.3.23) yields

$$\begin{aligned} 0 = & -\tau^2 \Big[2\beta\varepsilon_2 \tau_{tt}\tau_{xx} + (4\beta - 2\varepsilon_1)\tau_{xt}^2 + \tau_t \left(-2\varepsilon_1 \tau_{xxt} - (\varepsilon_1 - 1)\tau_{xxx} + \tau_x\right) \\ & -2\varepsilon_1 \tau_x \tau_{xtt} - \varepsilon_1 \tau_{tt}\tau_{xx} - 3(\varepsilon_1 - 1)\tau_{xt}\tau_{xx} - 3\varepsilon_1 \tau_x \tau_{xxt} + \tau_t^2 + 3\tau_x \tau_{xxt}\Big] \\ & + 2\tau \Big[(\beta\varepsilon_2 - \varepsilon_1)\tau_{xx}\tau_t^2 + (\beta\varepsilon_2 - \varepsilon_1)\tau_{tt}\tau_x^2 \\ & + \tau_x \tau_t \left(4(\beta - \varepsilon_1)\tau_{xt} - 3(\varepsilon_1 - 1)\tau_{xx}\right) - 3(\varepsilon_1 - 1)\tau_x^2 \tau_{xt}\Big] \\ & - 2\tau_t \tau_x^2 \left[(\beta(\varepsilon_2 + 2) - 3\varepsilon_1)\tau_t - 3(\varepsilon_1 - 1)\tau_x\right] \\ & + \tau^3 \left(-\varepsilon_1 \tau_{xxtt} - \varepsilon_1 \tau_{xxxt} + \tau_{tt} + \tau_{xt} + \tau_{xxxt}\right)\,. \end{aligned} \tag{1.3.25}$$

Then, following the approach discussed in subsection 1.3.1, we choose the following one-soliton ansatz

$$\tau = 1 + \eta e^{\Gamma_1}\,, \tag{1.3.26}$$

and we find that the equation (1.3.25) at the first order of η is satisfied if k_i and ω_i, for $i = 1$, are constrained by

$$\omega_i = \frac{k_i + (1 - \varepsilon_1)k_i^3}{1 - \varepsilon_1 k_i^2}\,. \tag{1.3.27}$$

For the order corresponding to η^2, it is satisfied if k_i, for $i = 1$, satisfies

$$\frac{2k_i^4 \left[(\varepsilon_1 - 1)\, k_i^2 - 1\right] \left[\beta\left(\varepsilon_2 + 2\right)\left(\left(\varepsilon_1 - 1\right) k_i^2 - 1\right) + 3\right]}{\left(\varepsilon_1 k_i^2 - 1\right)^2} = 0\,. \tag{1.3.28}$$

Since we only want k_1 and ω_1 to be constrained by the dispersion relation (see

subsection 1.3.1), we make the following choice to satisfy the above equation

$$\varepsilon_1 = 1 \quad \text{and} \quad \beta = \frac{3}{2+\varepsilon_2}\,. \tag{1.3.29}$$

Imposing these constraints implies that all the higher order terms vanish trivially, showing that equation (1.3.26) leads to a family of exact solutions. That is, the following expression

$$q = \frac{3}{2+\varepsilon_2} \ln\left(1 + e^{\Gamma_1}\right) \tag{1.3.30}$$

solves equation (1.1.1) exactly, provided that $\varepsilon_1 = 1$ and that the following dispersion relation is satisfied

$$\omega_i = \frac{k_i}{1-k_i^2}\,. \tag{1.3.31}$$

Setting $\alpha = 8$ for definiteness, the family of analytical one-soliton solutions can then be written as

$$u = \frac{3k_1\omega_1}{4(2+\varepsilon_2)\cosh^2(\Gamma_1/2)}\,. \tag{1.3.32}$$

Note that this class of solutions solves both the RLW equation (i.e., $\varepsilon_1 = 1$ and $\varepsilon_2 = 0$) and the mRLW equation (i.e., $\varepsilon_1 = \varepsilon_2 = 1$) as special cases.

It follows from equations (1.3.31) and (1.3.32) that the amplitude, A, is given by

$$A = \frac{3k_1\omega_1}{4(2+\varepsilon_2)} = \frac{3k_1^2}{4(2+\varepsilon_2)(1-k_1^2)}\,, \tag{1.3.33}$$

and the phase velocity is

$$v_p = \frac{\omega_1}{k_1} = \frac{1}{1-k_1^2}\,. \tag{1.3.34}$$

For definiteness, we will always impose that $0 < k_1 < 1$, unless stated otherwise, and so we see that the soliton always has a positive amplitude and velocity.

For the two-soliton solutions, we use the ansatz

$$\tau = 1 + \eta e^{\Gamma_1} + \eta e^{\Gamma_2} + \eta^2 A_{12} e^{\Gamma_1+\Gamma_2}\,. \tag{1.3.35}$$

Following a similar procedure, we now find that

$$\beta = \varepsilon_1 = \varepsilon_2 = 1\,, \tag{1.3.36}$$

with the dispersion relation expressed by equation (1.3.31) and

$$A_{ij} = -\frac{(\omega_i - \omega_j)^2(k_i - k_j)^2 + (\omega_i - \omega_j)(k_i - k_j) - (\omega_i - \omega_j)^2}{(\omega_i + \omega_j)^2(k_i + k_j)^2 + (\omega_i + \omega_j)(k_i + k_j) - (\omega_i + \omega_j)^2}\,. \tag{1.3.37}$$

It then follows from equations (1.3.24) and (1.3.35) that

$$q = \ln\left(1 + e^{\Gamma_1} + e^{\Gamma_2} + A_{12}e^{\Gamma_1+\Gamma_2}\right) \tag{1.3.38}$$

exactly solves equation (1.1.1), provided that equations (1.3.31), (1.3.36) and (1.3.37) are satisfied. Note that equation (1.3.36) implies that equation (1.1.1) reduces to equation (1.1.9). In other words, equation (1.3.38) is an analytical solution of the mRLW equation.

Let us add that one can approximate the values of the conserved charges Q_1 and $Q_2^{\varepsilon_2}$ for the analytical one- and two-soliton solutions (see equations (1.3.30) and (1.3.38)) as

$$Q_1 = [-q_t]_{x=-\infty}^{\infty} \approx \frac{3}{2+\varepsilon_2}\sum_{i=1}^{N}\omega_i\,, \quad N = 1, 2\,, \tag{1.3.39}$$

and

$$Q_2^{\varepsilon_2} = [-q_x]_{x=-\infty}^{\infty} \approx -\frac{3}{2+\varepsilon_2}\sum_{i=1}^{N}k_i\,, \quad N = 1, 2\,. \tag{1.3.40}$$

In chapter 4 we will check if these relations also hold for numerical simulations of equation (1.1.1).

Finally, we have also the checked three- and four-soliton ansatzes in a similar way. We found that the expansions do not truncate. In other words, the three- and four-soliton ansatzes do not generate analytical solutions of the perturbed KdV equation.

Note that since the mRLW equation does not admit three-soliton Hirota solutions but it does admit one- and two-soliton Hirota solutions, the mRLW equation is a partial integrable model. Furthermore, as mentioned in section 1.2, when two integrable solitons scatter, the only result of their interaction is the phase shift they experience. It turns out that the two mRLW solitons expressed by equation (1.3.38) also experience a phase shift when they scatter. To determine the analytical expression of this

shift, let us introduce two new variables

$$y = x - \frac{\omega_1}{k_1}t \quad \text{and} \quad z = x - \frac{\omega_2}{k_2}t\,. \tag{1.3.41}$$

Let us first substitute y into Γ_1 and Γ_2, that is,

$$\Gamma_1 = k_1 y + \delta_1 \quad \text{and} \quad \Gamma_2 = k_2 y + \left(\frac{k_2\omega_1 - k_1\omega_2}{k_1}\right) t + \delta_2\,. \tag{1.3.42}$$

For definiteness, we let $k_1 > k_2$, and so

$$k_2\omega_1 - k_1\omega_2 > 0\,. \tag{1.3.43}$$

Therefore, as $t \to \infty$, q described by equation (1.3.38) can now be approximated as follows

$$\begin{aligned}\lim_{t\to\infty} q(y,t) &= \Gamma_2 + \ln\left(e^{-\Gamma_2} + e^{\Gamma_1-\Gamma_2} + 1 + A_{12}e^{\Gamma_1}\right)\\ &\approx \Gamma_2 + \ln\left(1 + A_{12}e^{\Gamma_1}\right)\,,\end{aligned} \tag{1.3.44}$$

and so

$$\lim_{t\to\infty} u(y,t) \approx \frac{k_1\omega_1 e^{\Gamma_1+\ln A_{12}}}{\left(1+e^{\Gamma_1+\ln A_{12}}\right)^2}\,. \tag{1.3.45}$$

Furthermore, it is easy to see that

$$\lim_{t\to-\infty} q(y,t) \approx \ln\left(1 + e^{\Gamma_1}\right)\,, \tag{1.3.46}$$

and so

$$\lim_{t\to-\infty} u(y,t) \approx \frac{k_1\omega_1 e^{\Gamma_1}}{\left(1+e^{\Gamma_1}\right)^2}\,. \tag{1.3.47}$$

Repeating the same procedure with the variable z yields

$$\lim_{t\to\infty} u(z,t) \approx \frac{k_2\omega_2 e^{\Gamma_2}}{\left(1+e^{\Gamma_2}\right)^2} \tag{1.3.48}$$

and

$$\lim_{t\to-\infty} u(z,t) \approx \frac{k_2\omega_2 e^{\Gamma_2+\ln A_{12}}}{\left(1+e^{\Gamma_2+\ln A_{12}}\right)^2}\,. \tag{1.3.49}$$

Thus, the solitary wave corresponding to Γ_1 is phase-shifted forward by $\ln A_{12}$ after the collision, while the wave corresponding to Γ_2 is phase-shifted in the opposite direction by $\ln A_{12}$.

1.4 Quasi-integrability

Integrable models are quite rare, and often only approximately describe physical systems. To find more reliable models of certain nonlinear physical phenomena, one needs to introduce extra terms to the set of integrable PDEs. This often spoils the integrability of such a model. However, if the perturbing terms are small, the model may give rise to dissipative solitons, i.e., soliton-like structures that scatter rather stable, but nonelastically, with other soliton- and radiation-like structures [26, and references therein]. In this case, the models are often described as 'nearly integrable'.

These observations have lead to various attempts to define the concept of quasi-integrability [11, 12, e.g.]. To introduce this concept, consider a nearly integrable PDE in $(1+1)$ dimensions that admits soliton-like solutions, $u = u(x,t)$, and assume that $u \to 0$ sufficiently fast as $x \to \pm\infty$. Furthermore, suppose that the underlying integrable model, i.e., the model without the perturbation terms, can be represented by a zero curvature equation which leads to infinitely many conserved charges $Q^{(n)}$. However, in the presence of the perturbing terms, the curvature does not vanish which leads to the so-called anomalous curvature equation. As a result, the infinite charges $Q^{(n)}$ are not truly conserved. Instead, suppose that the infinite $Q^{(n)}$'s in the perturbed theory, for multi-soliton solutions, satisfy the following two equations

$$\frac{dQ^{(n)}}{dt} = \alpha^{(n)} \tag{1.4.1}$$

and

$$\lim_{t\to-\infty} Q^{(n)} = \lim_{t\to\infty} Q^{(n)}\,, \tag{1.4.2}$$

where the so-called anomalies $\alpha^{(n)}$ are dependent on the solution u and its derivatives. Note that the anomalies vanish for the integrable model and so the $Q^{(n)}$'s in this case are truly conserved charges. However, in the perturbing case, i.e., when the anomalies do not vanish, it follows from these equations that the charges are only conserved asymptotically. It is then said that the charges are quasi-conserved, and the corresponding solution is said to be quasi-integrable.

For all the models that have been studied in the context of quasi-integrability, each anomaly is of the following form

$$\alpha^{(n)} = \int_{-\infty}^{\infty} \mathrm{d}x \, \beta^{(n)} \,, \tag{1.4.3}$$

where $\beta^{(n)}$ is some function dependent on u and its derivatives. Thus, it follows from equations (1.4.1) and (1.4.2) that

$$\int_{-\infty}^{\infty} \mathrm{d}t \, \alpha^{(n)} = \int_{-\infty}^{\infty} \mathrm{d}t \int_{-\infty}^{\infty} \mathrm{d}x \, \beta^{(n)} = 0 \,. \tag{1.4.4}$$

This shows that the property of quasi-integrability can potentially be explained by parity arguments. Namely, if the $\beta^{(n)}$'s are odd functions with respect to space-time inversion, then equation (1.4.4) is automatically satisfied and, as a result, equation (1.4.2) will also be satisfied. Since all the $\beta^{(n)}$'s are dependent on the solution u and its derivatives, attempts have been made to relate quasi-integrability to the parity properties of multi-soliton solutions [13, e.g.].

Quasi-integrability is a new concept in nonlinear mathematical physics that is still being developed, and its underlying structures are not well understood thus far. To further investigate the concepts discussed in this section, we will devote chapters 2 and 6 to study the analytical and numerical quasi-integrability properties of the perturbed KdV equation.

Chapter 2

Quasi-integrability

In this chapter, we analytically investigate the quasi-integrability properties of the perturbed KdV equation. To be specific, since equation (1.1.1) can be seen as a perturbation of the integrable KdV equation, we use the KdV Lax potential A_x (see equation (1.2.7)) to construct an infinite amount of potentially quasi-conserved charges. For the analytical mRLW two-soliton solutions, we prove that these charges are truly quasi-conserved. Furthermore, in the last two sections of this chapter, we investigate the quasi-integrability properties of a solution that can be expressed as an expansion around an exact KdV solution with special parity properties.

2.1 The graded $\mathfrak{sl}(2)$ Lie algebra

In order to construct the potentially conserved charges, we first introduce the $\mathfrak{sl}(2)$ algebra. Namely, we will work with the following basis

$$T_3 = \frac{1}{2}\sigma_3 \quad \text{and} \quad T_\pm = \frac{1}{2}(\sigma_1 \pm i\sigma_2)\,, \tag{2.1.1}$$

where σ_1, σ_2 and σ_3 denote the Pauli matrices. This basis satisfies the following commutation relations

$$[T_3, T_\pm] = \pm T_\pm \quad \text{and} \quad [T_+, T_-] = 2T_3\,. \tag{2.1.2}$$

Next, let us introduce a graded basis, depending on a spectral parameter λ, in the following way

$$b_{2m+1} = \lambda^m \left(T_+ + \lambda T_-\right) , \quad F_{2m+1} = \lambda^m \left(T_+ - \lambda T_-\right) \quad \text{and} \quad F_{2m} = 2\lambda^m T_3 , \tag{2.1.3}$$

where $m \in \mathbb{Z}$. Their commutation relations take the following form

$$[b_{2m+1}, b_{2n+1}] = 0 , \tag{2.1.4}$$

$$[F_{2m+1}, F_{2n+1}] = 0 , \tag{2.1.5}$$

$$[F_{2m}, F_{2n}] = 0 , \tag{2.1.6}$$

$$[b_{2m+1}, F_{2n+1}] = -2F_{2(m+n+1)} , \tag{2.1.7}$$

$$[b_{2m+1}, F_{2n}] = -2F_{2(m+n)+1} , \tag{2.1.8}$$

$$[F_{2m+1}, F_{2n}] = -2b_{2(m+n)+1} . \tag{2.1.9}$$

Furthermore, we introduce the grading operator

$$\mathrm{d} = T_3 + 2\lambda \frac{d}{d\lambda} , \tag{2.1.10}$$

which satisfies the following commutation relations

$$[\mathrm{d}, b_{2m+1}] = (2m+1) b_{2m+1} \quad \text{and} \quad [\mathrm{d}, F_m] = m F_m . \tag{2.1.11}$$

2.2 The anomalous curvature equation

In order to construct the anomalous curvature equation, we introduce the Lax potentials, A_x and A_t, as follows

$$A_x = -\left[b_1 - \frac{\alpha}{12} u \left(b_{-1} - F_{-1}\right)\right] \tag{2.2.1}$$

and

$$A_t = -\left[-4b_3 - b_1 + \frac{\alpha}{6} u_x F_0 - \frac{\alpha}{3} u F_1 + \frac{G}{2}\left(b_{-1} - F_{-1}\right)\right] , \tag{2.2.2}$$

where G is defined as

$$G = \frac{\alpha^2}{18}u^2 + \frac{\alpha^2}{24}\varepsilon_2 w_x v_t - \frac{\alpha}{6}\varepsilon_1 u_{xt} + \frac{\alpha}{6}(1-\varepsilon_1)\,u_{xx} + \frac{\alpha}{6}u\,. \tag{2.2.3}$$

If we now define the function X as

$$X = \frac{\alpha}{6}\left[\frac{\alpha}{4}\varepsilon_2 w_x v_t - \varepsilon_1\left(u_{xt} + u_{xx}\right)\right], \tag{2.2.4}$$

and Y as

$$Y = u_t + u_x + \left[\frac{\alpha}{2}u^2 + \varepsilon_2\frac{\alpha}{4}w_x v_t + u_{xx} - \varepsilon_1\left(u_{xt} + u_{xx}\right)\right]_x, \tag{2.2.5}$$

then the curvature, $\mathcal{F}_{tx}$, can be written as

$$\mathcal{F}_{tx} = \partial_t A_x - \partial_x A_t + [A_t, A_x] = -XF_0 + \frac{\alpha}{12}Y\left(b_{-1} - F_{-1}\right). \tag{2.2.6}$$

Assuming that the u-field solves the perturbed KdV equations such that $Y = 0$, then X can be considered to be the anomaly of the zero curvature equation, and equation (2.2.6) is therefore called the anomalous curvature equation. Note that the anomaly X vanishes for the case of the KdV equation (i.e., $\varepsilon_1 = \varepsilon_2 = 0$) and note that the Lax potential A_x is of the same form as the potential A_x given in equation (1.2.7). This implies that for $\varepsilon_1 = \varepsilon_2 = 0$, the charges generated by A_x correspond to the well-known infinite amount of conserved charges related to the KdV equation, as we will show in the following subsection.

2.2.1 Quasi-conserved charges

To construct the potentially quasi-conserved charges of the curvature $\mathcal{F}_{tx}$, we use the same methods discussed in [12, e.g.]. We first gauge transform A_x and A_t in the following way

$$a_x = gA_x g^{-1} - (\partial_x g)\,g^{-1}, \tag{2.2.7}$$

$$a_t = gA_t g^{-1} - (\partial_t g)\,g^{-1}, \tag{2.2.8}$$

where $g \in \mathrm{SL}(2)$ is defined as

$$g = \exp\left(\sum_{n=1}^{\infty} \zeta_n F_{-n}\right) . \tag{2.2.9}$$

By Taylor expanding, we find that a_x can be expressed as

$$\begin{aligned} a_x = A_x &+ \left[\sum_{n=1}^{\infty} \zeta_n F_{-n}, A_x\right] + \frac{1}{2!}\left[\sum_{n=1}^{\infty} \zeta_n F_{-n}, \left[\sum_{m=1}^{\infty} \zeta_m F_{-m}, A_x\right]\right] \\ &- \sum_{m=1}^{\infty} (\partial_x \zeta_m) F_{-m} - \frac{1}{2!}\left[\sum_{n=1}^{\infty} \zeta_n F_{-n}, \sum_{m=1}^{\infty} (\partial_x \zeta_m) F_{-m}\right] \\ &- \frac{1}{3!}\left[\sum_{k=1}^{\infty} \zeta_k F_{-k}, \left[\sum_{n=1}^{\infty} \zeta_n F_{-n}, \sum_{m=1}^{\infty} (\partial_x \zeta_m) F_{-m}\right]\right] + \cdots . \end{aligned} \tag{2.2.10}$$

Using equation (2.2.1), and the algebra expressed by equations (2.1.4) to (2.1.9), we can write a_x as

$$\begin{aligned} a_x = & -b_1 \\ & - 2\zeta_1 F_0 \\ & - 2\zeta_2 F_{-1} + \frac{\alpha u}{12}(b_{-1} - F_{-1}) + 2\zeta_1^2 b_{-1} - (\partial_x \zeta_1) F_{-1} \\ & - 2\zeta_3 F_{-2} + \frac{\alpha u}{6}\zeta_1 F_{-2} - (\partial_x \zeta_2) F_{-2} \\ & - \cdots , \end{aligned} \tag{2.2.11}$$

where, for clarity, we have collected all the terms of the same grade on separate lines.

Next, for equation (2.2.11), we recursively choose the parameters ζ_{n+1} to kill the components in the F_{-n} direction. For example, the first few terms are chosen as

$$\zeta_1 = 0 , \tag{2.2.12}$$

$$\zeta_2 = -\frac{\alpha u}{24} - \frac{1}{2}(\partial_x \zeta_1) = -\frac{\alpha u}{24} , \tag{2.2.13}$$

$$\zeta_3 = \frac{\alpha u}{12}\zeta_1 - \frac{1}{2}(\partial_x \zeta_2) = \frac{\alpha}{48} u_x . \tag{2.2.14}$$

Having chosen the parameters ζ_{n+1} this way, we can now write a_x as

$$a_x = -b_1 + \sum_{n=0}^{\infty} a_x^{(-2n-1)} b_{-2n-1} , \tag{2.2.15}$$

where, for example, the first few values of $a_x^{(-2n-1)}$ are defined by

$$a_x^{(-1)} = \frac{\alpha u}{2^2 3}\,, \tag{2.2.16}$$

$$a_x^{(-3)} = \frac{\alpha^2 u^2}{2^5 3^2}\,, \tag{2.2.17}$$

$$a_x^{(-5)} = \frac{\alpha^3 u^3}{2^7 3^3} + \frac{\alpha^2 u u_{xx}}{2^7 3^2}\,, \tag{2.2.18}$$

$$a_x^{(-7)} = \frac{5\alpha^4 u^4}{2^{11} 3^4} + \frac{\alpha^3 u^2 u_{xx}}{2^7 3^3} + \frac{\alpha^3 u u_x^2 + \alpha^2 u u_{xxxx}}{2^9 3^2}\,. \tag{2.2.19}$$

The gauge-transformed curvature f_{tx} (under the gauge transformation expressed by equations (2.2.7) and (2.2.8), where g is defined by equations (2.2.9) with the parameters ζ_n chosen in the way described above) takes the form

$$f_{tx} = \partial_t a_x - \partial_x a_t + [a_t, a_x] = g\mathcal{F}_{tx}g^{-1} = -XgF_0g^{-1}\,, \tag{2.2.20}$$

where we have imposed the equations of motion such that $Y = 0$. After Taylor expanding and using the commutation relations, we find that we can express a_t in general as

$$a_t = 4b_3 + b_1 + \sum_{n=0}^{\infty} a_t^{(-2n-1)} b_{-2n-1} + \sum_{n=-2}^{\infty} c_t^{(-n)} F_{-n}\,, \tag{2.2.21}$$

and the gauge-transformed curvature takes the general form

$$f_{tx} = -X\left(\sum_{n=0}^{\infty} \gamma^{(-2n-1)} b_{-2n-1} + \sum_{n=0}^{\infty} \epsilon^{(-n)} F_{-n}\right)\,, \tag{2.2.22}$$

where the first non-trivial $\gamma^{(-2n-1)}$'s are defined as

$$\gamma^{(-1)} = 0\,, \tag{2.2.23}$$

$$\gamma^{(-3)} = -\partial_x\left[\frac{\alpha}{2^3 3} u\right]\,, \tag{2.2.24}$$

$$\gamma^{(-5)} = -\partial_x\left[\frac{\alpha^2}{2^6 3} u^2 + \frac{\alpha}{2^5 3} u_{xx}\right]\,, \tag{2.2.25}$$

$$\gamma^{(-7)} = -\partial_x\left[\frac{5\alpha^3}{2^8 3^3} u^3 + \frac{5\alpha^2}{2^8 3^2} u_x^2 + \frac{5\alpha^2}{2^7 3^2} u_{xx} + \frac{\alpha}{2^7 3} u_{xxxx}\right]\,. \tag{2.2.26}$$

Note that the commutator $[a_x, a_t]$ in equation (2.2.20) will not produce any terms in the direction of the b_{-2n-1} basis vectors. Thus, if we now only write down the terms of the gauge-transformed curvature in the direction of the b_{-2n-1} matrices,

then we get the following relation

$$-X\gamma^{(-2n-1)} = \partial_t a_x^{(-2n-1)} - \partial_x a_t^{(-2n-1)}\,, \quad \forall n \in \mathbb{Z}_0^+\,. \tag{2.2.27}$$

Integrating this equation with respect to x over the entire domain yields

$$\frac{dQ^{(-2n-1)}}{dt} = a_t^{(-2n-1)}\Big|_{x=-\infty}^{\infty} + \alpha^{(-2n-1)}\,, \tag{2.2.28}$$

where $Q^{(-2n-1)}$ is defined as

$$Q^{(-2n-1)} = \int_{-\infty}^{\infty} \mathrm{d}x\, a_x^{(-2n-1)} \tag{2.2.29}$$

and $\alpha^{(-2n-1)}$ is defined as

$$\alpha^{(-2n-1)} = -\int_{-\infty}^{\infty} \mathrm{d}x\, X\gamma^{(-2n-1)}\,. \tag{2.2.30}$$

Since all the group parameters ζ_n are dependent on u and its derivatives, and $u \to 0$ when $x \to \pm\infty$, we find that $g \to \mathbb{1}$ as $x \to \pm\infty$. This implies that

$$\lim_{x\to\pm\infty} a_t = \lim_{x\to\pm\infty} A_t\,, \tag{2.2.31}$$

and so it follows from equation (2.2.2) that

$$a_t^{(-2n-1)}\Big|_{x=-\infty}^{\infty} = 0\,. \tag{2.2.32}$$

Hence, equation (2.2.28) becomes

$$\frac{dQ^{(-2n-1)}}{dt} = \alpha^{(-2n-1)}\,, \tag{2.2.33}$$

and so the $Q^{(-2n-1)}$'s are potentially quasi-conserved. Note that, as we mentioned at the beginning of section 2.2, the quantities $Q^{(-2n-1)}$ have the same expression as the well-known conserved charges of the KdV equation. In other words, the $Q^{(-2n-1)}$'s are truly conserved when u solves the KdV equation.

Furthermore, note that it follows from equations (2.2.16) and (2.2.23) that

$$Q^{(-1)} = \frac{\alpha}{12}\int_{-\infty}^{\infty} \mathrm{d}x\, u \quad \text{and} \quad \frac{dQ^{(-1)}}{dt} = 0\,, \tag{2.2.34}$$

which implies that $Q^{(-1)}$ is a conserved quantity for any value of ε_1 and ε_2, as we discussed in section 1.1. On the other hand, the charges $Q^{(-2n-1)}$ for $n > 0$ are not exactly conserved. In the next two sections, we prove that the charges are in fact quasi-conserved for the exact mRLW two-soliton solutions. Furthermore, our numerical results strongly indicate that the charges are also quasi-conserved for the two- and three-soliton solutions governed by the RLW equation and the mRLW equation; this is discussed in more detail in chapter 6.

2.3 The parity argument

In this section, we discuss two different parity symmetries to analyse the quasi-conservation properties of the charges that were introduced in the previous section.

2.3.1 The parity argument for travelling wave solutions

Let us first consider the family of travelling wave solutions $u = u(x - \frac{\omega}{k}t + \delta)$ that solves equation (1.1.1). To this end, we define the shifted space coordinate, $\bar{x}$, as follows

$$\bar{x} = x - \frac{\omega}{k}t + \delta\,. \tag{2.3.1}$$

Next, let us introduce the space parity operator

$$\mathcal{P}_{\bar{x}} : \bar{x} \mapsto -\bar{x}\,, \tag{2.3.2}$$

and assume that u is an even function, that is,

$$\mathcal{P}_{\bar{x}}\, u = u\,. \tag{2.3.3}$$

It follows from equation (1.1.2) that

$$w = \int \mathrm{d}t\, u = -\frac{k}{\omega}\int \mathrm{d}\bar{x}\, u \tag{2.3.4}$$

and

$$v = \int \mathrm{d}x\, u = \int \mathrm{d}\bar{x}\, u\,. \tag{2.3.5}$$

Since w and v are antiderivatives of the even function u, we can always choose the 'constants' of integration (without affecting the u-field) such that w and v are odd functions, that is,

$$\mathcal{P}_{\bar{x}}\, w = -w \quad \text{and} \quad \mathcal{P}_{\bar{x}}\, v = -v\,. \tag{2.3.6}$$

As a result, w_x and v_t are even under the parity transformation

$$\mathcal{P}_{\bar{x}}\, w_x = w_x \quad \text{and} \quad \mathcal{P}_{\bar{x}}\, v_t = v_t\,. \tag{2.3.7}$$

Furthermore, it is easy to see that u_{xt} and u_{xx} are also even under parity

$$\mathcal{P}_{\bar{x}}\, u_{xt} = u_{xt} \quad \text{and} \quad \mathcal{P}_{\bar{x}}\, u_{xx} = u_{xx}\,. \tag{2.3.8}$$

Combining the above ingredients, we see that the anomaly X is also even under parity

$$\mathcal{P}_{\bar{x}}\, X = X\,. \tag{2.3.9}$$

Furthermore, the pattern of the $\gamma^{(-2n-1)}$'s, where the first few are given in equations (2.2.23) to (2.2.26), shows that they are always odd

$$\mathcal{P}_{\bar{x}}\, \gamma^{(-2n-1)} = -\gamma^{(-2n-1)}\,, \quad \forall n \in \mathbb{Z}_0^+\,. \tag{2.3.10}$$

Therefore, we conclude that the $X\gamma^{(-2n-1)}$ are also odd functions and, as a result, the $\alpha^{(-2n-1)}$'s vanish, that is,

$$\alpha^{(-2n-1)} = -\int_{-\infty}^{\infty} \mathrm{d}\bar{x}\, X\gamma^{(-2n-1)} = 0\,. \tag{2.3.11}$$

It follows from equation (2.2.33) that the charges expressed by equation (2.2.29) are independent of time (i.e., they are truly conserved). Since the one-soliton solutions constructed in subsection 1.3.3 are special cases of travelling wave solutions, their corresponding charges are therefore also truly conserved.

2.3.2 The parity argument for multi-soliton solutions

In this subsection, we consider the more general class of solutions $u = u(x,t)$ that solves equation (1.1.1). We first define the new coordinates, $\tilde{x}$ and $\tilde{t}$, relative to some point (x_Δ, t_Δ), as follows

$$\tilde{x} = x - x_\Delta \quad \text{and} \quad \tilde{t} = t - t_\Delta \,, \tag{2.3.12}$$

and we define the space-time parity operator as

$$\mathcal{P} : (\tilde{x}, \tilde{t}) \mapsto (-\tilde{x}, -\tilde{t}) \,. \tag{2.3.13}$$

We will again assume that the solution is an even function under this transformation, that is,

$$\mathcal{P}\, u = u \,. \tag{2.3.14}$$

Similarly as in the previous subsection, we find that w and v are odd functions

$$\mathcal{P}\, w = -w \quad \text{and} \quad \mathcal{P}\, v = -v \,. \tag{2.3.15}$$

It follows that G and X are even (see equations (2.2.3) and (2.2.4)), and Y is odd (see equation (2.2.5)), that is,

$$\mathcal{P}\, G = G \,, \quad \mathcal{P}\, X = X \quad \text{and} \quad \mathcal{P}\, Y = -Y \,. \tag{2.3.16}$$

Next, let $\sigma : \mathfrak{sl}(2) \to \mathfrak{sl}(2)$ denote the following automorphism

$$\begin{aligned} \sigma(T) &= e^{i\pi\,\mathrm{d}} T e^{-i\pi\,\mathrm{d}} \\ &= T + i\pi[\mathrm{d}, T] + \frac{(i\pi)^2}{2}[\mathrm{d}, [\mathrm{d}, T]] + \frac{(i\pi)^3}{3!}[\mathrm{d}, [\mathrm{d}, [\mathrm{d}, T]]] + \cdots \,, \end{aligned} \tag{2.3.17}$$

where d is the grading operator defined in section 2.1. Using the commutation relations described by equation (2.1.11), this leads to the expression

$$\sigma(b_{2n+1}) = e^{i\pi(2n+1)} b_{2n+1} = -b_{2n+1} \,, \tag{2.3.18}$$

and similarly

$$\sigma(F_{2n+1}) = -F_{2n+1} \quad \text{and} \quad \sigma(F_{2n}) = F_{2n} \,. \tag{2.3.19}$$

Combing these ingredients, let Ω denote the space-time parity transformation applied to the aforementioned automorphism, that is,

$$\Omega = \mathcal{P}\,\sigma\,. \tag{2.3.20}$$

It follows from equation (2.2.6), with $Y = 0$, that

$$\Omega(\mathcal{F}_{tx}) = \mathcal{F}_{tx}\,. \tag{2.3.21}$$

Furthermore, suppose that we have chosen the ζ_n is in the way described in subsection 2.2.1 such that the first few terms are given by equations (2.2.12) to (2.2.14). Then it follows from the pattern of ζ_n that

$$\Omega(\zeta_n F_{-n}) = (-1)^n\,\mathcal{P}\,\zeta_n F_{-n} = \zeta_n F_{-n}\,, \tag{2.3.22}$$

and so

$$\Omega(g) = g \quad \text{and} \quad \Omega(g^{-1}) = g^{-1}\,, \tag{2.3.23}$$

where g is the group element defined by equation (2.2.9). Thus, it follows from equation (2.2.20) that

$$\Omega(f_{tx}) = \Omega(g\mathcal{F}_{tx}g^{-1}) = \Omega(g)\Omega(\mathcal{F}_{tx})\Omega(g^{-1}) = g\mathcal{F}_{tx}g^{-1} = f_{tx}\,. \tag{2.3.24}$$

Let us now focus on the first term on the right-hand side of equation (2.2.22). In particular, it follows from equation (2.3.24) that the following expression must be satisfied

$$\Omega(X\gamma^{(-2n-1)}b_{-2n-1}) \stackrel{!}{=} X\gamma^{(-2n-1)}b_{-2n-1}\,, \quad \forall n \in \mathbb{Z}_0^+\,. \tag{2.3.25}$$

It then follows from the results expressed by equations (2.3.16) and (2.3.18) that

$$\mathcal{P}\,\gamma^{(-2n-1)} = -\gamma^{(-2n-1)}\,, \tag{2.3.26}$$

and so we can conclude that

$$\mathcal{P}\,X\gamma^{(-2n-1)} = -X\gamma^{(-2n-1)} \implies \int_{-\tilde{t}}^{\tilde{t}} \mathrm{d}t \int_{-\tilde{x}}^{\tilde{x}} \mathrm{d}x\, X\gamma^{(-2n-1)} = 0\,. \tag{2.3.27}$$

It follows from equations (2.2.30) and (2.2.33) that

$$Q^{(-2n-1)}(\tilde{t}) - Q^{(-2n-1)}(-\tilde{t}) = \int_{-\tilde{t}}^{\tilde{t}} \mathrm{d}t\, \alpha^{(-2n-1)} = 0\,, \tag{2.3.28}$$

$$\implies Q^{(-2n-1)}(\tilde{t}) = Q^{(-2n-1)}(-\tilde{t})\,. \tag{2.3.29}$$

Thus, we see that these quantities satisfy equation (1.4.2) when $\tilde{t} \to \infty$, and so are, by definition, quasi-conserved. To sum up, we have shown that any solution of equation (1.1.1) that satisfies equation (2.3.14) is a quasi-integrable solution.

2.4 Parity of the exact two-soliton mRLW solutions

In this section, we show that the exact two-soliton mRLW solutions satisfy equation (2.3.14) and, thus, its charges $Q^{(-2n-1)}$ are quasi-conserved. To this end, we introduce two new variables, z_+ and z_-, in the following way

$$z_+ = \frac{1}{2}(\Gamma_1 + \Gamma_2 + \ln A_{12}) \quad \text{and} \quad z_- = \frac{1}{2}(\Gamma_1 - \Gamma_2)\,. \tag{2.4.1}$$

Then the two-soliton τ-function described by equation (1.3.35)) can be expressed as

$$\begin{aligned} \tau &= 1 + e^{z_+ + z_- - \frac{1}{2}\ln A_{12}} + e^{z_+ - z_- - \frac{1}{2}\ln A_{12}} + e^{2z_+} \\ &= 2e^{z_+}\left(\cosh z_+ + A_{12}^{-1/2}\cosh z_-\right)\,. \end{aligned} \tag{2.4.2}$$

Note that $A_{12} = 0$ if $k_1 = k_2$, and so the two-soliton solutions reduce to single-soliton travelling wave solutions. Thus, we will only consider $k_1 \neq k_2$ in the following discussion. In this case, z_+ and z_- are linearly independent and can be considered as independent space-time variables. In fact, by defining

$$k_\pm = \frac{1}{2}(k_1 \pm k_2)\,, \quad \omega_\pm = \frac{1}{2}(\omega_1 \pm \omega_2) \quad \text{and} \quad \delta_\pm = \frac{1}{2}(\delta_1 \pm \delta_2)\,, \tag{2.4.3}$$

we can express z_+ and z_- in terms of x and t as

$$\begin{pmatrix} z_+ \\ z_- \end{pmatrix} = \begin{pmatrix} k_+ & -\omega_+ \\ k_- & -\omega_- \end{pmatrix} \begin{pmatrix} x \\ t \end{pmatrix} + \begin{pmatrix} \delta_+ + \frac{1}{2}\ln A_{12} \\ \delta_- \end{pmatrix} . \tag{2.4.4}$$

Using the variables $\tilde{x}$ and $\tilde{t}$ (see equation (2.3.12)), we can rewrite this equation in the following way

$$\begin{pmatrix} \tilde{x} \\ \tilde{t} \end{pmatrix} = \begin{pmatrix} k_+ & -\omega_+ \\ k_- & -\omega_- \end{pmatrix}^{-1} \begin{pmatrix} z_+ \\ z_- \end{pmatrix} , \tag{2.4.5}$$

where x_Δ and t_Δ are defined as

$$x_\Delta = \frac{\omega_+\delta_- - \omega_-(\delta_+ + \frac{1}{2}\ln A_{12})}{k_+\omega_- - k_-\omega_+} \quad \text{and} \quad t_\Delta = \frac{k_+\delta_- - k_-(\delta_+ + \frac{1}{2}\ln A_{12})}{k_+\omega_- - k_-\omega_+} . \tag{2.4.6}$$

Thus, we see that $\mathcal{P}$ described by equation (2.3.13) also acts as a symmetry operator on (z_+, z_-), that is,

$$\mathcal{P} : (z_+, z_-) \mapsto (-z_+, -z_-) . \tag{2.4.7}$$

Since $\partial_x z_\pm = k_\pm$ and $\partial_t z_\pm = -\omega_\pm$, it follows from equations (1.3.21), (1.3.24) and (2.4.2) that

$$\begin{aligned} u = {} & \frac{8\left[(k_+\omega_+ + k_-\omega_-)\cosh z_+ \cosh z_- - (k_+\omega_- + k_-\omega_+)\sinh z_+ \sinh z_-\right]}{\alpha A_{12}^{1/2}\left(\cosh z_+ + A_{12}^{-1/2}\cosh z_-\right)^2} \\ & + \frac{8\left(k_+\omega_+ + A_{12}^{-1}k_-\omega_-\right)}{\alpha\left(\cosh z_+ + A_{12}^{-1/2}\cosh z_-\right)^2} , \end{aligned} \tag{2.4.8}$$

and so we see that u obeys equation (2.3.14). Due to the result discussed in the previous section, we can conclude that the charges defined by equation (2.2.29) corresponding to the mRLW two-soliton solution (i.e., $\varepsilon_1 = \varepsilon_2 = 1$) are quasi-conserved.

Note that the coordinates given in equation (2.4.6) describe the point in space-time around which the u-field is symmetric under $\mathcal{P}$. Therefore, we expect that these coordinates represent the point in space-time that the solitons pass through each other. This is illustrated in figure 2.1, which shows an analytical two-soliton solution expressed by equation (1.3.38); the point where the dotted and the dashed

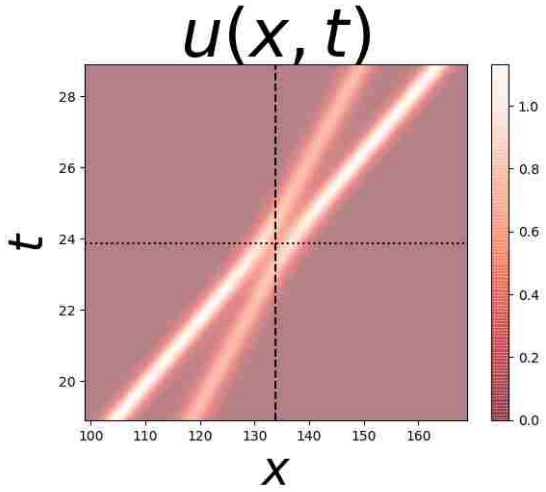

Figure 2.1: The two-soliton mRLW u-field in the (x, t) plane. The dotted curve shows the line $t = t_\Delta$ and the dashed curve shows the line $x = x_\Delta$, defined by the expressions in equation (2.4.6). In other words, the point where the two lines cross each other is the point of symmetry under the space-time parity operator $\mathcal{P}$.

curve cross each other is the point (x_Δ, t_Δ).

2.5 Parity of the exact KdV solutions

In this section, we discuss the parity properties of the one-, two- and three-soliton solutions of the KdV equation (see subsection 1.3.2). The results will be important for the next section where we investigate the quasi-integrability properties of perturbed KdV solutions around some exact KdV solution that is even under $\mathcal{P}$.

From equation (1.3.14) it is easy to see that the one-soliton solution is invariant under $\mathcal{P}_{\bar{x}}$. Let us therefore focus on the two-soliton solutions expressed by equation (1.3.16). To analyse its parity properties, we express the τ-function in terms of the variables z_+ and z_- expressed by equation (2.4.1), that is,

$$\tau = 2e^{z_+} \left(\cosh z_+ + A_{12}^{-1/2} \cosh z_- \right) . \tag{2.5.1}$$

It follows from equation (1.3.12) that the corresponding u-field takes the form

$$\begin{aligned} u = & \frac{12\left[A_{12}^{1/2}(k_-^2+k_+^2)\cosh z_- \cosh z_+ + k_-^2\cosh^2 z_-\right]}{\alpha\left(A_{12}^{1/2}\cosh z_+ + \cosh z_-\right)^2} \\ & + \frac{12\left[k_+^2 A_{12}\cosh^2 z_+ - \left(k_-\sinh z_- + k_+ A_{12}^{1/2}\sinh z_+\right)^2\right]}{\alpha\left(A_{12}^{1/2}\cosh z_+ + \cosh z_-\right)^2}\,, \end{aligned} \tag{2.5.2}$$

where $k_\pm$ are defined by equation (2.4.3). Thus, it follows from equation (2.4.7) that the two-soliton solutions are even under $\mathcal{P}$.

To investigate the parity properties of the three-soliton solutions, we introduce the following variables

$$z_-^{(1)} = \frac{1}{2}(-\Gamma_1+\Gamma_2+\Gamma_3+\ln A_{23})\,, \tag{2.5.3}$$

$$z_-^{(2)} = \frac{1}{2}(\Gamma_1-\Gamma_2+\Gamma_3+\ln A_{13})\,, \tag{2.5.4}$$

$$z_-^{(3)} = \frac{1}{2}(\Gamma_1+\Gamma_2-\Gamma_3+\ln A_{12})\,, \tag{2.5.5}$$

$$z_+^{(1)} = z_-^{(1)}+z_-^{(2)}+z_-^{(3)} = \frac{1}{2}(\Gamma_1+\Gamma_2+\Gamma_3+\ln A_{12}+\ln A_{13}+\ln A_{23})\,. \tag{2.5.6}$$

Furthermore, it will be useful to define

$$k^{(1)} = -k_- + \frac{1}{2}k_3\,, \quad \omega^{(1)} = -\omega_- + \frac{1}{2}\omega_3\,, \quad \Delta^{(1)} = -\delta_- + \frac{1}{2}(\delta_3+\ln A_{23})\,, \tag{2.5.7}$$

$$k^{(2)} = k_- + \frac{1}{2}k_3\,, \quad \omega^{(2)} = \omega_- + \frac{1}{2}\omega_3\,, \quad \Delta^{(2)} = \delta_- + \frac{1}{2}(\delta_3+\ln A_{13})\,, \tag{2.5.8}$$

$$k^{(3)} = k_+ - \frac{1}{2}k_3\,, \quad \omega^{(3)} = \omega_+ - \frac{1}{2}\omega_3\,, \quad \Delta^{(3)} = \delta_+ + \frac{1}{2}(-\delta_3+\ln A_{12})\,, \tag{2.5.9}$$

so that we can write

$$z_-^{(i)} = k^{(i)}x - \omega^{(i)}t + \Delta^{(i)}\,. \tag{2.5.10}$$

Then we can express equation (1.3.18) as

$$\tau = 2e^{z_+^{(1)}}F\,, \tag{2.5.11}$$

where the function F is defined as

$$\begin{aligned} F = & \cosh z_+^{(1)} + A_{12}^{-1/2}A_{13}^{-1/2}\cosh z_-^{(1)} + A_{12}^{-1/2}A_{23}^{-1/2}\cosh z_-^{(2)} \\ & + A_{13}^{-1/2}A_{23}^{-1/2}\cosh z_-^{(3)}\,. \end{aligned} \tag{2.5.12}$$

Using equation (1.3.12), we can write the τ-function corresponding to the three-soliton solutions as

$$u = \frac{12}{\alpha}\left(\frac{FF_{xx} - (F_x)^2}{F^2}\right), \tag{2.5.13}$$

with

$$\begin{aligned} F_x = &\left(k^{(1)} + k^{(2)} + k^{(3)}\right)\sinh z_+^{(1)} + k^{(1)}A_{12}^{-1/2}A_{13}^{-1/2}\sinh z_-^{(1)} \\ &+ k^{(2)}A_{12}^{-1/2}A_{23}^{-1/2}\sinh z_-^{(2)} + k^{(3)}A_{13}^{-1/2}A_{23}^{-1/2}\sinh z_-^{(3)} \end{aligned} \tag{2.5.14}$$

and

$$\begin{aligned} F_{xx} = &\left(k^{(1)} + k^{(2)} + k^{(3)}\right)^2\cosh z_+^{(1)} + \left(k^{(1)}\right)^2 A_{12}^{-1/2}A_{13}^{-1/2}\cosh z_-^{(1)} \\ &+ \left(k^{(2)}\right)^2 A_{12}^{-1/2}A_{23}^{-1/2}\cosh z_-^{(2)} + \left(k^{(3)}\right)^2 A_{13}^{-1/2}A_{23}^{-1/2}\cosh z_-^{(3)}. \end{aligned} \tag{2.5.15}$$

Now, we want the space-time symmetry operator $\mathcal{P}$ (see equation (2.3.13)) to change the sign of $(z_+^{(1)}, z_+^{(2)}, z_+^{(3)})$. These three variables describes three straight lines in the (x,t) plane, and so the point of symmetry is at the point where the three lines cross each other. Combining these ingredients, we see that we need to choose the given point (x_Δ, t_Δ) in such a way that the point of symmetry is at the origin of the coordinate system described by $(z_+^{(1)}, z_+^{(2)}, z_+^{(3)})$. To this end, we express equation (2.5.10) as the following matrix equation

$$\begin{pmatrix} k^{(1)} & -\omega^{(1)} & \Delta^{(1)} \\ k^{(2)} & -\omega^{(2)} & \Delta^{(2)} \\ k^{(3)} & -\omega^{(3)} & \Delta^{(3)} \end{pmatrix}\begin{pmatrix} x_\Delta \\ t_\Delta \\ 1 \end{pmatrix} = \begin{pmatrix} 0 \\ 0 \\ 0 \end{pmatrix}. \tag{2.5.16}$$

Since this is a system of homogeneous linear equations, it is non-trivially satisfied if the determinant of the square matrix vanishes, that is,

$$\begin{aligned} 0 = &\left(\Delta^{(1)} + \Delta^{(2)}\right)\left(k_1^3k_2 - k_1k_2^3\right) + \left(\Delta^{(1)} + \Delta^{(3)}\right)\left(k_3^3k_1 - k_3k_1^3\right) \\ &+ \left(\Delta^{(2)} + \Delta^{(3)}\right)\left(k_2^3k_3 - k_2k_3^3\right). \end{aligned} \tag{2.5.17}$$

If $k_i = k_j$ for $i \neq j$, then the three-soliton solutions reduce to two-soliton solutions. In other words, we demand that $k_1 \neq k_2 \neq k_3$. Therefore, to satisfy equation (2.5.17),

we impose that

$$\Delta^{(1)} = \Delta^{(2)} = \Delta^{(3)} = 0\,. \tag{2.5.18}$$

This condition can be rewritten as the following matrix equation

$$\begin{pmatrix} 1 & -1 & -1 \\ -1 & 1 & -1 \\ -1 & -1 & 1 \end{pmatrix} \begin{pmatrix} \delta_1 \\ \delta_2 \\ \delta_3 \end{pmatrix} = \begin{pmatrix} \ln A_{23} \\ \ln A_{13} \\ \ln A_{12} \end{pmatrix}\,. \tag{2.5.19}$$

We solve this equation by imposing the following condition on the phase constants

$$\delta_i = -\frac{1}{2}\ln\left(A_{ij}A_{ik}\right)\,. \tag{2.5.20}$$

As a result, equation (2.5.10) reduces to

$$z_-^{(i)} = k^{(i)}x - \omega^{(i)}t\,. \tag{2.5.21}$$

We now easily see that the space-time operator $\mathcal{P}$ acts as follows on the new coordinates

$$\mathcal{P} : (z_-^{(1)}, z_-^{(2)}, z_-^{(3)}) \mapsto (-z_-^{(1)}, -z_-^{(2)}, -z_-^{(3)}) \implies \mathcal{P} : z_+^{(1)} \mapsto -z_+^{(1)}\,, \tag{2.5.22}$$

where the space-time point of symmetry is at $x_\Delta = t_\Delta = 0$, that is,

$$\mathcal{P} : (x,t) \mapsto (-x,-t)\,. \tag{2.5.23}$$

Looking at equation (2.5.13) and the expressions for F, F_x and F_{xx}, we see that the three-soliton solutions are even under this operator, provided the three solitons collide at the same point in space-time.

2.6 Parity of the perturbed KdV solutions

In this section, we consider an expansion of u, which is assumed to solve the perturbed KdV equation, around an exact solution of the KdV equation. We then assume that the exact KdV solution is even under the space-time parity operator, and argue that under this assumption the perturbed system seems to favour even solutions to a

certain extent.

To simplify the expansion, we express the perturbation parameters ε_1 and ε_2 as follows

$$\varepsilon_1 = \varepsilon \sin\xi \quad \text{and} \quad \varepsilon_2 = \varepsilon \cos\xi \,, \tag{2.6.1}$$

and so equation (1.1.1) can be written as

$$u_t + u_x + \left[\frac{\alpha}{2}u^2 + u_{xx} + \varepsilon\left(\frac{\alpha}{4}w_x v_t \cos\xi - (u_{xt} + u_{xx})\sin\xi\right)\right]_x = 0\,. \tag{2.6.2}$$

We expand the solution as

$$u = \sum_{n=0}^{\infty} \varepsilon^n u^{(n)} = u^{(0)} + \varepsilon u^{(1)} + \varepsilon^2 u^{(2)} + \cdots \,, \tag{2.6.3}$$

which implies that

$$w = \int \mathrm{d}t\, u = \sum_{n=0}^{\infty} \varepsilon^n \int \mathrm{d}t\, u^{(n)} \equiv \sum_{n=0}^{\infty} \varepsilon^n w^{(n)} \tag{2.6.4}$$

and

$$v = \int \mathrm{d}x\, u = \sum_{n=0}^{\infty} \varepsilon^n \int \mathrm{d}x\, u^{(n)} \equiv \sum_{n=0}^{\infty} \varepsilon^n v^{(n)}\,. \tag{2.6.5}$$

Collecting the terms at order ε^0 gives

$$u_t^{(0)} + u_x^{(0)} + \left[\frac{\alpha}{2}\left(u^{(0)}\right)^2 + u_{xx}^{(0)}\right]_x = 0\,, \tag{2.6.6}$$

and so we see that $u^{(0)}$ solves the KdV equation, as desired.

Collecting terms at the next order, we find that

$$u_t^{(1)} + u_x^{(1)} + \left[\alpha u^{(0)}u^{(1)} + u_{xx}^{(1)} + \frac{\alpha}{4}w_x^{(0)}v_t^{(0)}\cos\xi - \left(u_{xt}^{(0)} + u_{xx}^{(0)}\right)\sin\xi\right]_x = 0\,. \tag{2.6.7}$$

Next, we decompose u, w and v into its even and odd parts in the following way

$$u^{(i,\pm)} = \frac{1}{2}(1 \pm \mathcal{P})u^{(i)}\,, \quad w^{(i,\pm)} = \frac{1}{2}(1 \pm \mathcal{P})w^{(i)} \quad \text{and} \quad v^{(i,\pm)} = \frac{1}{2}(1 \pm \mathcal{P})v^{(i)}\,, \tag{2.6.8}$$

where $\mathcal{P}$ is defined by equation (2.3.13). Using this notation, we can write the even

part of equation (2.6.7) as

$$\begin{aligned} 0 = {} & \partial_t u^{(1,-)} + \partial_x u^{(1,-)} + \Big[\alpha \left(u^{(0,+)} u^{(1,-)} + u^{(0,-)} u^{(1,+)}\right) + \partial_x^2 u^{(1,-)} \\ & + \frac{\alpha}{4}\left(\partial_x w^{(0,+)} \partial_t v^{(0,-)} + \partial_x w^{(0,-)} \partial_t v^{(0,+)}\right) \cos\xi \\ & - \left(\partial_x \partial_t u^{(0,-)} + \partial_x^2 u^{(0,-)}\right) \sin\xi \Big]_x \,, \end{aligned} \tag{2.6.9}$$

and the odd part as

$$\begin{aligned} 0 = {} & \partial_t u^{(1,+)} + \partial_x u^{(1,+)} + \Big[\alpha \left(u^{(0,+)} u^{(1,+)} + u^{(0,-)} u^{(1,-)}\right) + \partial_x^2 u^{(1,+)} \\ & + \frac{\alpha}{4}\left(\partial_x w^{(0,+)} \partial_t v^{(0,+)} + \partial_x w^{(0,-)} \partial_t v^{(0,-)}\right) \cos\xi \\ & - \left(\partial_x \partial_t u^{(0,+)} + \partial_x^2 u^{(0,+)}\right) \sin\xi \Big]_x \,. \end{aligned} \tag{2.6.10}$$

Let us now suppose that the exact solution of the KdV equation, $u^{(0)}$, is even under space-time parity operator, that is,

$$\mathcal{P}\, u^{(0)} = u^{(0)} \implies \mathcal{P}\, w^{(0)} = -w^{(0)} \quad \text{and} \quad \mathcal{P}\, v^{(0)} = -v^{(0)} \,, \tag{2.6.11}$$

and so

$$u^{(0,-)} = 0 \quad \text{and} \quad w^{(0,+)} = v^{(0,+)} = 0 \,. \tag{2.6.12}$$

Subsequently, equation (2.6.9) reduces to

$$\partial_t u^{(1,-)} + \partial_x u^{(1,-)} + \left[\alpha u^{(0,+)} u^{(1,-)} + \partial_x^2 u^{(1,-)}\right]_x = 0 \,, \tag{2.6.13}$$

and equation (2.6.10) becomes

$$\begin{aligned} & \partial_t u^{(1,+)} + \partial_x u^{(1,+)} + \left[\alpha u^{(0,+)} u^{(1,+)} + \partial_x^2 u^{(1,+)}\right]_x = \\ & \quad - \left[\frac{\alpha}{4} \partial_x w^{(0,-)} \partial_t v^{(0,-)} \cos\xi - \left(\partial_x \partial_t u^{(0,+)} + \partial_x^2 u^{(0,+)}\right) \sin\xi\right]_x \,. \end{aligned} \tag{2.6.14}$$

This shows that $u^{(1,-)}$ satisfies a homogeneous equation and $u^{(1,+)}$ an inhomogeneous equation. Now, suppose that $u^{(1)}$ is an even function, that is,

$$u^{(1,-)} = 0 \implies w^{(1,+)} = v^{(1,+)} = 0 \,, \tag{2.6.15}$$

then equation (2.6.13) is trivially satisfied. Next, assuming that equations (2.6.12) and (2.6.15) are satisfied, we can repeat the same steps to determine that the even

part of the terms corresponding to ε^2 are given by

$$\partial_t u^{(2,-)} + \partial_x u^{(2,-)} + \left[\alpha u^{(0,+)} u^{(2,-)} + \partial_x^2 u^{(2,-)}\right]_x = 0\,, \tag{2.6.16}$$

and the odd part is given by

$$\begin{aligned}\partial_t u^{(2,+)} + \partial_x u^{(2,+)} + \left[\alpha u^{(0,+)} u^{(2,+)} + \partial_x^2 u^{(2,+)}\right]_x = \\ - \Big[\frac{\alpha}{2}\left(u^{(1,+)}\right)^2 + \frac{\alpha}{4}\left(\partial_x w^{(0,-)}\partial_t v^{(1,-)} + \partial_x w^{(1,-)}\partial_t v^{(0,-)}\right)\cos\xi \\ - \left(\partial_x\partial_t u^{(1,+)} + \partial_x^2 u^{(1,+)}\right)\sin\xi\Big]_x\,.\end{aligned} \tag{2.6.17}$$

This shows that, again, $u^{(2,-)}$ satisfies a homogeneous equation and $u^{(2,+)}$ satisfies an inhomogeneous equation. Just as for $u^{(1)}$, if $u^{(2)}$ is an even function, that is

$$u^{(2,-)} = 0 \implies w^{(2,+)} = v^{(2,+)} = 0\,. \tag{2.6.18}$$

then equation (2.6.16) is trivially satisfied. Continuing in the same way, it appears that $u^{(i,-)}$ satisfies a homogeneous equation for all i, and $u^{(i,+)}$ satisfies an inhomogeneous equation for all i. From this, if u is even under $\mathcal{P}$, then all the homogeneous equations would be trivially satisfied, which would also imply that the solution is quasi-integrable (see subsection 2.3.2). Of course, this analysis does not exclude the possibility of solutions that are a combination of even and odd functions, however u cannot be purely an odd function. In that sense, it appears that the perturbed model favours even solutions, which would imply that it is quasi-integrable.

To numerically test this result, we must ensure that u is an even function during the entire simulation. This means that solving this problem is more complex than just choosing initial conditions that are even, because we have no guarantee that the numerical solution remains even during the simulation. Unfortunately, we have not found a way to solve this problem.

Chapter 3

Finite difference methods

In the first section of this chapter, we describe the general LU decomposition method to solve tri-diagonal matrix equations. This algorithm will be used in the finite difference schemes discussed in the following two sections, where we develop two algorithms to approximate equation (1.3.23). Due to the presence of various mixed partial derivatives, these schemes will be a combination of implicit and explicit finite difference methods. A similar problem was encountered by J. C. Eilbeck and G. R. McGuire when they numerically investigated the RLW equation [7]. We follow their ideas, and modify them appropriately to solve equation (1.3.23). In addition, to test the stability properties of these schemes, we compute the numerical time evolution of various exact solutions constructed in subsection 1.3.3 and compare them with their analytical values.

3.1 LU decomposition

For the algorithms we construct in the next two sections, we will have to solve a system of linear equations of the form

$$AB = C\,, \tag{3.1.1}$$

where A is an $n \times n$ tridiagonal matrix, and B and C are column vectors. Note that A and C are known matrices, and we want to solve the equation for B. We will

use the LU decomposition method to solve this problem, which we briefly discuss in this section (see, for instance, the book by G. Schay for more information [25]). To this end, we decompose a general tridiagonal matrix A into an lower and upper triangular matrix as follows

$$A = LU\,. \tag{3.1.2}$$

More specifically, let us write the general $n \times n$ tridiagonal matrix A as

$$A = \begin{pmatrix} b_1 & c_1 & 0 & 0 & \cdots & \\ a_2 & b_2 & c_2 & 0 & & \\ 0 & a_3 & b_3 & c_3 & & \\ \vdots & & \ddots & \ddots & \ddots & \\ & & & a_{n-1} & b_{n-1} & c_{n-1} \\ & & & 0 & a_n & b_n \end{pmatrix}, \tag{3.1.3}$$

and let us write L and U as

$$L = \begin{pmatrix} 1 & 0 & 0 & 0 & \cdots & \\ l_2 & 1 & 0 & 0 & & \\ 0 & l_3 & 1 & 0 & & \\ \vdots & & \ddots & \ddots & \ddots & \\ & & & l_{n-1} & 1 & 0 \\ & & & 0 & l_n & 1 \end{pmatrix} \tag{3.1.4}$$

and

$$U = \begin{pmatrix} d_1 & c_1 & 0 & 0 & \cdots & \\ 0 & d_2 & c_2 & 0 & & \\ 0 & 0 & d_3 & c_3 & & \\ \vdots & & \ddots & \ddots & \ddots & \\ & & & 0 & d_{n-1} & c_{n-1} \\ & & & 0 & 0 & d_n \end{pmatrix}. \tag{3.1.5}$$

Then L and U are determined by the following recursive equations

$$d_1 = b_1\,, \quad l_i = a_i/d_{i-1} \quad \text{and} \quad d_i = b_i - l_i c_{i-1}\,, \tag{3.1.6}$$

where $i = 2, 3, \ldots, n$.

Next, we substitute equation (3.1.2) into equation (3.1.1) to get

$$LUB = C \implies UB = L^{-1}C \equiv Z\,. \tag{3.1.7}$$

Thus, in order to determine matrix B, we see that we have to solve the following two equations

$$LZ = C \quad \text{and} \quad UB = Z\,. \tag{3.1.8}$$

Since L is a lower triangular matrix, the first equation can be solved for Z by using forward-substitution. Once we have found Z, we use back-substitution to solve the second equation for B, as required.

3.2 First-order scheme

In order to numerically solve the perturbed KdV equation, we first make the following substitution

$$p = q_t \tag{3.2.1}$$

such that the equation (1.3.23) can be rewritten as

$$p_t + p_x - 4p_x^2 - 2\varepsilon_2 q_{xx} p_t + (1 - \varepsilon_1)p_{xxx} - \varepsilon_1 p_{xxt} = 0\,. \tag{3.2.2}$$

Next, we discretise x and t in a finite set of points $x_0, x_1, \ldots, x_N$ and $t_0, t_1, \ldots, t_K$, with the grid spacing h and the time step τ. Furthermore, we let p_i^m and q_i^m denote the solutions p and q at the grid point $(ih, m\tau)$, where $i = 0, 1, \ldots, N$ and $m = 0, 1, \ldots, K$. Finally, let v_i^m denote any approximation to p_i^m and let w_i^m denote any approximation to q_i^m.

To construct a finite difference method that is first-order in time and second-order in space, we introduce the following finite difference operators

$$\delta_x^2\, v_i^m = (v_{i+1}^m - 2v_i^m + v_{i-1}^m)/h^2\,, \tag{3.2.3}$$

$$\mathrm{H}_x\, v_i^m = (v_{i+1}^m - v_{i-1}^m)/2h\,, \tag{3.2.4}$$

$$\Delta_t\, v_i^m = (v_i^{m+1} - v_i^m)/\tau\,, \tag{3.2.5}$$

and these operators act similarly on w_i^m. Now, using these operators on equation (3.2.2) in a straightforward manner gives the following finite difference equation

$$\begin{aligned} 0 = {} & \Delta_t\, v_i^m + \mathrm{H}_x\, v_i^m - 4\,(\mathrm{H}_x\, v_i^m)^2 - 2\varepsilon_2\,\delta_x^2\, w_i^m\,\Delta_t\, v_i^m + (1-\varepsilon_1)\,\delta_x^2\,\mathrm{H}_x\, v_i^m \\ & - \varepsilon_1\,\delta_x^2\,\Delta_t\, v_i^m\,, \end{aligned} \tag{3.2.6}$$

which can be rewritten as

$$\begin{aligned} & \frac{v_i^{m+1}}{\tau} - 2\varepsilon_2\frac{(w_{i+1}^m - 2w_i^m + w_{i-1}^m)v_i^{m+1}}{h^2\tau} - \varepsilon_1\frac{v_{i+1}^{m+1} - 2v_i^{m+1} + v_{i-1}^{m+1}}{h^2\tau} = \\ & \qquad \frac{v_i^m}{\tau} - \frac{v_{i+1}^m - v_{i-1}^m}{2h} + \frac{\left(v_{i+1}^m - v_{i-1}^m\right)^2}{h^2} - 2\varepsilon_2\frac{\left(w_{i+1}^m - 2w_i^m + w_{i-1}^m\right)v_i^m}{h^2\tau} \\ & \qquad - (1-\varepsilon_1)\,\frac{v_{i+2}^m - 2v_{i+1}^m + 2v_{i-1}^m - v_{i-2}^m}{2h^3} - \varepsilon_1\frac{v_{i+1}^m - 2v_i^m + v_{i-1}^m}{h^2\tau}\,, \end{aligned} \tag{3.2.7}$$

for any $i \in \{2, 3, \ldots, N-2\}$ and $m \in \{0, 1, \ldots, K-1\}$. Next we introduce the following $(N+1)\times(N+1)$ tridiagonal matrix

$$A = \begin{pmatrix} 1 & 0 & 0 & 0 & 0 & \cdots & & \\ 0 & 1 & 0 & 0 & 0 & \cdots & & \\ 0 & -h\varepsilon_1 & a_2 & -h\varepsilon_1 & 0 & \cdots & & \\ 0 & 0 & -h\varepsilon_1 & a_3 & -h\varepsilon_1 & & & \\ \vdots & \vdots & & \ddots & \ddots & \ddots & & \\ & & & & -h\varepsilon_1 & a_{N-2} & -h\varepsilon_1 & 0 \\ & & & & 0 & 0 & 1 & 0 \\ & & & & 0 & 0 & 0 & 1 \end{pmatrix}, \tag{3.2.8}$$

where a_i is defined as

$$a_i = h^3 - 2h\varepsilon_2\left(w_{i+1}^m - 2w_i^m + w_{i-1}^m\right) + 2h\varepsilon_1\,. \tag{3.2.9}$$

We introduce the following $N+1$ column vectors

$$B = \begin{pmatrix} v_0^{m+1} \\ v_1^{m+1} \\ v_2^{m+1} \\ \vdots \\ v_{N-1}^{m+1} \\ v_N^{m+1} \end{pmatrix} \quad \text{and} \quad C = \begin{pmatrix} c_0 \\ c_1 \\ c_2 \\ \vdots \\ c_{N-1} \\ c_N^m \end{pmatrix}, \tag{3.2.10}$$

where c_i, for $i = 2, 3, \ldots, N-2$, is defined as

$$\begin{aligned} c_i = h^3 v_i^m &- \frac{h^2\tau}{2}\left(v_{i+1}^m - v_{i-1}^m\right) + h\tau\left(v_{i+1}^m - v_{i-1}^m\right)^2 \\ &- 2h\varepsilon_2\left(w_{i+1}^m - 2w_i^m + w_{i-1}^m\right) v_i^m \\ &- \frac{\tau}{2}\left(1-\varepsilon_1\right)\left(v_{i+2}^m - 2v_{i+1}^m + 2v_{i-1}^m - v_{i-2}^m\right) \\ &- h\varepsilon_1\left(v_{i+1}^m - 2v_i^m + v_{i-1}^m\right), \end{aligned} \tag{3.2.11}$$

with the following boundary conditions

$$c_0{}^m = v_0^{m+1}, \quad c_1^m = v_1^{m+1}, \quad c_{N-1}^m = v_{N-1}^{m+1} \quad \text{and} \quad c_N^m = v_N^{m+1}. \tag{3.2.12}$$

By multiplying both sides of equation (3.2.7) with $h^3\tau$, we can rewrite it as the following matrix equation

$$AB = C, \tag{3.2.13}$$

for any $m \in \{0, 1, \ldots, K-1\}$.

Note that the matrix A and the column vector C contain all the approximations v and w at the time level m, whereas B contains all the approximations v at $m+1$. Thus, assuming that we know the values of v and w at the time level $m = 0$ for all i (i.e., the initial condtions), and we know the values of v at $m = 1$ to satisfy the boundary conditions (see equation (3.2.12)), then we can calculate all the other values of v at $m = 1$ by solving equation (3.2.13) for B. (We use the LU decomposition method, as discussed in the previous section, to determine B.) To obtain the values

of w at $m = 1$, we solve equation (3.2.1) as follows

$$v_i^m = \Delta_t \, w_i^m \implies w_i^{m+1} = \tau v_i^m + w_i^m \,, \tag{3.2.14}$$

for all $i \in \{0, 1, 2, 3, \ldots, N\}$.

We repeat this procedure for all time levels to determine the numerical time evolution of the given initial configurations. For the actual soliton field u, we choose $\alpha = 8$ such that equation (1.3.21) becomes

$$u = -q_{xt} = -p_x \,. \tag{3.2.15}$$

Thus, we approximate u by applying the finite difference operator H_x on $-p$ in a straightforward manner.

3.2.1 Stability properties

In this subsection, we test this scheme with $h = 0.1$ and $\tau = 0.001$. First, we run it with various exact one-soliton solutions as initial conditions (see equation (1.3.30)). The green curve in figure 3.1 shows the time evolution of such a simulation with $\varepsilon_2 = 1$. And, for comparison, the red curve shows the corresponding analytical values. Figure 3.1a shows the start of the simulation at $t = 0$, and since the initial conditions of the numerical simulation are the same as the analytical values, the two curves lie exactly on top of each other. Figures 3.1b and 3.1c show the numerical

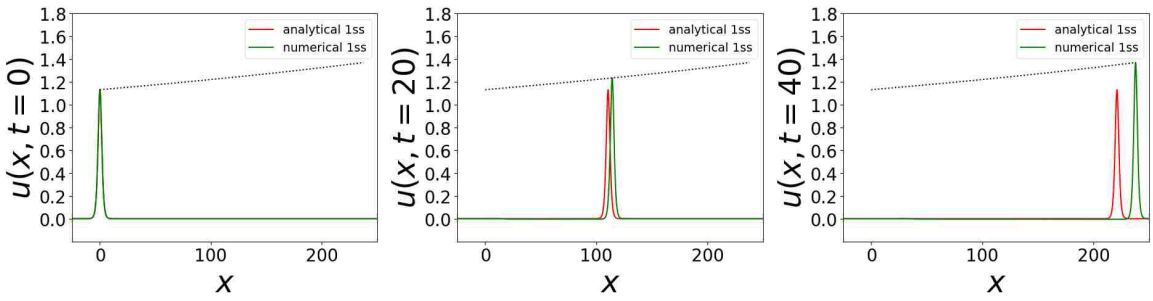

(a) $t = 0$ (b) $t = 20$ (c) $t = 40$

Figure 3.1: An analytical and numerical mRLW one-soliton solution $u(x, t)$ at different points in time. The dotted line shows the spatial trajectory of the numerical soliton's amplitude.

approximation at $t = 20$ and $t = 40$, respectively. We see that the amplitude of the numerical soliton increases over time. This is illustrated by the dotted curve in the figures, which shows how the amplitude of the numerical soliton changes as it propagates to the right.[1]

We have also tested this scheme with equation (1.3.38) as initial conditions. The results of such a simulation are presented in figure 3.2. The green curve represents the numerical solution, and the red curve shows the corresponding analytical values. Just as in the previous test, we see that the amplitudes of the numerical solitons are continuously increasing (except for when the solitons are interacting with each other), as shown by the dotted curves in figure 3.2. Note, however, that the amplitude corresponding to the larger soliton increases more rapidly than the amplitude of the

[1]We have obtained the amplitude of the numerical soliton at some fixed $t = t_i$ by finding the three highest points of the soliton, and assume they fit a polynomial of degree 2. Using the three highest points of the soliton, we then calculate the coefficients of the polynomial. Next, by taking the derivative of this polynomial and setting it equal to zero, we find the amplitude and its location at $t = t_i$. We repeat this procedure for all time levels to determine how the amplitude changes during the simulation.

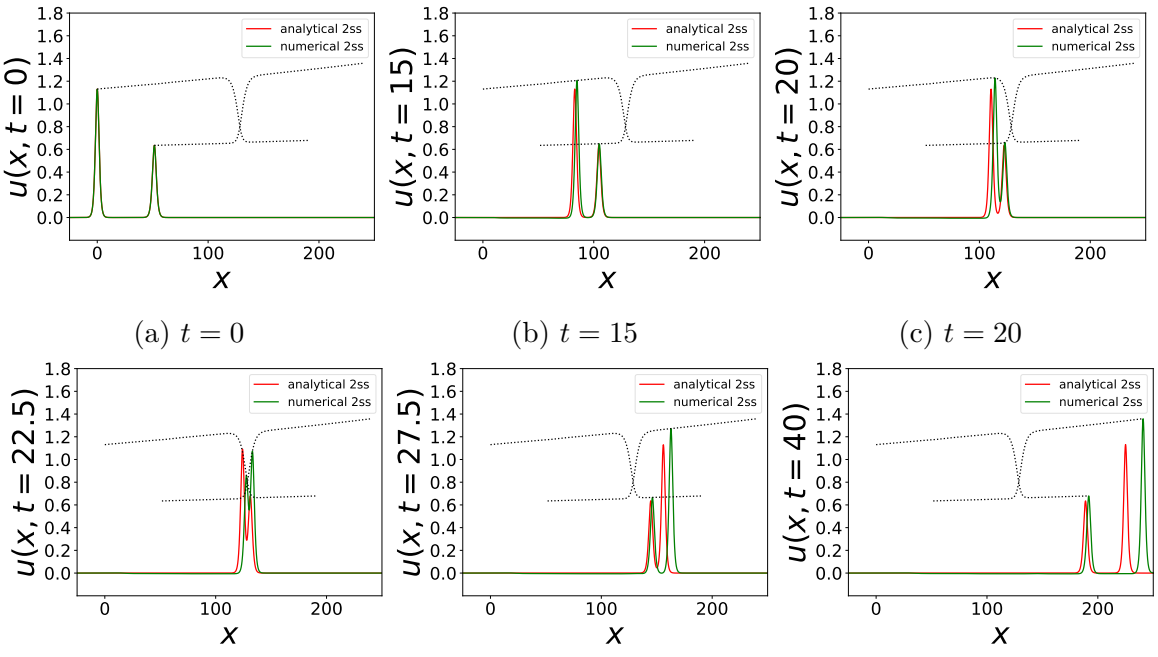

(a) $t = 0$ (b) $t = 15$ (c) $t = 20$

(d) $t = 22.5$ (e) $t = 27.5$ (f) $t = 40$

Figure 3.2: An analytical and numerical mRLW two-soliton solution $u(x, t)$ at different points in time. The dotted lines show the amplitudes' spatial trajectories of the two numerical solitons.

smaller soliton in the same amount of time. This is probably because the solution in the region of the smaller soliton changes less rapidly, and so the finite difference operators (see equations (3.2.3) to (3.2.5)) are better behaved in this region.

From the above two experiments it is clear the numerical solutions will eventually blow up if we run this simulation long enough, which indicates that this scheme is unstable for the chosen h and τ. We have also tried various other values of h and τ, and observed very similar behaviour in the sense that the amplitude of the numerical solitons increase as time progresses. We have also tested the one-soliton simulation with other values of ε_2, and we saw similar stability properties.

Finally, note that figures 3.1 and 3.2 show that the numerical solitons have moved further to the right than the corresponding analytical solutions in the same amount of time. Thus, we see that as the amplitude increases, the velocity of the soliton increases as well. This is consistent with equations (1.3.33) and (1.3.34).

3.3 Second-order scheme

The accuracy of the first-order scheme can be improved by using the central difference operator for time (instead of the forward difference operator used in the previous section), that is,

$$\mathrm{H}_t\, v_i{}^m = (v_i^{m+1} - v_i^{m-1})/2\tau\,. \tag{3.3.1}$$

We will now follow the same method as we did in the previous section. Thus, the finite difference equation now becomes

$$\begin{aligned} 0 = {} & \mathrm{H}_t\, v_i^m + \mathrm{H}_x\, v_i^m - 4\,(\mathrm{H}_x\, v_i^m)^2 - 2\varepsilon_2\,\delta_x^2\, w_i^m\, \mathrm{H}_t\, v_i^m + (1-\varepsilon_1)\,\delta_x^2\, \mathrm{H}_x\, v_i^m \\ & - \varepsilon_1\,\delta_x^2\, \mathrm{H}_t\, v_i^m\,. \end{aligned} \tag{3.3.2}$$

After making the substitutions, we find that this can be rewritten as

$$\begin{aligned}\frac{v_i^{m+1}}{2\tau} - \varepsilon_2\frac{(w_{i+1}^m - 2w_i^m + w_{i-1}^m)v_i^{m+1}}{h^2\tau} - \varepsilon_1\frac{v_{i+1}^{m+1} - 2v_i^{m+1} + v_{i-1}^{m+1}}{2h^2\tau} = \\ \frac{v_i^{m-1}}{2\tau} - \frac{v_{i+1}^m - v_{i-1}^m}{2h} + \frac{\left(v_{i+1}^m - v_{i-1}^m\right)^2}{h^2} - \varepsilon_2\frac{\left(w_{i+1}^m - 2w_i^m + w_{i-1}^m\right)v_i^{m-1}}{h^2\tau} \\ -(1-\varepsilon_1)\frac{v_{i+2}^m - 2v_{i+1}^m + 2v_{i-1}^m - v_{i-2}^m}{2h^3} - \varepsilon_1\frac{v_{i+1}^{m-1} - 2v_i^{m-1} + v_{i-1}^{m-1}}{2h^2\tau},\end{aligned} \tag{3.3.3}$$

for any $i \in \{2, 3, \ldots, N-2\}$ and $m \in \{1, 2, \ldots, K-1\}$. Now, we define the tridiagonal matrix A by

$$A = \begin{pmatrix} 1 & 0 & 0 & 0 & 0 & \cdots & & \\ 0 & 1 & 0 & 0 & 0 & \cdots & & \\ 0 & -\frac{h\varepsilon_1}{2} & a_2 & -\frac{h\varepsilon_1}{2} & 0 & \cdots & & \\ 0 & 0 & -\frac{h\varepsilon_1}{2} & a_3 & -\frac{h\varepsilon_1}{2} & & & \\ \vdots & \vdots & & \ddots & \ddots & \ddots & & \\ & & & & -\frac{h\varepsilon_1}{2} & a_{N-2} & -\frac{h\varepsilon_1}{2} & 0 \\ & & & & 0 & 0 & 1 & 0 \\ & & & & 0 & 0 & 0 & 1 \end{pmatrix}, \tag{3.3.4}$$

with a_i defined as

$$a_i = \frac{h^3}{2} - h\varepsilon_2\left(w_{i+1}^m - 2w_i^m + w_{i-1}^m\right) + h\varepsilon_1\,. \tag{3.3.5}$$

Just as we did in the previous section, we introduce the following $N+1$ column vectors

$$B = \begin{pmatrix} v_0^{m+1} \\ v_1^{m+1} \\ v_2^{m+1} \\ \vdots \\ v_{N-1}^{m+1} \\ v_N^{m+1} \end{pmatrix} \quad \text{and} \quad C = \begin{pmatrix} c_0 \\ c_1 \\ c_2 \\ \vdots \\ c_{N-1} \\ c_N^m \end{pmatrix}, \tag{3.3.6}$$

where c_i, for $i = 2, 3, \ldots, N-2$, is now defined as

$$\begin{aligned} c_i = \frac{h^3}{2} v_i^{m-1} &- \frac{h^2\tau}{2}\left(v_{i+1}^m - v_{i-1}^m\right) + h\tau\left(v_{i+1}^m - v_{i-1}^m\right)^2 \\ &- h\varepsilon_2\left(w_{i+1}^m - 2w_i^m + w_{i-1}^m\right) v_i^{m-1} \\ &- \frac{\tau}{2}(1-\varepsilon_1)\left(v_{i+2}^m - 2v_{i+1}^m + 2v_{i-1}^m - v_{i-2}^m\right) \\ &- \frac{h\varepsilon_1}{2}\left(v_{i+1}^{m-1} - 2v_i^{m-1} + v_{i-1}^{m-1}\right), \end{aligned} \tag{3.3.7}$$

and we have the same boundary conditions as in the previous section

$$c_0{}^m = v_0^{m+1}, \quad c_1^m = v_1^{m+1}, \quad c_{N-1}^m = v_{N-1}^{m+1} \quad \text{and} \quad c_N^m = v_N^{m+1}. \tag{3.3.8}$$

By multiplying both sides of equation (3.2.7) with $h^3\tau$, we can rewrite it as the matrix equation

$$AB = C, \tag{3.3.9}$$

for any $m \in \{1, 2, \ldots, K-1\}$.

Since we are using a central difference time operator, we need the initial conditions for w and v at the first two time levels (i.e., at $m = 0$ and $m = 1$). We can then, assuming we know the boundary conditions, determine v at $m = 2$ by solving equation (3.3.9) using the LU decomposition method. To solve equation (3.2.1), we again use the central difference time operator, that is,

$$v_i^m = \mathrm{H}_t\, w_i^m \implies w_i^{m+1} = 2\tau v_i^m + w_i^{m-1}, \tag{3.3.10}$$

for all $i \in \{0, 1, 2, 3, \ldots, N\}$. Thus, we can obtain w and v for each grid point by repeating this procedure for all time levels. Just as in the previous section, we choose $\alpha = 8$ to obtain the actual soliton field u (see equation (3.2.15)).

Finally, note that if we had substituted the finite difference operators directly into the perturbed KdV equation without first making the substitution expressed by equation (3.2.1), then the $4q_{xt}^2$ term would have yielded a term $(-w_{i+1}^{m+1} w_{i-1}^{m+1})/(2h^2\tau^2)$; and since this term contains two unknowns, (i.e., w_{i+1}^{m+1} and w_{i-1}^{m+1}), we would not have been able to solve for it. Moreover, for very similar reasons, we cannot use the well-known Crank-Nicolson method to numerically solve equation (1.3.23).

3.3.1 Stability properties

Just as in the previous section, we test this scheme by using the analytical Hirota solutions constructed in subsection 1.3.3 as initial conditions, with $h = 0.01$ and $\tau = 0.001$. First, we investigate the family of one-soliton solutions. The green curve in figure 3.3 represent such a one-soliton simulation with $\varepsilon_2 = 1$, and the red curve shows the corresponding analytical values. The simulation starts at $t = 0$ (see figure 3.3a), and since we use the analytical expression as initial conditions, the two curves lie exactly on top of each other. Figures 3.3b and 3.3b show the solutions at $t = 20$ and $t = 40$, and now we see that the amplitude of the numerical solution is stable. In fact, the numerical solution approximates the exact values so close that it is hard to distinguish between the green and the red curve. Therefore, we have added an inset in figure 3.3c to show the solitons at a smaller scale. We see that the shape and velocity of the numerical solutions approximates the analytical values indeed very closely. We have also performed this one-soliton test with other values of $\varepsilon_2 \neq 1$. These numerical solutions behaved in very similar way as for $\varepsilon_2 = 1$ in the sense that the numerical solutions are a very good approximation to the corresponding analytical values.

Furthermore, we have repeated this test with the class of mRLW two-soliton solutions (see equation (1.3.38)) as initial conditions. Figure 3.4 shows the time evolution of such a simulation. Just as for the one-soliton simulations, we see

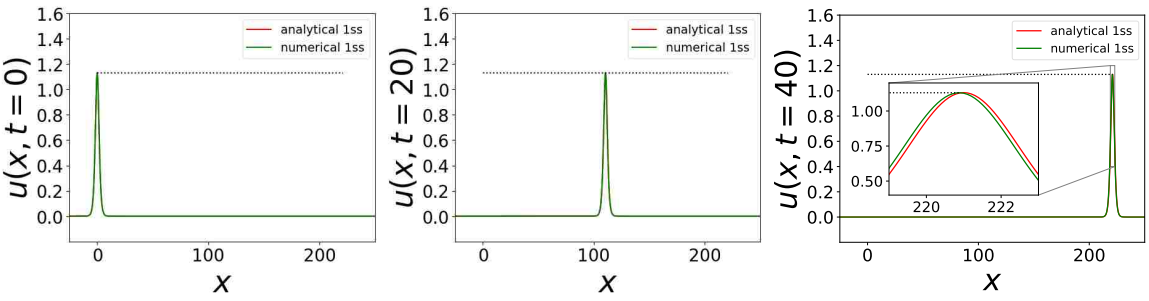

(a) $t = 0$ (b) $t = 20$ (c) $t = 40$

Figure 3.3: An analytical and numerical mRLW one-soliton solution $u(x, t)$ at different points in time. The dotted line shows the spatial trajectory of the numerical soliton's amplitude.

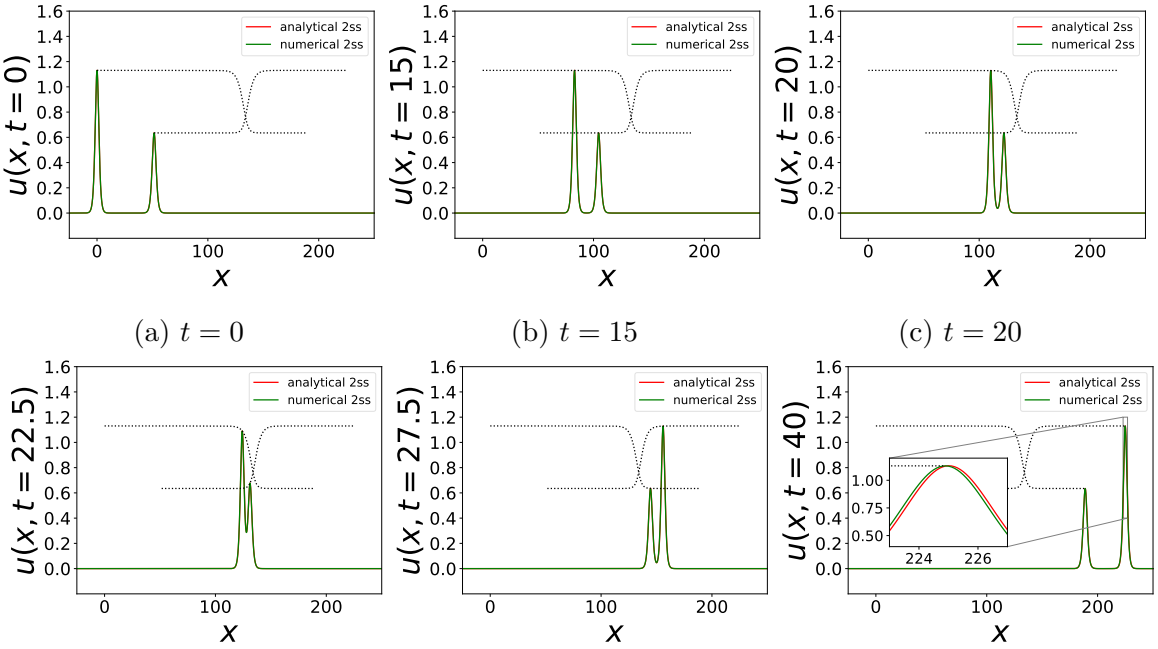

(a) $t = 0$ (b) $t = 15$ (c) $t = 20$

(d) $t = 22.5$ (e) $t = 27.5$ (f) $t = 40$

Figure 3.4: An analytical and numerical mRLW two-soliton solution $u(x, t)$ at different points in time. The dotted lines show the amplitudes' spatial trajectories of the two numerical solitons.

that the numerical solution stays very close to the exact values of equation (1.3.38). Figure 3.4f shows an inset of the region near the largest soliton at a much smaller scale. Similar to the one-soliton test, we see the soliton's shape and velocity are almost the same. Upon zooming in on the smallest soliton, we saw that the discrepancy between the analytical and numerical solutions was even smaller. This is probably because the finite difference operator behave slightly better in the region of the smaller soliton.

From these results, we conclude that this second-order finite difference scheme approximates equation (1.3.23) very well for $h = 0.1$ and $\tau = 0.001$. We have also tried other values of h and τ, but we believe this particular choice is a good balance between accuracy and efficiency, and hence all the numerical simulations presented in the next chapters will be produced using this second-order scheme with $h = 0.1$ and $\tau = 0.001$.

Chapter 4

RLW and mRLW simulations

As discussed in subsection 1.3.3, we found one- and two-soliton solutions that solve the perturbed KdV equation only for certain values of ε_1 and ε_2. In this chapter, we discuss the numerical properties of multi-soliton systems that do not analytically solve the perturbed KdV equation. To construct such an N-soliton configuration, with $N \geq 2$, we use as initial conditions the superposition of N single-soliton solutions described by equation (1.3.30), that is,

$$q = \frac{3}{2+\varepsilon_2} \sum_{i=1}^{N} \ln\left(1 + e^{\Gamma_i}\right) , \tag{4.0.1}$$

while keeping $\varepsilon_1 = 1$.

4.1 Multi-soliton mRLW interactions

In this section, we investigate multi-soliton simulations governed by the mRLW equation (i.e., $\varepsilon_1 = \varepsilon_2 = 1$). Since we know the form of the analytical two-soliton solutions, we are particularly interested in the numerical three-soliton simulations. To construct a three-soliton system, we use the linear superposition of three one-soliton solutions as initial conditions, with the three solitons initially placed far apart from each other. We then determine the time evolution of such a system (using the second-order scheme discussed in section 3.3), and study its properties. However, to test this method, we first present the numerical time evolution of a simulation

using equation (4.0.1) as initial conditions, with $\varepsilon_2 = 1$ and $N = 2$, and compare it with the numerical time evolution of the exact two-soliton solution described by equation (1.3.38).

4.1.1 Two-soliton solutions

To this end, the superposition of two one-soliton solutions takes the following form

$$q = \ln\left(1 + e^{\Gamma_1}\right) + \ln\left(1 + e^{\Gamma_2}\right) . \tag{4.1.1}$$

The red curve in figure 4.1 shows the numerical time evolution of such a system. For comparison purposes, the green curve in figure 4.1 shows the numerical time evolution of equation (1.3.38), that is, this green curve is exactly the same as the green curve shown in figure 3.4. We cannot distinguish between the curves on the scale shown in the figure. In fact, the inset in figure 3.4f shows that even on a smaller scale, the two solutions are indistinguishable, which implies that the results are very

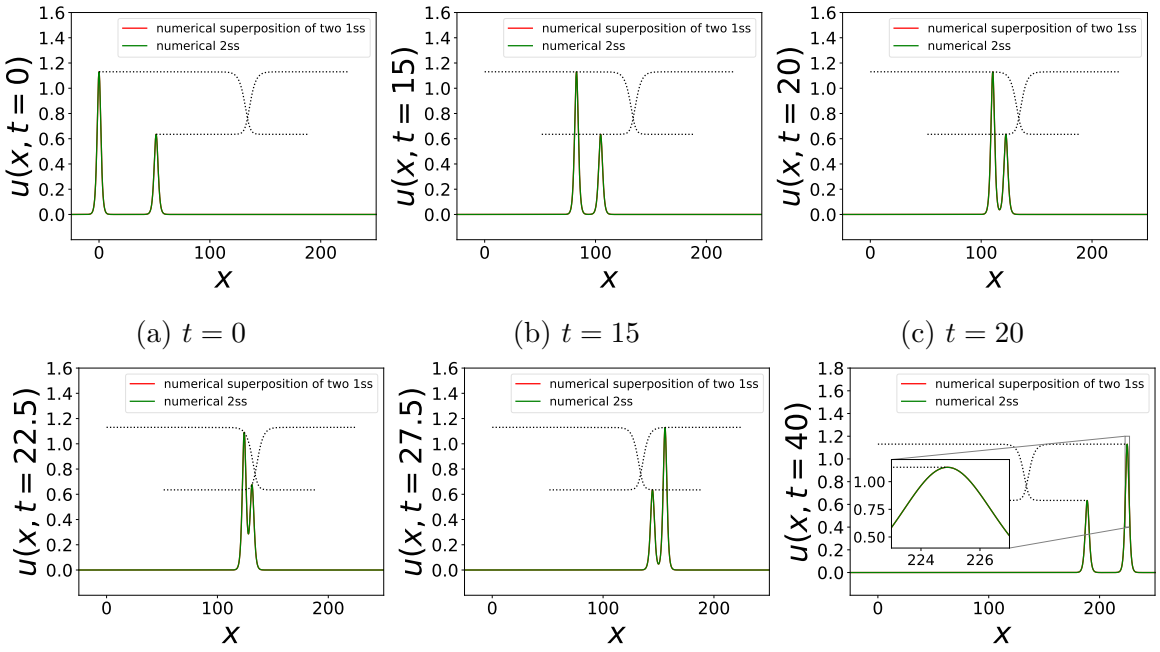

(a) $t = 0$ (b) $t = 15$ (c) $t = 20$

(d) $t = 22.5$ (e) $t = 27.5$ (f) $t = 40$

Figure 4.1: The red curve represents the numerical simulation constructed with the linear superposition of two mRLW single-soliton solutions, and the green curve shows the numerical time evolution of the corresponding analytical mRLW two-soliton solution.

reliable.

In this chapter, we also investigate the phase shifts that the numerical solitons experience. To find the phase shift, we numerically obtain the x- and t-dependence of the amplitudes of each of the solitons (see the footnote on page 45). Since the phase velocity of non-interacting solitons (i.e., before and after the collision) is approximately constant, we can use this data to numerically calculate the resulting spatial shift of each soliton. For the two-soliton mRLW solutions, we have an analytical expression for the phase shift (see subsection 1.3.3), and we will use this expression to determine the numerical phase shift from the aforementioned numerical spatial shift.

To this end, when the two solitons are far apart (i.e., before and after the collision), they can be approximated as the superposition of two single-soliton solutions. Therefore, let us find the expression for the location of a single soliton by setting the x-derivative of equation (1.3.32) (with $\varepsilon_2 = 1$) equal to zero, which yields

$$x = \frac{\omega_1 t - \delta_1}{k_1} \,. \tag{4.1.2}$$

This equation expresses how the location of a single soliton's amplitude, x, depends on time. Furthermore, a single soliton propagates with a constant velocity (see equation (1.3.34)), and so x satisfies the following linear relation

$$x = v_p^{(k_1)} t + x_0^{(k_1)} \,. \tag{4.1.3}$$

These equations are also valid for two-soliton systems, provided they are far apart from each other. Due to the phase shift, $x_0^{(k_1)}$ before the collision will be different than $x_0^{(k_1)}$ after the collision. To find an analytic expression for this difference, i.e., the spatial shift, we use equation (4.1.2) as follows

$$\begin{aligned} \Delta\, x_0^{(k_1)} &\equiv \lim_{t\to\infty} x_0^{(k_1)} - \lim_{t\to-\infty} x_0^{(k_1)} \\ &\approx \frac{\omega_1 t - (\delta_1 + \ln A_{12})}{k_1} - \frac{\omega_1 t - \delta_1}{k_1} = -\frac{\ln A_{12}}{k_1} \,, \end{aligned} \tag{4.1.4}$$

where A_{12} is defined by equation (1.3.37). Following the same procedure for the

soliton corresponding to k_2, we find that the analytical expression for its spatial shift is given by

$$\Delta\, x_0^{(k_2)} \approx \frac{\omega_2 t - (\delta_2 - \ln A_{12})}{k_2} - \frac{\omega_2 t - \delta_2}{k_2} = \frac{\ln A_{12}}{k_2}\,. \tag{4.1.5}$$

Now, let $\Delta\, x_0^{(k_i,\mathrm{n})}$ denote the numerically obtained spatial shift of the soliton corresponding to k_i. Furthermore, let δ_{12} denote the numerical phase shift of the soliton corresponding to k_1 after it has interacted with the soliton corresponding to k_2, where we assume that $k_1 > k_2$, and let δ_{21} denote the numerical phase shift that the soliton corresponding to k_2 experiences due to the same collision. Then, we have obtained the following relations

$$\delta_{12} = -k_1\, \Delta\, x_0^{(k_1,\mathrm{n})} \quad \text{and} \quad \delta_{21} = -k_2\, \Delta\, x_0^{(k_2,\mathrm{n})}\,. \tag{4.1.6}$$

Furthermore, we define the relative errors, $\epsilon^{(k_1)}$ and $\epsilon^{(k_1)}$, of the numerical phase shifts, δ_{12} and δ_{12}, as

$$\epsilon^{(k_1)} = \frac{|\delta_{12} - \ln A_{12}|}{|\ln A_{12}|} \quad \text{and} \quad \epsilon^{(k_2)} = \frac{|\delta_{21} + \ln A_{12}|}{|\ln A_{12}|}\,. \tag{4.1.7}$$

Using this method, we found that for both the red and the green curves presented in figure 4.1, the relative errors were $\epsilon^{(k_1)} = 1.97\%$ and $\epsilon^{(k_2)} = 0.34\%$ (i.e., the two simulations approximate each other so closely that the relative errors were the same for both simulations). These errors are a combination of the errors due to:

(i) the numerical second-order scheme discussed in section 3.3,

(ii) and the algorithm to obtain the x- and t-dependence of the solitons' amplitudes, as discussed in the footnote on page 45.

To eliminate the first error, we determined the numerical phase shift of the corresponding analytical values (see, for instance, the red curve in figure 3.4), and we found that $\epsilon^{(k_1)} = 4.91\%$ and $\epsilon^{(k_2)} = 3.36\%$. Thus, in this case, the relative errors for the analytical solution are significantly higher than for the numerical simulations, which implies that the algorithm to obtain the phase shift is fairly sensitive. To further illustrate this sensitivity, we have run additional analytical and numerical

simulations for various other values of ω_2 while keeping $\omega_1 = 5$ constant, and determined the relative errors of the phase shifts that the solitons experience. The corresponding relative errors $\epsilon^{(k_1)}$ are shown in figure 4.2, where the red dots represent the relative errors obtained for the analytical two-soliton solution described by equation (1.3.38), and the blue dots represent the relative errors observed for the corresponding numerical simulation. We have repeated these experiments with other values of ω_1 and ω_2, and we found that the relative errors always satisfy $\epsilon^{(k_1)} < 6\%$ and $\epsilon^{(k_2)} < 6\%$.

4.1.2 Three-soliton solutions

Armed with the results of the previous subsection, we now investigate the numerical time evolution of systems constructed by the linear superposition of three single-solitons, that is,

$$q = \ln\left(1 + e^{\Gamma_1}\right) + \ln\left(1 + e^{\Gamma_2}\right) + \ln\left(1 + e^{\Gamma_3}\right) . \tag{4.1.8}$$

Figure 4.3 shows the time evolution of such a simulation. The simulation starts at $t = 0$, i.e., figure 4.3a shows the system when it has already evolved for 34 units

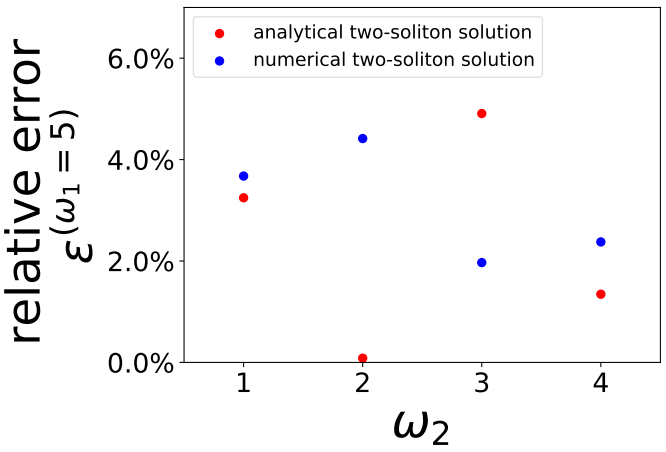

Figure 4.2: The vertical axis represents the relative errors $\epsilon^{(k_1)} \equiv \epsilon^{(\omega_1)}$, with $\omega_1 = 5$, that are experienced during various analytical and numerical mRLW two-soliton simulations, and the horizontal axis shows various values for ω_2 that were used for these simulations. The red dots are the relative errors due to the analytical two-soliton solution. Similarly, the blue dots are the errors obtained in the numerical two-soliton simulation.

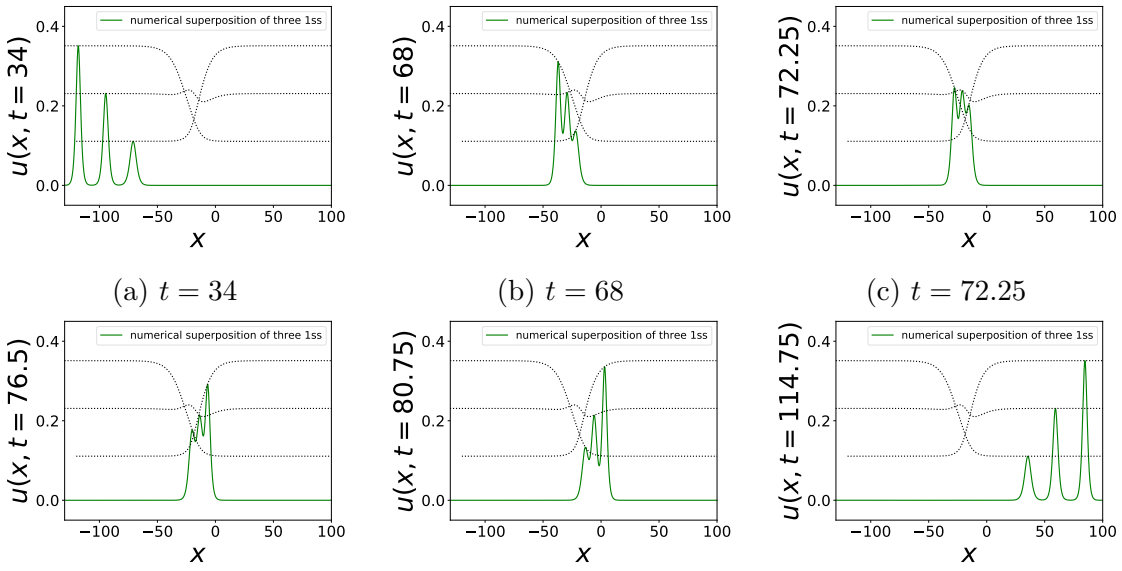

(a) $t = 34$ (b) $t = 68$ (c) $t = 72.25$

(d) $t = 76.5$ (e) $t = 80.75$ (f) $t = 114.75$

Figure 4.3: Numerical time evolution of a three-soliton system governed by the mRLW equation. Note that at all times during the simulation, there are three distinct maxima present.

of time. Figures 4.3b to 4.3e show how the three solitons interact with each other. Note that the solution's amplitude decreases during the collision, which is due to the nonlinearity of equation (1.1.1). Figure 4.3f shows the three solitons after they have scattered, and we see that the amplitudes and shapes of the solitons have not visibly changed. In fact, using equation (1.3.33), we found that the relative numerical error of the amplitude of each of the three solitons before and after the collision was less than 0.074%. Similarly, the numerical error of the velocity of each of the solitons (see equation (1.3.34)) was less than 0.12% before and after they interacted. Furthermore, we did not see any (visible) loss of radiation during the entire simulation. In figure 4.4a we have plotted how the amplitudes of the three solitons vary with time. This shows that the parameters of the simulation are such that there are three distinct solitons present at all times during the simulation. Furthermore, figure 4.4b shows the (numerically obtained) t-dependence of Q_1 and $Q_2^{\varepsilon_2}$ (see equations (1.1.10) and (1.1.11)). We see that they are indeed conserved for this numerical three-soliton simulation, and they approximate equations (1.3.39) and (1.3.40) very closely (with $N = 3$). In fact, using these equations, we found that the relative numerical error

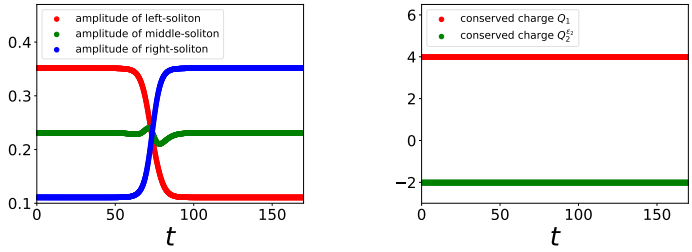

(a) (b)

Figure 4.4: The red dots in figure (a) illustrate the time-dependence of left-soliton's amplitude shown in figure 4.3; similarly, the green and blue dots, respectively, correspond to the middle- and right-soliton of the simulation. Figure (b) shows how the charges Q_1 and $Q_2^{\varepsilon_2}$ of the simulation vary with time.

for the conserved charges was smaller than 0.0001% at each time level during the simulation.

In figure 4.5 we show a different three-soliton mRLW simulation. For this simulation the parameters of the initial conditions are chosen such that the smallest soliton gets completely 'absorbed' during the three-soliton interaction (see, for instance, figure 4.5c). To better illustrate this, figure 4.6a shows how the amplitudes of the three solitons vary with time. From this plot we can see that from $t \sim 17$

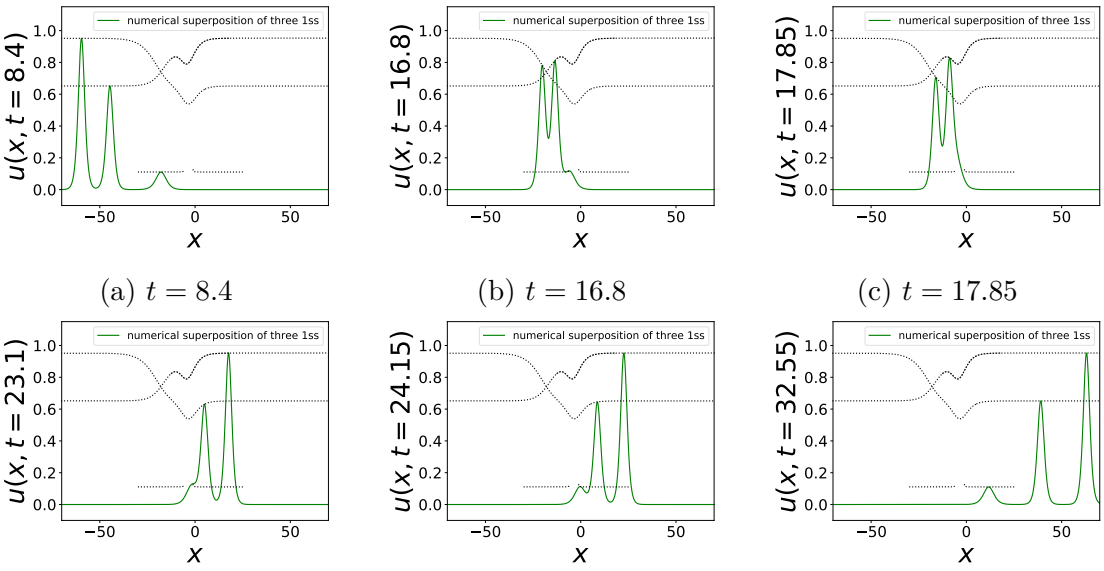

(a) $t = 8.4$ (b) $t = 16.8$ (c) $t = 17.85$

(d) $t = 23.1$ (e) $t = 24.15$ (f) $t = 32.55$

Figure 4.5: Numerical time evolution of a three-soliton system governed by the mRLW equation. Figure (c) illustrates that the smallest solitons get 'absorbed' during the collision.

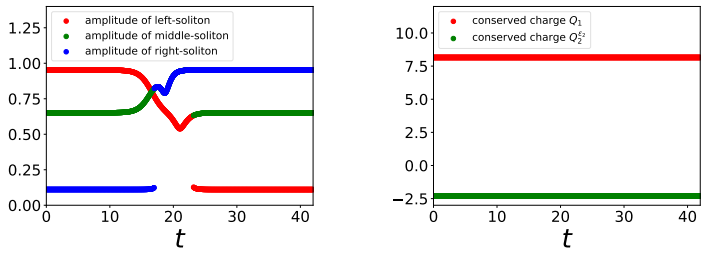

(a) (b)

Figure 4.6: The red dots in figure (a) illustrate the time-dependence of left-soliton's amplitude shown in figure 4.5; similarly, the green and blue dots, respectively, correspond to the middle- and right-soliton of the simulation. Figure (b) shows how the charges Q_1 and $Q_2^{\varepsilon_2}$ of the simulation vary with time.

to $t \sim 23$, the smallest wave gets absorbed during the three-soliton interaction and there are only two distinct maxima present. We see that after the collision, the solitons re-emerge with the same amplitudes and velocities. Figure 4.6b shows the corresponding charges Q_1 and $Q_2^{\varepsilon_2}$, which are also conserved for this simulation and approximate equations (1.3.39) and (1.3.40), for $N = 3$, very closely (just as for the previous simulation). To be precise, we found that the numerical errors of the amplitudes were less than 0.21%, of the soliton's velocities less than 0.11%, and of the charges Q_1 and $Q_2^{\varepsilon_2}$ less than 0.01%.

Thus, from the above two simulations, we see that the numerical solitons of the partial integrable mRLW equation share some of the properties that we observe for integrable models (see section 1.2). As we mentioned in section 1.2, the total phase shift of an integrable soliton due to an N-soliton interaction is equal to the total sum of the phase shifts due to separate two-soliton interactions with each of the other $N-1$ solitons involved. Assuming this also holds for the mRLW equation, then for a numerical three-soliton collision, with $k_1 > k_2 > k_3$, we expect that

$$\Delta\, x_0^{(k_1)} \approx \frac{\omega_1 t - (\delta_1 + \ln A_{12} + \ln A_{13})}{k_1} - \frac{\omega_1 t - \delta_1}{k_1} = -\frac{\ln A_{12} + \ln A_{13}}{k_1}\,, \tag{4.1.9}$$

$$\Delta\, x_0^{(k_2)} \approx \frac{\omega_2 t - (\delta_2 - \ln A_{12} + \ln A_{23})}{k_2} - \frac{\omega_2 t - \delta_2}{k_2} = \frac{\ln A_{12} - \ln A_{23}}{k_2}\,, \tag{4.1.10}$$

$$\Delta\, x_0^{(k_3)} \approx \frac{\omega_3 t - (\delta_3 - \ln A_{13} - \ln A_{23})}{k_3} - \frac{\omega_3 t - \delta_3}{k_3} = \frac{\ln A_{13} + \ln A_{23}}{k_3}\,. \tag{4.1.11}$$

Following the discussion in the previous subsection, let δ_{ijm} denote the numerical

phase shift which the soliton related to the wavenumber k_i experiences as a result of a three-soliton interaction with the other two solitons related to the wavenumbers k_j and k_m. Furthermore, let the numerically obtained spatial shift of the soliton corresponding to k_i be denoted by $\Delta x_0^{(k_i,\mathrm{n})}$. It then follows from the above three equations that

$$\delta_{123} = -k_1 \, \Delta x_0^{(k_1,\mathrm{n})} , \quad \delta_{213} = -k_2 \, \Delta x_0^{(k_2,\mathrm{n})} \quad \text{and} \quad \delta_{312} = -k_3 \, \Delta x_0^{(k_3,\mathrm{n})} . \tag{4.1.12}$$

We define the corresponding relative errors, $\epsilon^{(k_1)}$, $\epsilon^{(k_2)}$ and $\epsilon^{(k_3)}$, in a similar way as in the previous subsection, that is,

$$\epsilon^{(k_1)} = \frac{|\delta_{123} - \ln A_{12} - \ln A_{13}|}{|\ln A_{12} + \ln A_{13}|} , \quad \epsilon^{(k_2)} = \frac{|\delta_{213} + \ln A_{12} - \ln A_{23}|}{|-\ln A_{12} + \ln A_{23}|} , \tag{4.1.13}$$

and

$$\epsilon^{(k_3)} = \frac{|\delta_{312} + \ln A_{13} + \ln A_{23}|}{|\ln A_{13} + \ln A_{23}|} . \tag{4.1.14}$$

For the simulation shown in figure 4.3, we found that $\epsilon^{(k_1)} = 1.92\%$, $\epsilon^{(k_2)} = 4.72\%$ and $\epsilon^{(k_3)} = 1.75\%$. And for the time evolution corresponding to figure 4.5, we observed that $\epsilon^{(k_1)} = 0.69\%$, $\epsilon^{(k_2)} = 0.19\%$ and $\epsilon^{(k_3)} = 0.10\%$. We observed similar relative errors for various other three-soliton simulations, which indicates that the phase shifts due to multi-soliton collisions can be explained by the additivity of 'two-particle' effects.

To sum up, the simulations discussed in this subsection have shown that the partial integrable mRLW equation admits numerical three-soliton solutions. The resulting solitons evolve very similar to integrable solitons in the sense that there is no particle creation or destruction and the solitons scatter elastically with each other during a three-soliton interaction. Furthermore, we also see that the phase shift is additive (with a numerical error of less than 6%).

4.2 Multi-soliton RLW interactions

As discussed in section 1.1, the RLW equation admits only one-soliton solutions, which are expressed by equation (1.3.30) with $\varepsilon_2 = 0$. Therefore, to study multi-soliton systems governed by the RLW equation, we use numeric procedures. The numeric solutions of the RLW have been extensively studied [3, 7, 8, 20, e.g.]. In this section, we briefly present the two- and three-soliton simulations with the intent to discuss their quasi-integrability properties in chapter 6.

4.2.1 Two-soliton solutions

To construct an RLW two-soliton simulation, we use the methods discussed in the previous section. Thus, we use equation (4.0.1), with $\varepsilon_2 = 0$ and $N = 2$, as initial conditions. Figure 4.7 shows such a simulation, which has been constructed with the same angular parameters (i.e., k_1, k_2, δ_1, and δ_2) used to produce figure 4.1 (see appendix A). Figure 4.7a shows the start of the simulation, and figures 4.7b to 4.7f show the numerical time evolution at various points in time. The simulation showed

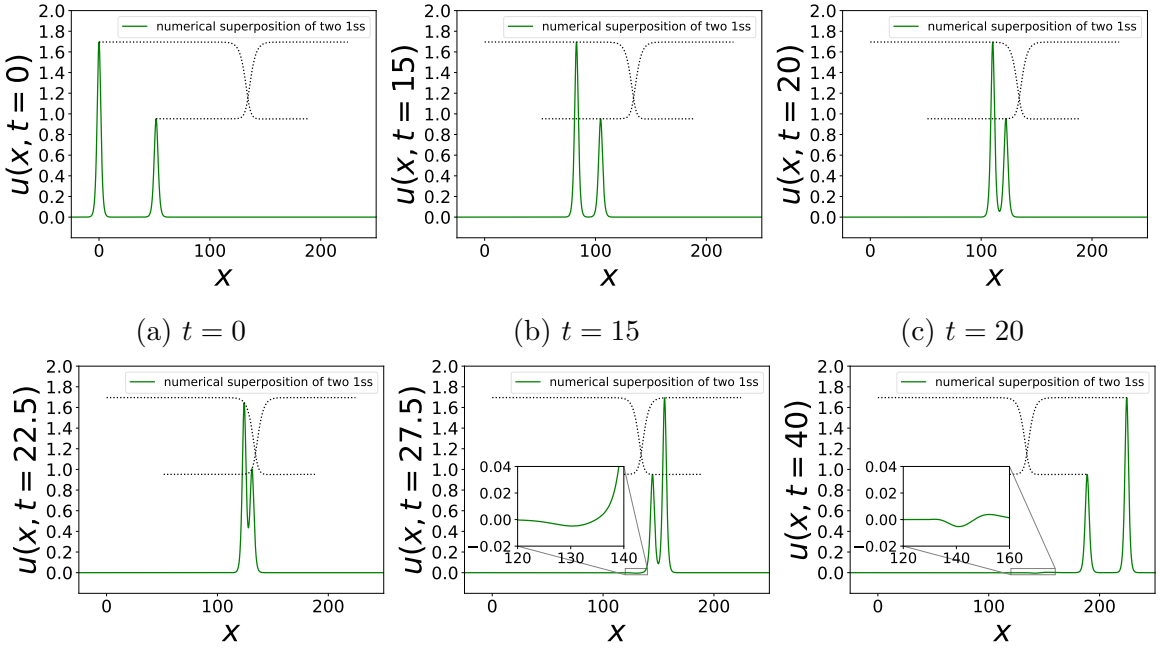

(a) $t = 0$ (b) $t = 15$ (c) $t = 20$

(d) $t = 22.5$ (e) $t = 27.5$ (f) $t = 40$

Figure 4.7: Numerical time evolution of a two-soliton system governed by the RLW equation.

that immediately after the largest soliton passed the smallest soliton, the smallest soliton emitted a small amount of (visible) radiation. To illustrate this, the insets in figure 4.7e and 4.7f show the radiation at a smaller scale. These observations agree with the results presented in [3, 20].

Figure 4.8 shows the corresponding numerical conserved charges (see equations (1.1.6) to (1.1.8)). We thus see that the quantities are independent in time (up to small numerical errors) for RLW two-soliton simulations. Using equation (1.3.33) with $\varepsilon_2 = 0$, we found that the relative error for each soliton's amplitude was less than 0.11%, and the relative errors of the velocities were found to be less than 0.12%. These errors are very small, and so we see that the (small) loss of radiation did not have a significant impact on these variables. Since there is no analytic two-soliton expression that solves the RLW equation, we do not have an analytical expression for the phase shift. However, when we used the relative errors defined by equation (4.1.7), we found that $\epsilon^{(k_1)} = 8.27\%$ and $\epsilon^{(k_2)} = 0.25\%$. Furthermore, just as in subsection 4.1.1, we have determined the relative errors for various simulations using different values for ω_2 while keeping $\omega_1 = 5$ constant. The results are shown in figure 4.9. From this, it appears that the phase shift due to a two-soliton RLW interaction can be approximated by $\ln A_{12}$, provided that $|\omega_1 - \omega_2|$ is sufficiently small. However, more research needs to be done to draw definite conclusions.

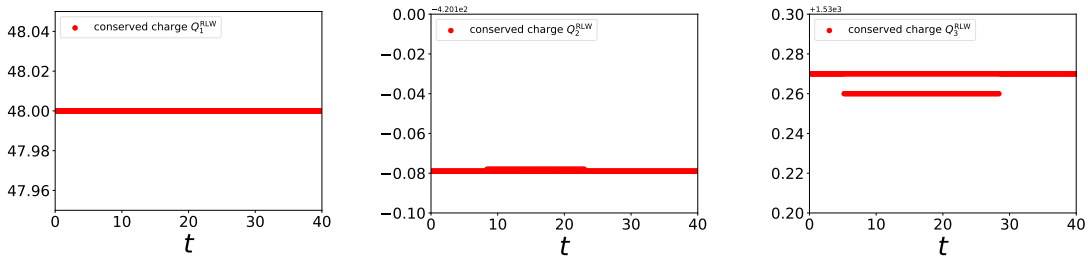

(a) (b) (c)

Figure 4.8: The time-dependence of the charges Q_1^{RLW}, Q_2^{RLW} and Q_3^{RLW} from the RLW two-soliton simulation shown in figure 4.7.

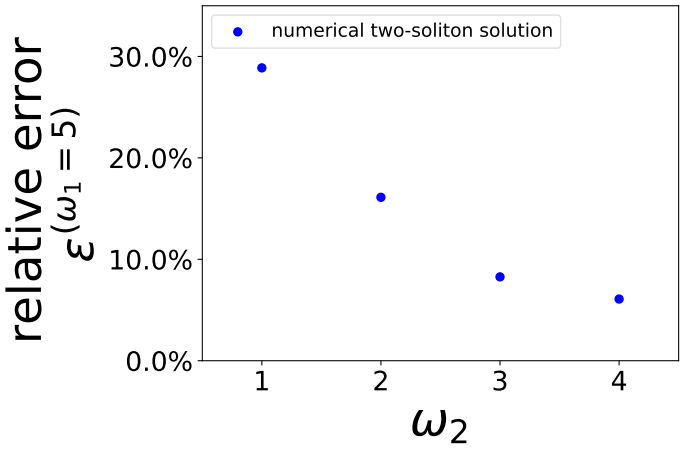

Figure 4.9: The vertical axis represents the relative errors $\epsilon^{(k_1)} \equiv \epsilon^{(\omega_1)}$, with $\omega_1 = 5$, that are experienced during various numerical RLW two-soliton simulations, and the horizontal axis shows various values for ω_2 that were used for these simulations.

4.2.2 Three-soliton solutions

Figure 4.10 shows the numerical time evolution of a system constructed using the superposition of three single-soliton RLW solutions. This simulation was run with the same angular parameters used to produce figure 4.3. The results show that after the three-soliton collision, the smallest soliton emits some (visible) radiation

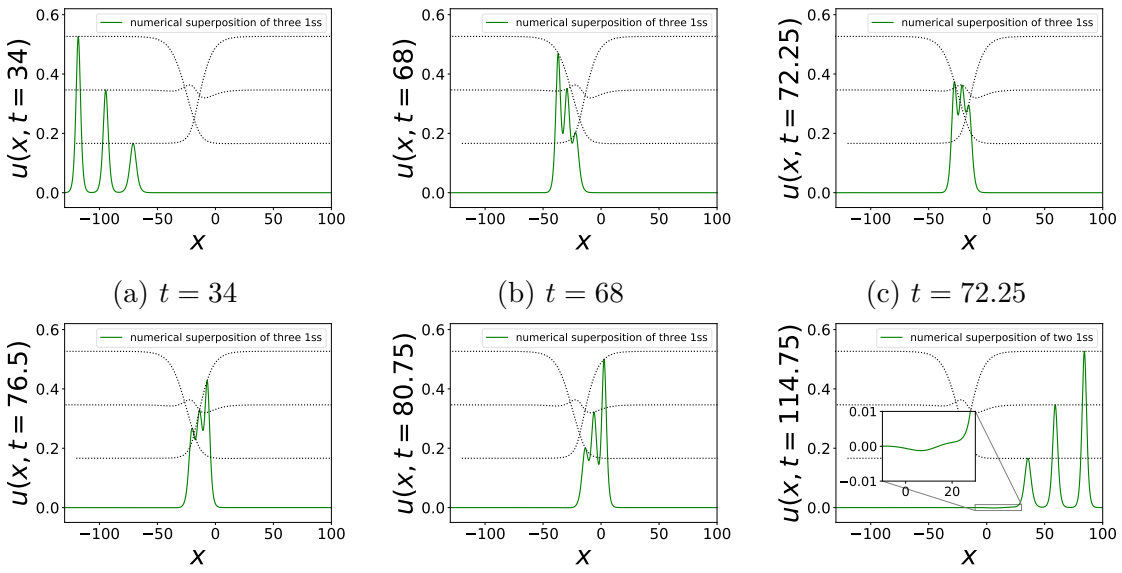

(a) $t = 34$ (b) $t = 68$ (c) $t = 72.25$

(d) $t = 76.5$ (e) $t = 80.75$ (f) $t = 114.75$

Figure 4.10: Numerical time evolution of a three-soliton system governed by the RLW equation. Note that at all times during the simulation, there are three distinct maxima present.

(see figure 4.10f), which is comparable with the two-soliton simulation. Numerical analysis of Q_1^{RLW}, Q_2^{RLW} and Q_3^{RLW} showed that they were conserved at about the same order as for the two-soliton simulation discussed in the previous subsection. Furthermore, we found that the errors of the amplitudes were less than 0.13%, and the errors of the phase velocities were less than 0.089%. As mentioned in the previous subsection, we do not have an analytic expression for the phase shift, and so we have used equations (4.1.13) and (4.1.14) to determine that $\epsilon^{(k_1)} = 5.34\%$, $\epsilon^{(k_2)} = 8.97\%$ and $\epsilon^{(k_3)} = 0.48\%$.

Figure 4.11 shows the RLW simulation corresponding to figure 4.5, with $\varepsilon_2 = 0$. We found that the relative errors of the solitons' amplitudes and velocities (before and after the collision) to be less than 1.22% and 0.54%, respectively. For the phase shift, we found that $\epsilon^{(k_1)} = 11.47\%$, $\epsilon^{(k_2)} = 8.13\%$ and $\epsilon^{(k_3)} = 3.40\%$.

To sum up, the main difference between the numerical RLW and mRLW solutions is that the RLW solitons emits some visible radiation, whereas for the mRLW simulations we did not see any visible loss of radiation. Furthermore, using the analytical expression for the phase shift of the exact two-soliton mRLW solution,

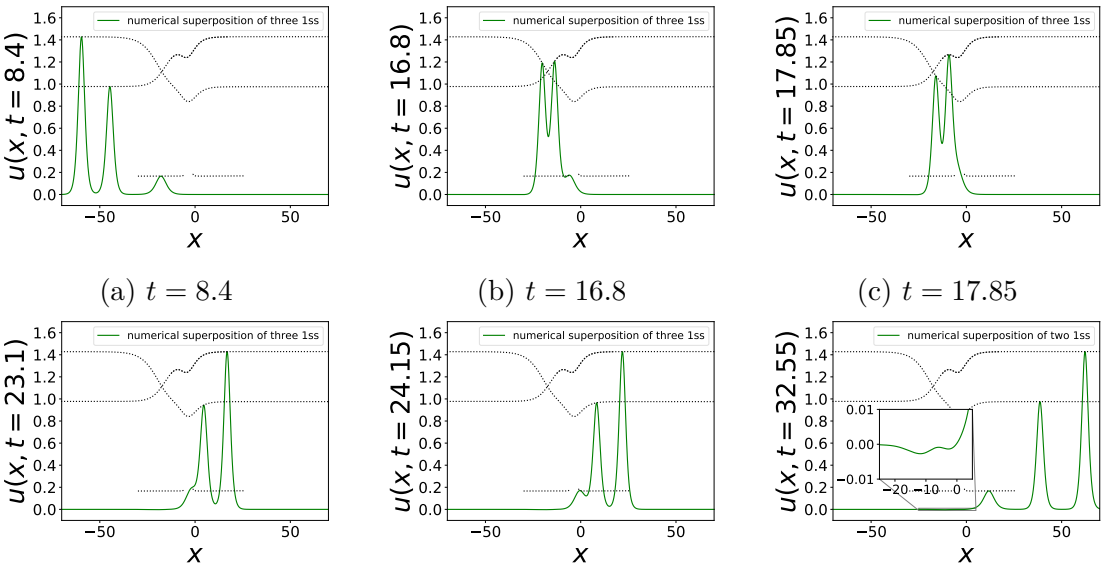

(a) $t = 8.4$ (b) $t = 16.8$ (c) $t = 17.85$

(d) $t = 23.1$ (e) $t = 24.15$ (f) $t = 32.55$

Figure 4.11: Numerical time evolution of a three-soliton system governed by the RLW equation. Figure (c) illustrates that the smallest solitons get 'absorbed' during the collision.

we have determined that the phase shift of the numerical three-soliton interaction governed by the mRLW equation is additive (within a numerical error of 6%). On the other hand, since we do not have an analytic expression for the phase shift of RLW solitons, it is more complicated. If we look at the numerical observed errors $\epsilon^{(k_1)}$, $\epsilon^{(k_2)}$ and $\epsilon^{(k_3)}$ presented in this section, and compare it with the results presented in section 4.1, we see that overall the errors are significantly larger. However, it does appear the RLW phase shift approximates the mRLW phase shift to within a certain degree, provided $|k_1 - k_2|$ is small enough.

4.3 General initial pulses

In this section, we test the soliton resolution conjecture for the mRLW and RLW equation. As mentioned in section 1.2, we want to test if any arbitrary initial pulse will eventually decouple in a stable system composed of soliton- and radiation-like components.

To test this conjecture, we use the following initial conditions

$$q = -t\,\mathrm{erf}(0.5x) \implies u = \frac{1}{\sqrt{\pi}} \exp\left(-x^2\right) . \tag{4.3.1}$$

The time evolution of this system governed by the mRLW equation (i.e., $\varepsilon_1 = \varepsilon_2 = 1$) is shown in figure 4.12. Unlike before, the simulation now starts at $t = 1$, which is shown in figure 4.12a. The dotted line shows the trajectory of the Gaussian function's amplitude, which shows that it initially decreases sharply, and subsequently stabilises at some constant value. This happens while the initial conditions decouple into soliton- and radiation-like components, as shown in figures 4.12b and 4.12c. As time progresses, the radiation's amplitude starts to increase. This can be seen by comparing figure 4.12e with figure 4.12f, which shows that the amplitude of the radiation-like structure has grown significantly during a short period of time. In fact, the whole system blows up at $t \approx 67.2$. We have run this simulation with various different grid spacings and time steps, and found that the system always blew up at

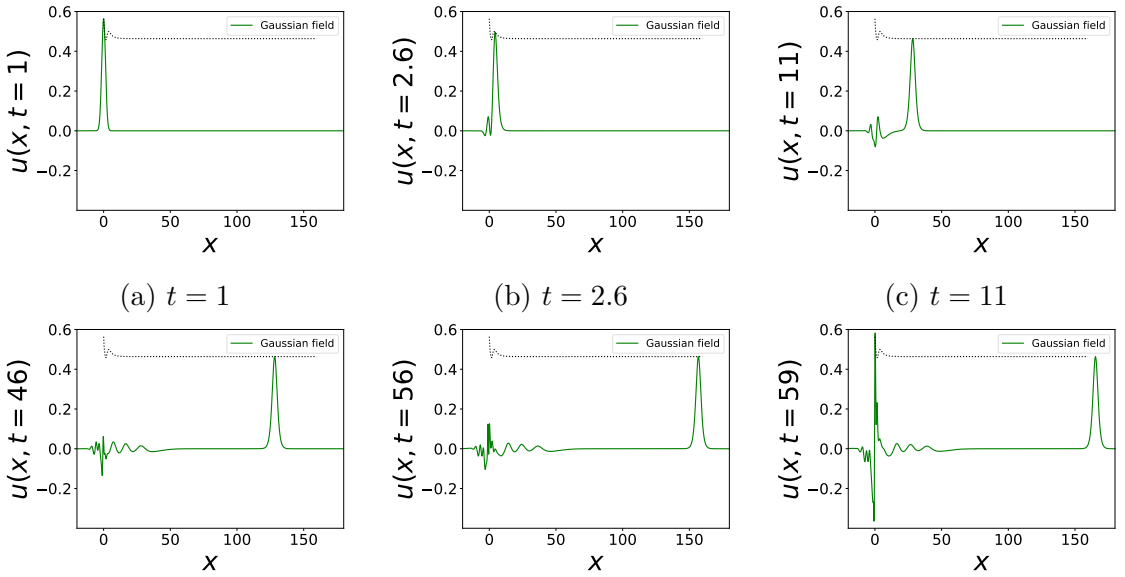

(a) $t = 1$ (b) $t = 2.6$ (c) $t = 11$

(d) $t = 46$ (e) $t = 56$ (f) $t = 59$

Figure 4.12: The time evolution of a Gaussian function governed by the mRLW equation.

(approximately) the same t. Therefore, we believe that the blow-up is not a result of instabilities due to the second-order finite difference method.

Thus, we see that the soliton resolution conjecture does not hold for the mRLW equation. We have also investigated the time evolution of these initial conditions, and various others, governed by the RLW equation (i.e., $\varepsilon_1 = 1$ and $\varepsilon_2 = 0$), and found that they also decouple into soliton- and radiation-like components. However, none of the initial pulses governed by the RLW equation blew up. This suggests that the conjecture may hold for the RLW model, which is consistent with the results obtained in [8]. This difference between the RLW and mRLW models might be because, to our knowledge, the mRLW equation does not admit a Hamiltonian structure, which potentially controls and limits the growth of the radiation-like components.

Chapter 5

Perturbed RLW and mRLW simulations

As we mentioned in section 1.2, integrability also manifests itself in the stability of perturbed solitons. Therefore, in this chapter, we investigate the nonintegrable mRLW and RLW models in the presence of perturbation terms. To be specific, we study various one-, two- and three-soliton mRLW and RLW configurations in the presence of perturbing terms determined by ε_1 and ε_2. The quasi-integrability properties of these perturbed soliton simulations will be discussed in chapter 6.

5.1 Perturbations of mRLW solutions

Let us first focus on the mRLW equation. To study its perturbations, we rewrite equation (1.1.1) as

$$u_t + u_x + \left[\frac{\alpha}{2}u^2 + \frac{\alpha}{4}w_x v_t - u_{xt}\right]_x = \left[\chi_2 \frac{\alpha}{4} w_x v_t - \chi_1 \left(u_{xx} - u_{xt}\right)\right]_x , \qquad (5.1.1)$$

where we have defined χ_1 and χ_2 by

$$\chi_1 = 1 - \varepsilon_1 \quad \text{and} \quad \chi_2 = 1 - \varepsilon_2 \, . \qquad (5.1.2)$$

Since the left-hand side of equation (5.1.1) is equivalent to the mRLW partial differential operator, we can think of u as a solution governed by the mRLW equation

in the presence of an additional external force that is described by the right-hand side of equation (5.1.1). The parameters χ_1 and χ_2 determine the magnitude of the perturbing terms.

5.1.1 One-soliton solutions

We start by investigating one-soliton systems governed by the perturbed mRLW equation. To this end, we construct the initial conditions using the family of one-soliton solutions that exactly solve the left-hand side of equation (5.1.1), that is,

$$q = \ln\left(1 + e^{\Gamma_1}\right) . \tag{5.1.3}$$

Using various different values of χ_1 and χ_2, we then let this system numerically evolve according to the second-order algorithm .

Figure 5.1 shows three different simulations; figures 5.1a to 5.1c are perturbed through $\chi_1 = 0$ and $\chi_2 = 0.1$, figures 5.1d to 5.1f through $\chi_1 = 0$ and $\chi_2 = 0.7$, and figures 5.1g to 5.1i through $\chi_1 = 0$ and $\chi_2 = 1$. For all three simulations, we see that the initial soliton emits a small amount of visible radiation shortly after the start of the simulation (see the insets in figures 5.1b, 5.1e and 5.1h). Comparing the insets shown in figures 5.1c, 5.1f and 5.1i, it appears that the radiation becomes larger as χ_2 becomes larger. Particularly, the radiation emitted when $\chi_2 = 1$ is significantly larger than for the simulations corresponding to $\chi_2 = 0.1$ and $\chi_2 = 0.7$. As usual, the dotted line shows the trajectory of the soliton's amplitude. We see that for all three simulations, the amplitude slightly decreases immediately after the simulation has started, and then stabilises after the soliton has emitted the radiation-like component. We have found that when we increase χ_2 from 0 to 0.7 in increments of 0.1, the soliton's amplitude decreases more when χ_2 increases. However, when χ_2 increases from 0.7 to 1 in increments of 0.1, the soliton's amplitude starts to decrease less. We have illustrated this effect in figure 5.2. Figure 5.2a shows the trajectory of the perturbed soliton's amplitude for χ_2 ranging from 0 to 0.7. We see that the amplitude of the soliton decreases more when the perturbation through χ_2

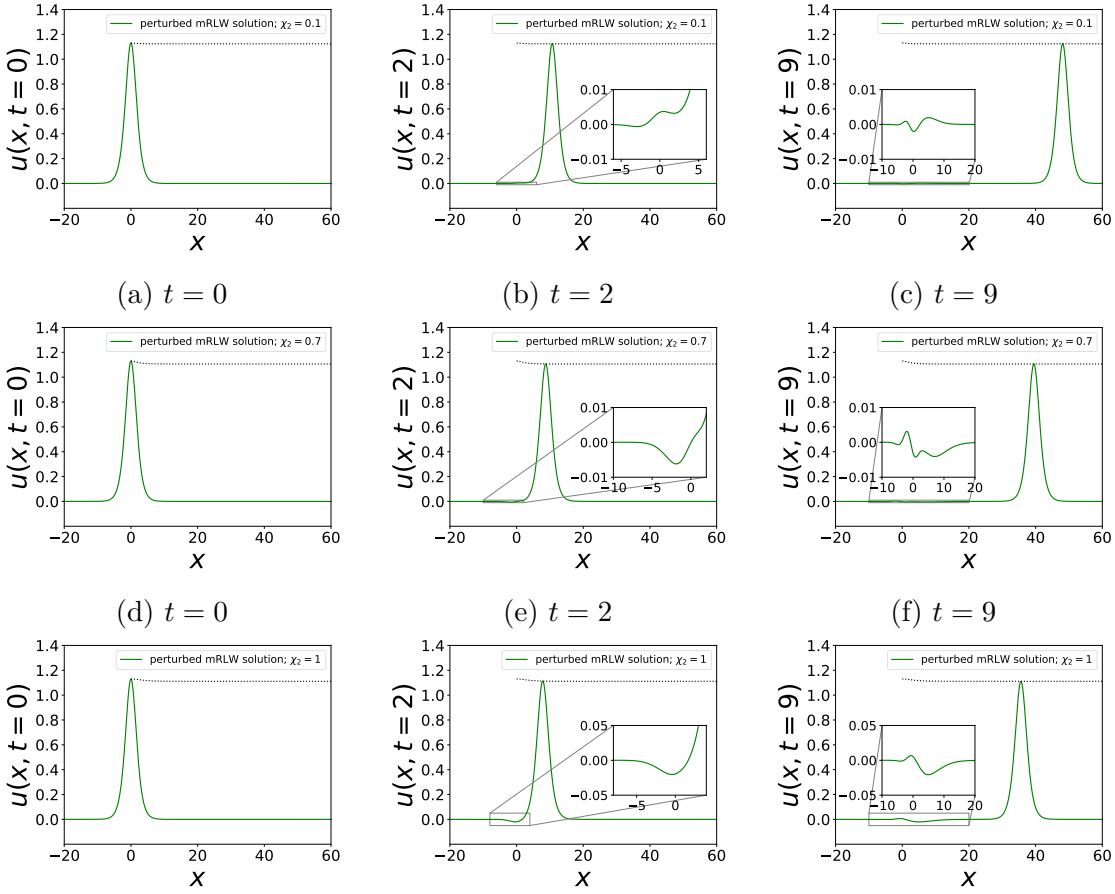

(a) $t = 0$ (b) $t = 2$ (c) $t = 9$

(d) $t = 0$ (e) $t = 2$ (f) $t = 9$

(g) $t = 0$ (h) $t = 2$ (i) $t = 9$

Figure 5.1: Figures (a) to (c) show the time evolution of an mRLW one-soliton solution perturbed through $\chi_1 = 0$ and $\chi_2 = 0.1$. Similarly, figures (d) to (f) show the time evolution perturbed through $\chi_1 = 0$ and $\chi_2 = 0.7$, and figures (g) to (i) show the simulation perturbed through $\chi_1 = 0$ and $\chi_2 = 1$.

increases. This can be explained by the fact that the initial conditions are a more 'accurate' solution to the perturbed equations of motion when the perturbation is small. Figure 5.2b shows how the amplitude varies when χ_2 is increased from 0.7

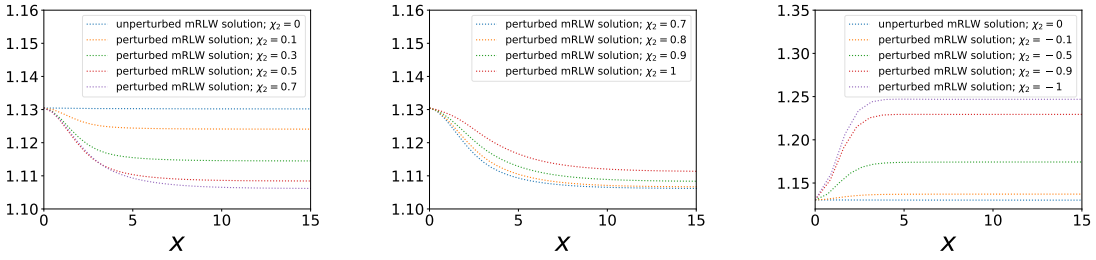

(a) (b) (c)

Figure 5.2: The trajectories of an mRLW soliton's amplitude perturbed through various values of χ_2 while keeping $\chi_1 = 0$ constant.

to 1. Surprisingly, we see that as the perturbation becomes larger in this range, the amplitude decreases less in magnitude. Finally, for future reference, we have also plotted a simulation produced with $\chi_2 = 0.5$, which is shown in figure 5.3.

Furthermore, for all these simulations we have analysed the charges introduced in section 1.1. We found that Q_1 and $Q_2^{\varepsilon_2}$ are incredibly well conserved. However, as shown in figure 5.4, the charges Q_2^{RLW} and Q_3^{RLW} are not conserved in general. It is interesting to point out that as the perturbation parameter χ_2 gets closer to the RLW equation, the quantities Q_2^{RLW} and Q_3^{RLW} become 'better' conserved. This is expected because these charges are only exactly conserved for the RLW equation.

We have also investigated these perturbations with $\chi_2 < 0$ while keeping $\chi_1 = 0$. For these simulations, we found that the amplitude of the initial soliton increases (instead of decreasing) while it emits radiation. Figure 5.5 shows an example of such a simulation with $\chi_2 = -0.5$, and figure 5.2c shows the various trajectories of a soliton's amplitude that is perturbed through various values of $\chi_2 < 0$. Upon analysing the charges, we also found the same behaviour in the sense that Q_1 and $Q_2^{\varepsilon_2}$ were conserved, whereas Q_2^{RLW} and Q_3^{RLW} were not conserved, as shown in figure 5.4.

For all the values of χ_2 discussed so far, we see that the initial configuration in the presence of a perturbation through χ_2 evolves into a long-lived system consisting of soliton- and radiation-like components. However, we found that as we decrease χ_2 from 0 to -1 in increments of 0.1, the system blows up when $\chi_2 \leq -0.8$. To illustrate this, figure 5.6 shows such a simulation for $\chi_2 = -0.9$. We see that initially, the soliton behaves similar as the solitons discussed in the previous simulations in

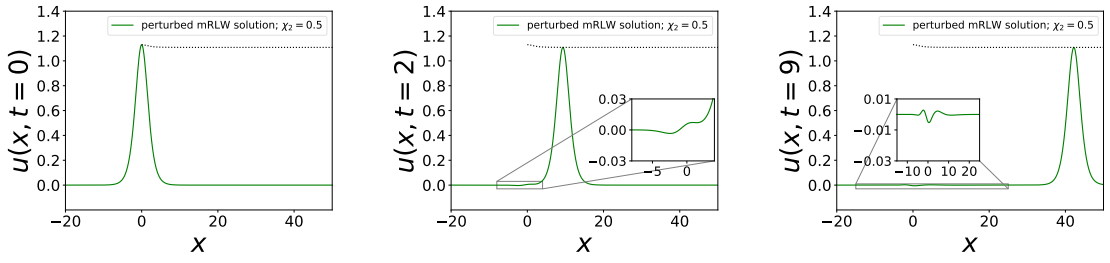

(a) $t = 0$ (b) $t = 2$ (c) $t = 9$

Figure 5.3: The time evolution of an mRLW one-soliton solution perturbed through $\chi_1 = 0$ and $\chi_2 = 0.5$.

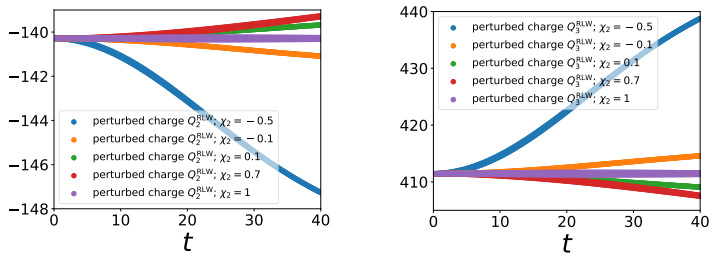

(a) (b)

Figure 5.4: The time-dependence of the quantities Q_2^{RLW} and Q_3^{RLW} observed for various mRLW one-soliton simulations perturbed through χ_2 while keeping $\chi_1 = 0$ constant.

the sense that the initial soliton emits some radiation in the beginning while its amplitude increases slightly, and then it stabilises. However, looking at the insets in figures 5.6b to 5.6e, we see that the amplitude of the radiation-like structure is slowly increasing. The amplitude keeps increasing, as shown in figure 5.6f, until the system blows up at around $t \approx 22.8$.

We have furthermore investigated the perturbations of the mRLW one-soliton solution for various values of $\chi_1 \neq 0$ while keeping $\chi_2 = 0$. Figure 5.7 show two of such simulations; figures 5.7a to 5.7c show the time evolution perturbed through $\chi_1 = 0.5$ and $\chi_2 = 0$, and figures 5.7d to 5.7f through $\chi_1 = -0.5$ and $\chi_2 = 0$. From this, we see that the initial soliton changes its shape after emitting radiation. The amplitude of the soliton increases initially if $\chi_1 > 0$, and it decreases if $\chi_1 < 0$. To illustrate this in more detail, figure 5.8 shows how the trajectory of the initial soliton

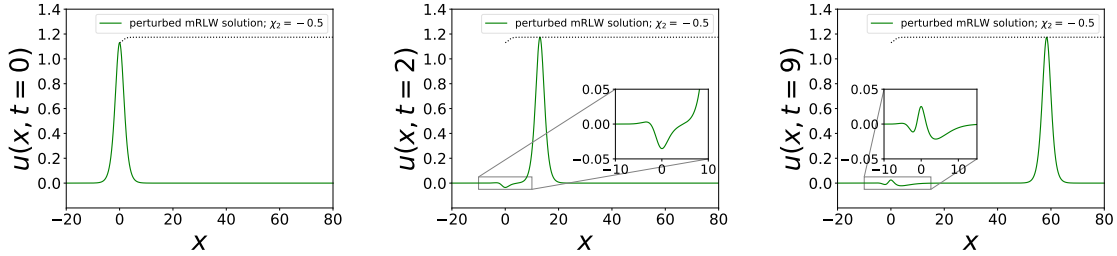

(a) $t = 0$ (b) $t = 2$ (c) $t = 9$

Figure 5.5: The time evolution of an mRLW one-soliton solution perturbed through $\chi_1 = 0$ and $\chi_2 = -0.5$.

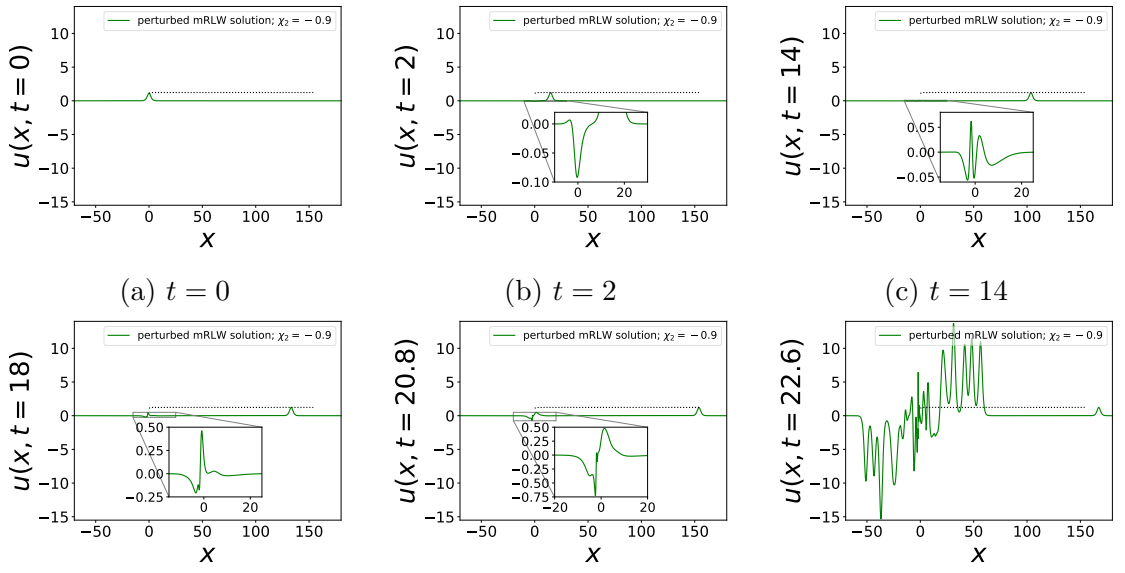

(a) $t = 0$ (b) $t = 2$ (c) $t = 14$

(d) $t = 18$ (e) $t = 20.8$ (f) $t = 22.6$

Figure 5.6: The time evolution of an mRLW one-soliton solution perturbed through $\chi_1 = 0$ and $\chi_2 = -0.9$, shown at a larger scale to illustrate the blow-up of the system.

changes for various values of χ_1.[1] This shows that as $|\chi_1|$ increases, the initial soliton's amplitude changes more rapidly. In this respect, simulations perturbed

[1]Note that our algorithm cannot solve the equations of motion when $\chi_1 = 1$, because then both the upper and lower diagonal of the tridiagonal matrix A (see equation (3.3.4)) vanish.

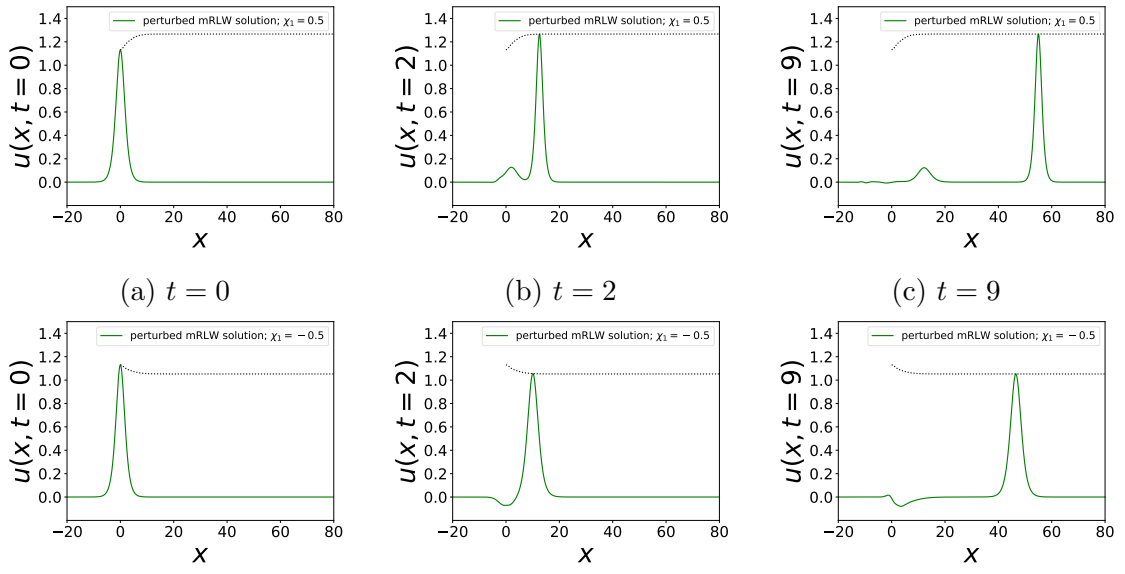

(a) $t = 0$ (b) $t = 2$ (c) $t = 9$

(d) $t = 0$ (e) $t = 2$ (f) $t = 9$

Figure 5.7: Figures (a) to (c) show the time evolution of an mRLW one-soliton solution perturbed through $\chi_1 = 0.5$ and $\chi_2 = 0$. Similarly, figures (d) to (f) show the simulation perturbed through $\chi_1 = -0.5$ and $\chi_2 = 0$.

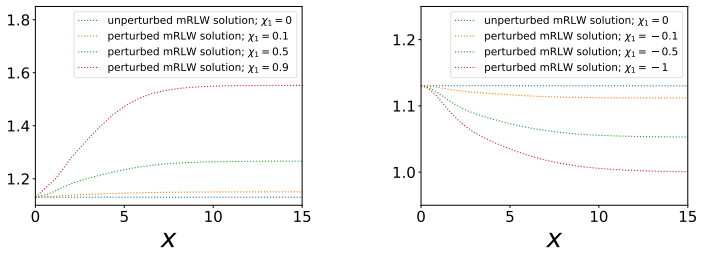

(a) (b)

Figure 5.8: The trajectories of an mRLW soliton's amplitude perturbed through various values of χ_1 while keeping $\chi_2 = 0$ constant.

through χ_1 differ from the simulations perturbed through χ_2 (see the discussion on page 68).

5.1.2 Two-soliton solutions

In the previous subsection, we discussed how an mRLW one-soliton solution evolves in the presence of perturbing terms governed by χ_1 and χ_2. We have seen that, provided χ_1 and χ_2 are relatively small, the perturbed systems result in long-lived localised structures after the initial configuration has emitted some radiation. In this subsection, we investigate the stability properties of mRLW two-soliton systems in the presence of perturbations through χ_1 and χ_2. That is, we take the following initial conditions

$$q = \ln\left(1 + e^{\Gamma_1} + e^{\Gamma_2} + A_{12}e^{\Gamma_1+\Gamma_2}\right) , \tag{5.1.4}$$

and obtain the numerical time evolution for various different values of χ_1 and χ_2.

Figures 5.9 and 5.10 show two of such simulations; figure 5.9 was produced with $\chi_1 = 0$ and $\chi_2 = 0.5$, and figure 5.10 with $\chi_1 = 0$ and $\chi_2 = -0.5$. Looking at the simulation corresponding to $\chi_2 = 0.5$, we see that the two initial solitons both emit some visible radiation while their amplitudes decrease. Note that the inset in figure 5.9b shows the radiation emitted by the smallest initial soliton. Subsequently, the largest soliton interacts with this radiation, which causes the amplitude of the largest soliton to alter slightly (see the inset in figure 5.9c). After this interaction, the soliton's amplitude returns to its original magnitude, as shown in figure 5.9d.

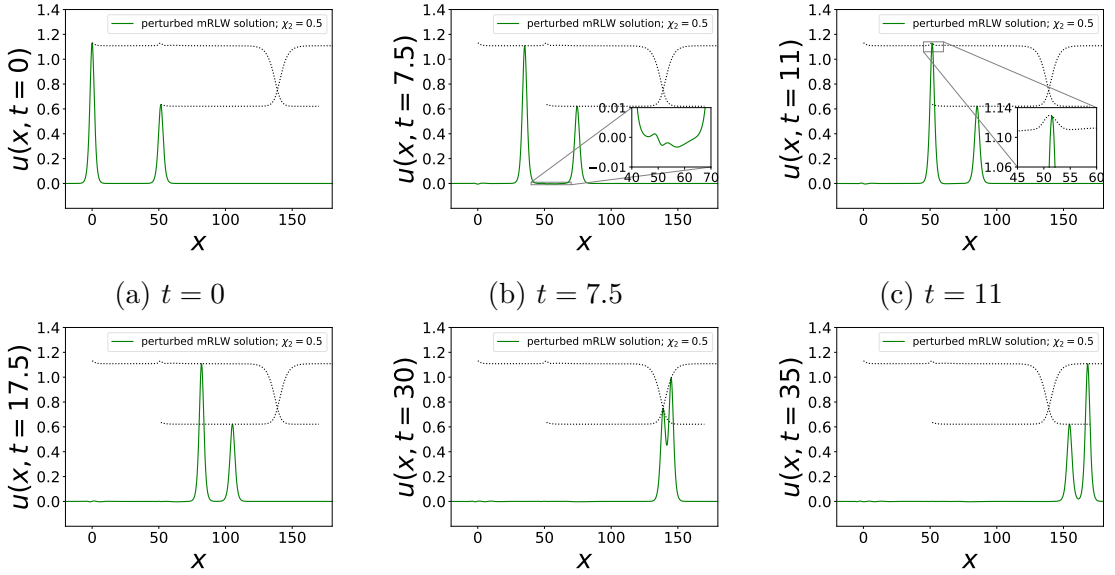

(a) $t = 0$ (b) $t = 7.5$ (c) $t = 11$

(d) $t = 17.5$ (e) $t = 30$ (f) $t = 35$

Figure 5.9: The time evolution of an mRLW two-soliton solution perturbed through $\chi_1 = 0$ and $\chi_2 = 0.5$.

Next, figure 5.9e shows how the soliton-like structures interact with each other. Note that the total amplitude decreases while they interact, whereas this is not necessarily true for the soliton-radiation collision (see the inset in figure 5.9c). Furthermore, figure 5.9f shows that the solitons' amplitudes return to their original values. For

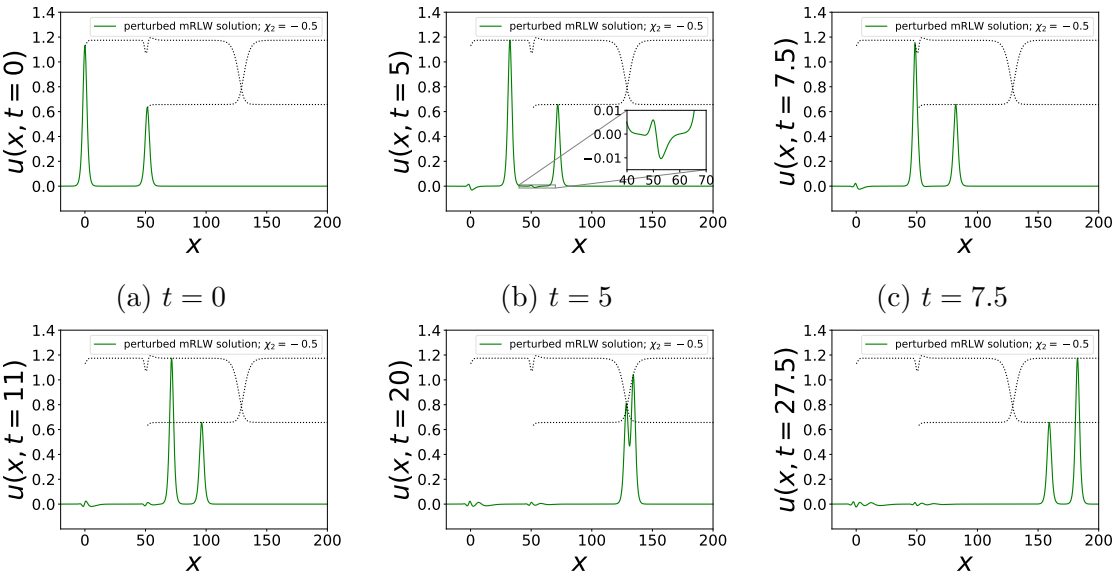

(a) $t = 0$ (b) $t = 5$ (c) $t = 7.5$

(d) $t = 11$ (e) $t = 20$ (f) $t = 27.5$

Figure 5.10: The time evolution of an mRLW two-soliton solution perturbed through $\chi_1 = 0$ and $\chi_2 = -0.5$.

the simulation perturbed through $\chi_2 = -0.5$, we observe similar behaviour, with the main difference that the initial solitons increase their amplitude when they emit radiation.

Figures 5.11 and 5.12 show the two-soliton mRLW simulations perturbed through $\chi_1 = 0.5$ and $\chi_1 = -0.5$, respectively, with $\chi_2 = 0$ for both simulations. The behaviour of these solutions is very similar in the sense that the initial solitons emit radiation while increasing or decreasing their amplitude slightly. Next, the largest soliton interacts with the radiation emitted by the smallest soliton. This causes the amplitude of the soliton-like structure to change slightly, but after the interaction it emerges with the same amplitude as before the collision. Finally, the two soliton structures interact with each other in a (nearly) elastic manner.

In all of the above two-soliton simulations, we have observed that during the soliton-radiation interactions, the total amplitude is sometimes higher than the soliton's amplitude before or after the interaction. This property has only been observed for radiation scattering with other soliton- or radiation-like structures. On the other hand, for perturbed soliton-soliton interactions, we see that the total amplitude always decreases, similar to the unperturbed soliton solutions.

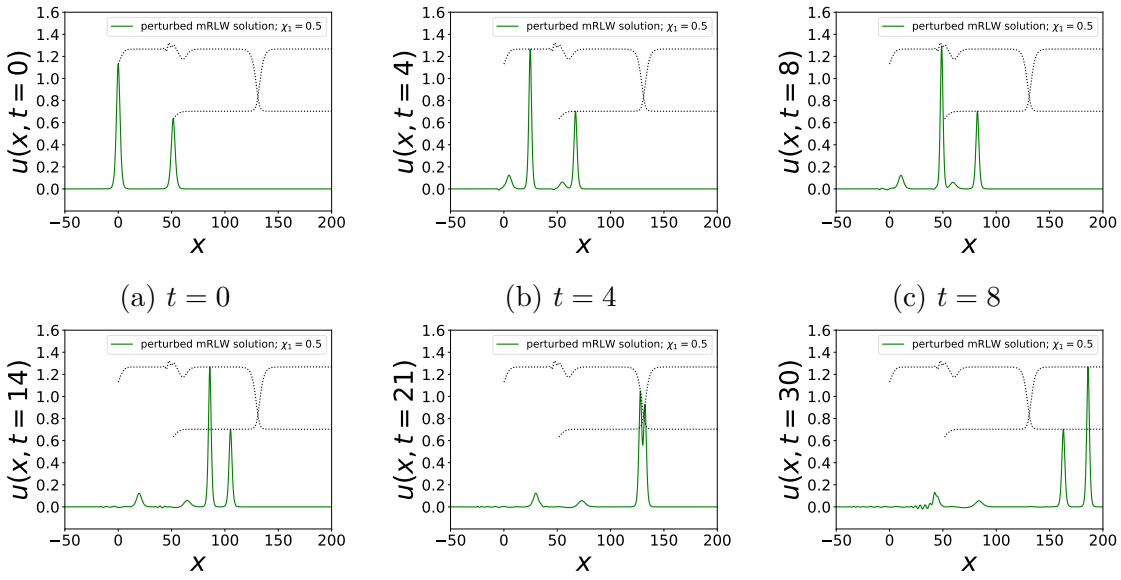

(a) $t = 0$ (b) $t = 4$ (c) $t = 8$

(d) $t = 14$ (e) $t = 21$ (f) $t = 30$

Figure 5.11: The time evolution of an mRLW two-soliton solution perturbed through $\chi_1 = 0.5$ and $\chi_2 = 0$.

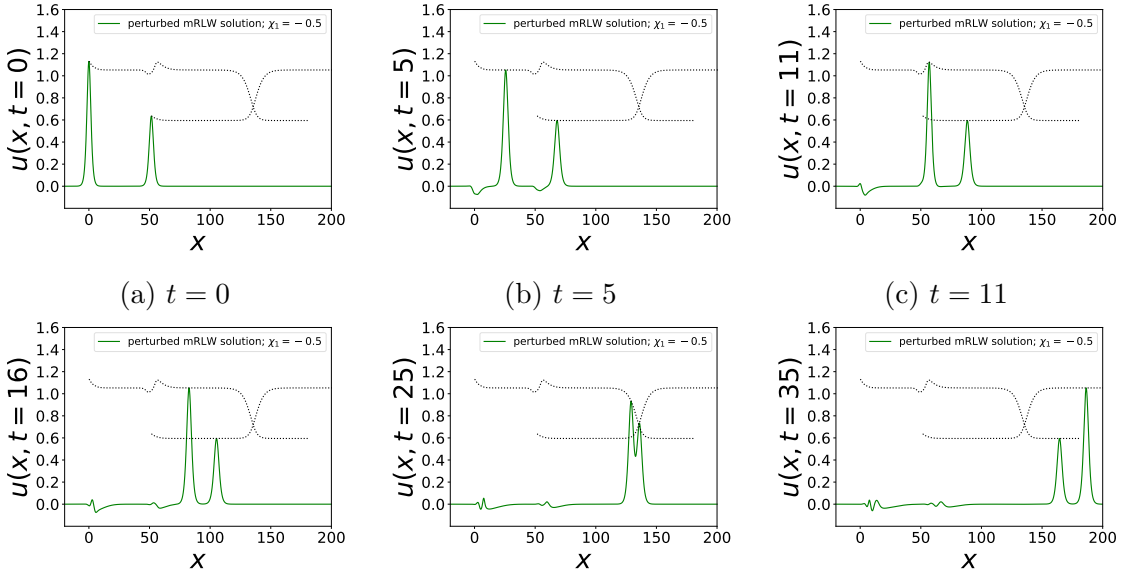

(a) $t = 0$ (b) $t = 5$ (c) $t = 11$

(d) $t = 16$ (e) $t = 25$ (f) $t = 35$

Figure 5.12: The time evolution of an mRLW two-soliton solution perturbed through $\chi_1 = -0.5$ and $\chi_2 = 0$.

5.1.3 Three-soliton solutions

In this subsection, we briefly present some numerical three-soliton simulations in the presence of perturbation terms, which allow us to investigate the 'many-particle' effects of perturbed three-soliton interactions. Furthermore, we discuss their quasi-integrability properties in chapter 6.

Since there are no known analytical three-soliton solutions that solve the mRLW equation, we use the superposition of three single-soliton solutions as initial conditions, that is,

$$q = \ln\left(1 + e^{\Gamma_1}\right) + \ln\left(1 + e^{\Gamma_2}\right) + \ln\left(1 + e^{\Gamma_3}\right) . \tag{5.1.5}$$

Figures 5.13 and 5.14 show two simulations constructed with these initial conditions; figure 5.13 is produced with $\chi_1 = 0$ and $\chi_2 = 0.5$, and figure 5.14 with $\chi_1 = 0$ and $\chi_2 = -0.5$. Similarly, figures 5.15 and 5.16 show the three-soliton simulations corresponding to $\chi_1 = 0.5$ and $\chi_1 = -0.5$, respectively, with $\chi_2 = 0$ for both simulations. The behaviour of these systems is very similar to the behaviour of the perturbed two-soliton simulations. We see that initially the two largest solitons emit visible radiation. (Note that we observed that the smallest soliton also emits

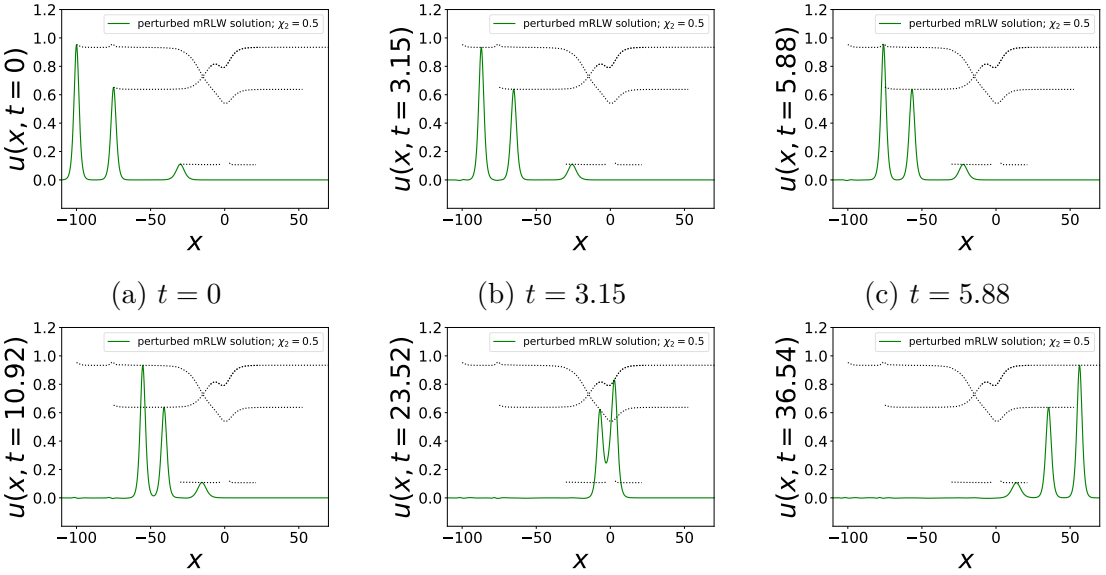

(a) $t = 0$ (b) $t = 3.15$ (c) $t = 5.88$

(d) $t = 10.92$ (e) $t = 23.52$ (f) $t = 36.54$

Figure 5.13: The time evolution of an mRLW three-soliton solution perturbed through $\chi_1 = 0$ and $\chi_2 = 0.5$.

radiation, however it is too small to see it in the figures.) As a result of the largest soliton colliding with the emitted radiation, its amplitude changes (see for example figures 5.13c, 5.14c, 5.15c and 5.16c). However, after this interaction, it returns to the same height as it had before the interaction. Subsequently, the three soliton-like

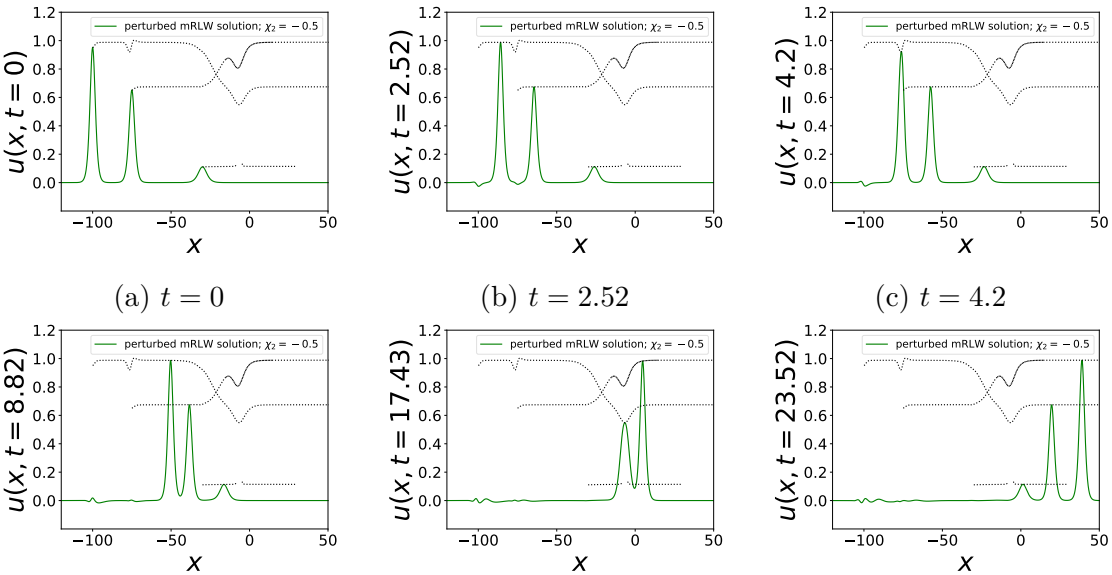

(a) $t = 0$ (b) $t = 2.52$ (c) $t = 4.2$

(d) $t = 8.82$ (e) $t = 17.43$ (f) $t = 23.52$

Figure 5.14: The time evolution of an mRLW three-soliton solution perturbed through $\chi_1 = 0$ and $\chi_2 = -0.5$.

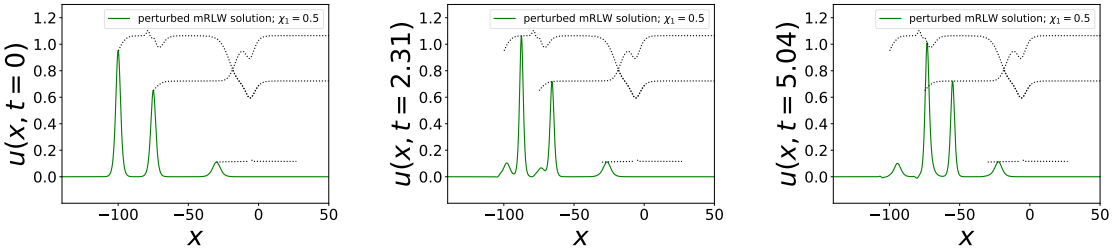

(a) $t = 0$ (b) $t = 2.31$ (c) $t = 5.04$

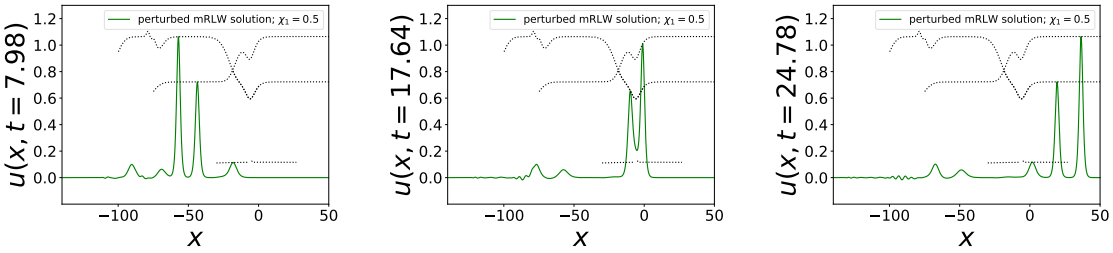

(d) $t = 7.98$ (e) $t = 17.64$ (f) $t = 24.78$

Figure 5.15: The time evolution of an mRLW three-soliton solution perturbed through $\chi_1 = 0.5$ and $\chi_2 = 0$.

structures simultaneously scatter with each other and, after the interaction, they again return to their original shapes.

Thus, to sum up, we see that the perturbed mRLW (multi-)soliton solutions give rise to long-lived localised structures, provided the perturbations are small enough.

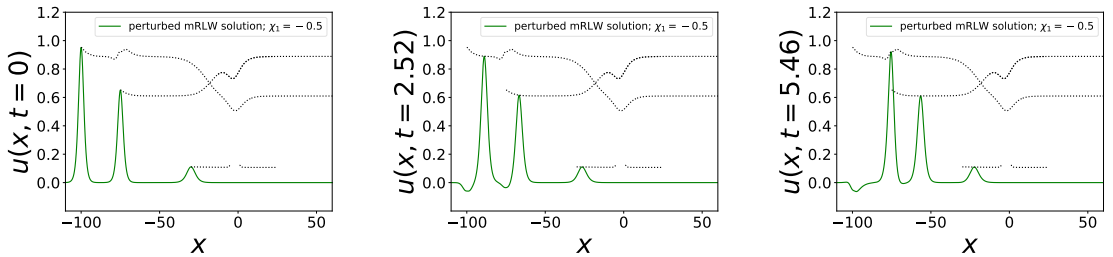

(a) $t = 0$ (b) $t = 2.52$ (c) $t = 5.46$

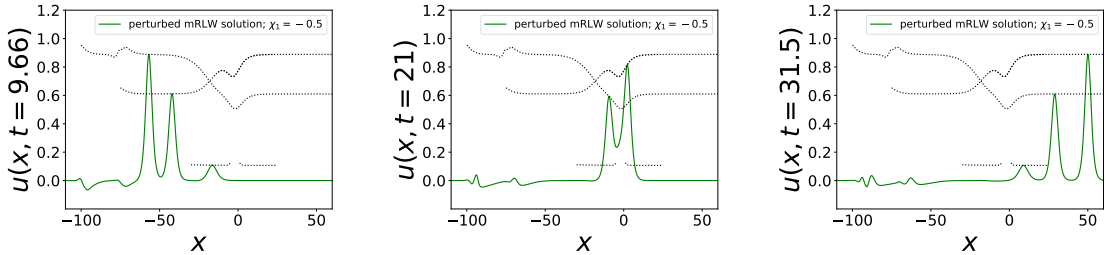

(d) $t = 9.66$ (e) $t = 21$ (f) $t = 31.5$

Figure 5.16: The time evolution of an mRLW three-soliton solution perturbed through $\chi_1 = -0.5$ and $\chi_2 = 0$.

These long-lived localised structures behave very much like solitons in the sense that interactions with other such structures appear to be (nearly) elastic. Furthermore, the interactions with radiation-like components also appears to result in (nearly) elastic scattering properties.

5.2 Perturbations of RLW solutions

In this section, we investigate the perturbed RLW soliton solutions. To this end, let us now rewrite equation (1.1.1) as

$$u_t + u_x + \left[\frac{\alpha}{2}u^2 - u_{xt}\right]_x = \left[-\varepsilon_2\frac{\alpha}{4}w_x v_t - \chi_1\left(u_{xx} - u_{xt}\right)\right]_x , \tag{5.2.1}$$

where χ_1 is defined by equation (5.1.2). The left-hand side is equivalent to the RLW partial differential operator. Thus, u can now be considered as a solution of the perturbed RLW equation, where the magnitudes of the perturbations are determined by χ_1 and ε_2.

5.2.1 One-soliton solutions

To study the perturbed RLW one-soliton solutions, we use equation (1.3.30) with $\varepsilon_2 = 0$ as initial conditions, that is,

$$q = \frac{3}{2}\ln\left(1 + e^{\Gamma_1}\right) . \tag{5.2.2}$$

The time evolution of these initial conditions governed by $\chi_1 = 0$ and $\varepsilon_2 = 0.5$ is shown in figures 5.17a to 5.17c, and figures 5.17d to 5.17f show the simulation perturbed through $\chi_1 = 0$ and $\varepsilon_2 = -0.5$. These simulations are similar to the results obtained from the perturbed mRLW one-soliton solutions. That is, we see that initially, the soliton emits some radiation while its amplitude changes slightly. Subsequently, the soliton-like structure propagates to the right unhindered, and appears to be long-lived.

In figure 5.18a we present the amplitude's trajectory for various values of $\varepsilon_2 \geq 0$,

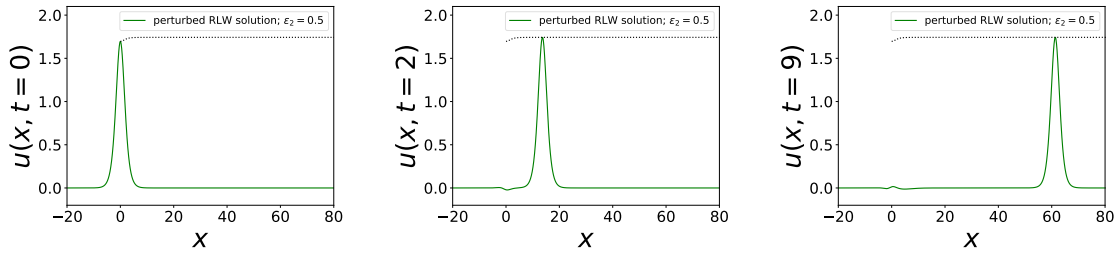

(a) $t = 0$ (b) $t = 2$ (c) $t = 9$

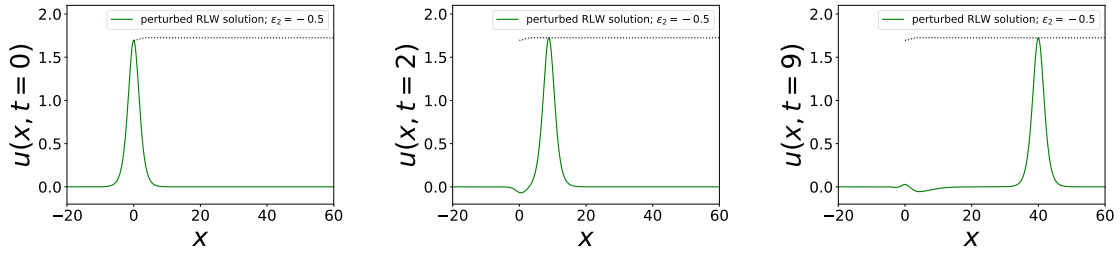

(d) $t = 0$ (e) $t = 2$ (f) $t = 9$

Figure 5.17: Figures (a) to (c) show the time evolution of an RLW one-soliton solution perturbed through $\chi_1 = 0$ and $\varepsilon_2 = 0.5$. Similarly, figures (d) to (f) show the simulation perturbed through $\chi_1 = 0$ and $\varepsilon_2 = -0.5$.

and figure 5.18b shows the trajectory for various values of $\varepsilon_2 \leq 0$. Figure 5.18a shows that as we increase ε_2, the amplitude of the soliton increases more rapidly. The results shown in figure 5.18b are more complicated; the amplitude of the soliton perturbed through $\varepsilon_2 = -0.1$ initially increases very slightly (see figure 5.18c: from $t = 0$ to $t \sim 2$), and then the soliton starts to decrease until the soliton stabilises with an amplitude that is in fact smaller than the initial soliton's amplitude. For the simulation corresponding to $\varepsilon_2 = -0.2$ we see the same pattern (i.e., the amplitude increases initially (until $t \sim 3$) and then decreases again until it stabilises), but

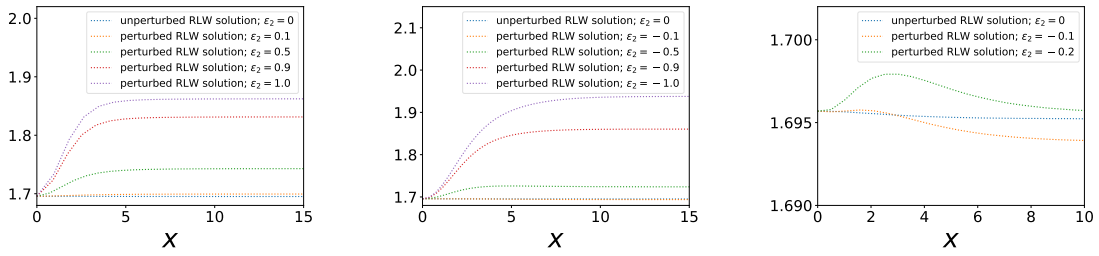

(a) (b) (c)

Figure 5.18: The trajectories of an RLW soliton's amplitude perturbed through various values of ε_2 while keeping $\chi_1 = 0$ constant. Figure (c) shows the same first three plotted curves as shown in figure (b) but at a much smaller scale.

the amplitude now stabilises at a slightly larger value than its initial value (see figure 5.18c). When we decrease $\varepsilon_2 < -0.2$ even further, we see from figure 5.18b that the soliton stabilises at an increasingly larger amplitude. However, for $\varepsilon_2 = -1$, we found that the simulation in fact blows up at approximately $t \approx 4.4$.

We have also investigated the perturbations through χ_1 while keeping $\varepsilon_2 = 0$. Figure 5.19 shows two of such simulations; figures 5.19a to 5.19c show the time evolution perturbed through $\chi_1 = 0.5$, and figures 5.19d to 5.19f through $\chi_1 = -0.5$. We again see that the initial soliton emits radiation while its amplitude changes in magnitude. Furthermore, figure 5.20 shows how the amplitude of the initial soliton changes under various perturbations through χ_1. This shows that for $\chi_1 > 0$, the amplitude increases, and for $\chi_1 < 0$ the amplitude decreases. This behaviour is less complex than for perturbations through ε_2.

5.2.2 Two-soliton solutions

In this subsection, we briefly discuss the RLW two-soliton solutions in the presence of perturbations. Since this model does not admit any exact multi-soliton solutions,

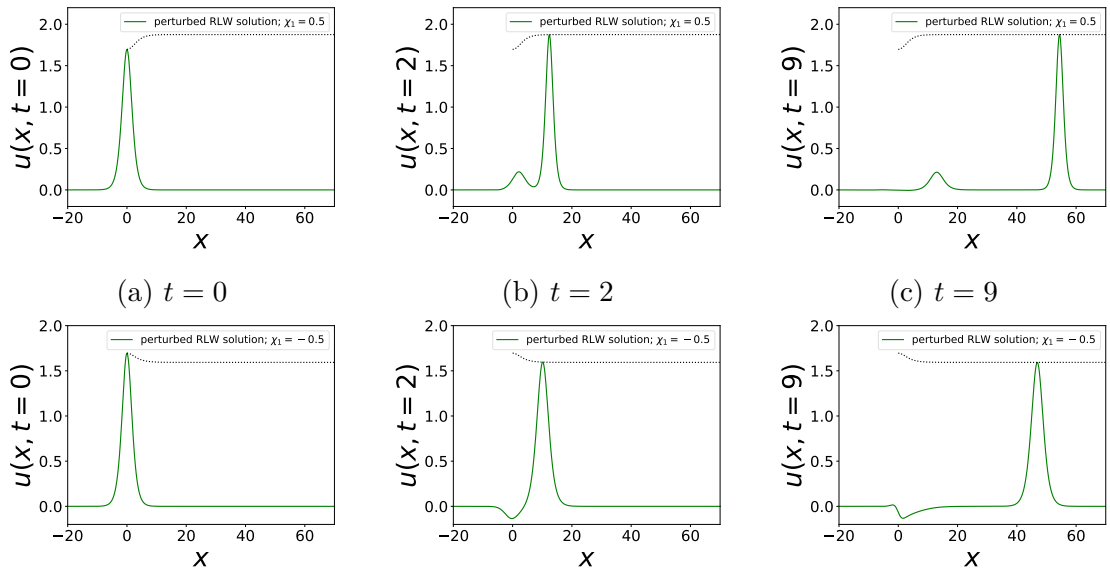

(a) $t = 0$ (b) $t = 2$ (c) $t = 9$

(d) $t = 0$ (e) $t = 2$ (f) $t = 9$

Figure 5.19: Figures (a) to (c) show the time evolution of an RLW one-soliton solution perturbed through $\chi_1 = 0.5$ and $\varepsilon_2 = 0$. Similarly, figures (d) to (f) show the simulation perturbed through $\chi_1 = -0.5$ and $\varepsilon_2 = 0$.

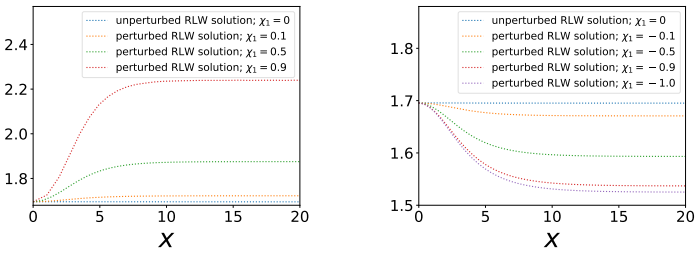

(a) (b)

Figure 5.20: The trajectories of an RLW soliton's amplitude perturbed through various values of χ_1 while keeping $\varepsilon_2 = 0$ constant.

we use the following initial conditions

$$q = \frac{3}{2}\ln\left(1 + e^{\Gamma_1}\right) + \frac{3}{2}\ln\left(1 + e^{\Gamma_2}\right) . \tag{5.2.3}$$

Figures 5.21 and 5.22 show the time evolution of such initial conditions under the perturbations governed by $\varepsilon_2 = 0.5$ and $\varepsilon_2 = -0.5$, respectively, and $\chi_1 = 0$ for both simulations. We see that, provided the perturbation is sufficiently small, the perturbed RLW two-soliton solutions have many of the same features as the perturbed mRLW soliton solutions discussed in the previous section. When the largest soliton-like structure interacts with the radiation emitted by the smallest

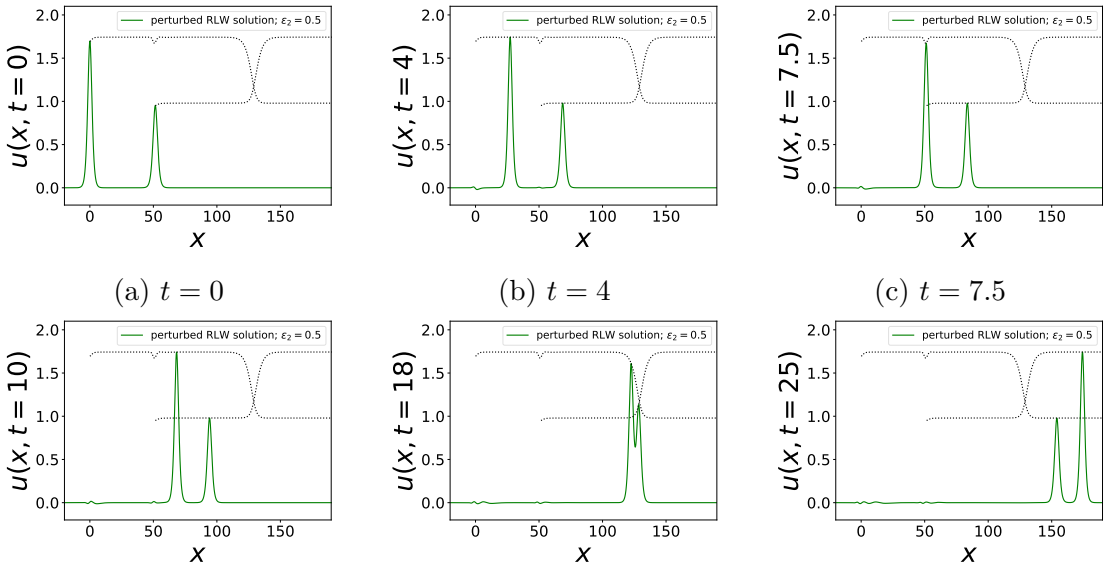

(a) $t = 0$ (b) $t = 4$ (c) $t = 7.5$

(d) $t = 10$ (e) $t = 18$ (f) $t = 25$

Figure 5.21: The time evolution of an RLW two-soliton solution perturbed through $\chi_1 = 0$ and $\varepsilon_2 = 0.5$.

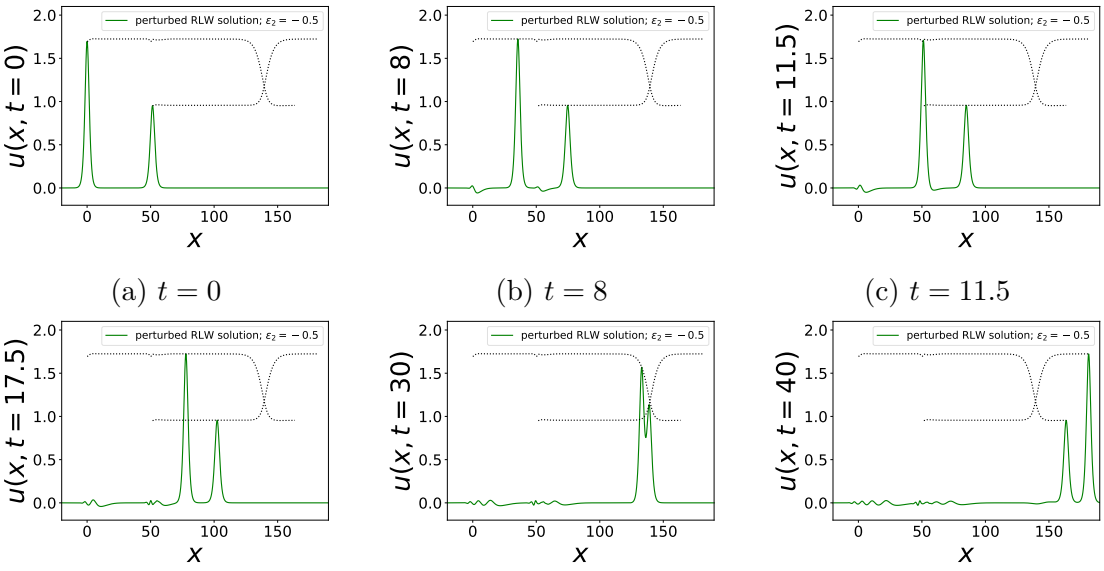

(a) $t = 0$ (b) $t = 8$ (c) $t = 11.5$

(d) $t = 17.5$ (e) $t = 30$ (f) $t = 40$

Figure 5.22: The time evolution of an RLW two-soliton solution perturbed through $\chi_1 = 0$ and $\varepsilon_2 = -0.5$.

initial soliton, as shown in figures 5.21c and 5.22c, the amplitude of the soliton changes briefly. However, after the interaction, the amplitude returns to the same height it was at before the interaction. Furthermore, when the two soliton-like structures interact with each other (see figures 5.21e and 5.22e), the solution's amplitude decreases, which is what we expect from soliton interactions.

The RLW two-soliton configuration in the presence of perturbations through χ_1 behaves in a very similar manner. This is shown in figures 5.23 and 5.24 for $\chi_1 = 0.5$ and $\chi_1 = -0.5$, respectively, with $\varepsilon_2 = 0$ for both simulations. The two initial solitons, shown in figures 5.23a and 5.24a, emit some radiation at the beginning of the simulation. As a consequence, the solitons' amplitudes change in magnitude, and then stabilise again after the resulting soliton-like structures have moved sufficiently far from the emitted radiation, as shown in figures 5.23b and 5.24b. When the largest soliton-like structure collides with the radiation emitted by the smallest initial soliton, see figures 5.23c and 5.24c, its amplitude changes slightly. However, it returns to its original height after the soliton-like structure has moved passed the radiation-like component, as shown in figures 5.23d and 5.24d. Next, the two solitons interact with each other in a nonlinear manner, as shown in figures 5.23e and 5.24e. Finally,

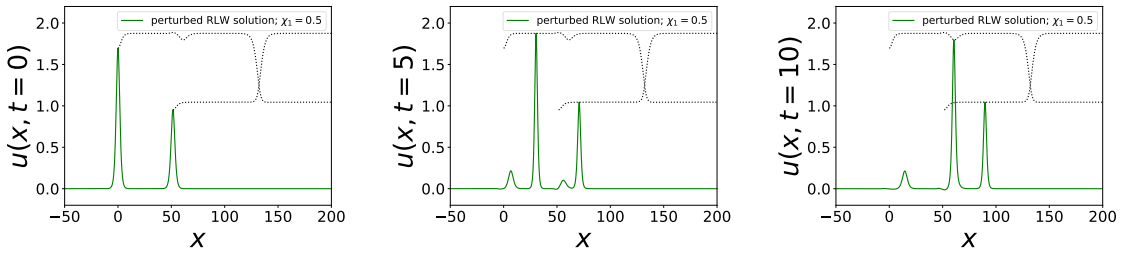

(a) $t = 0$ (b) $t = 5$ (c) $t = 10$

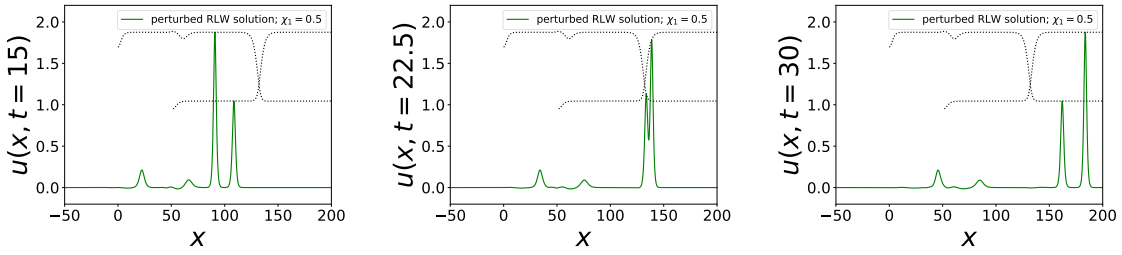

(d) $t = 15$ (e) $t = 22.5$ (f) $t = 30$

Figure 5.23: The time evolution of an RLW two-soliton solution perturbed through $\chi_1 = 0.5$ and $\varepsilon_2 = 0$.

figures 5.23f and 5.24f show that they continue to propagate to the right unhindered. Thus, to sum up, the initial two-soliton systems result in two long-lived soliton-like structures, with additional radiation-like components.

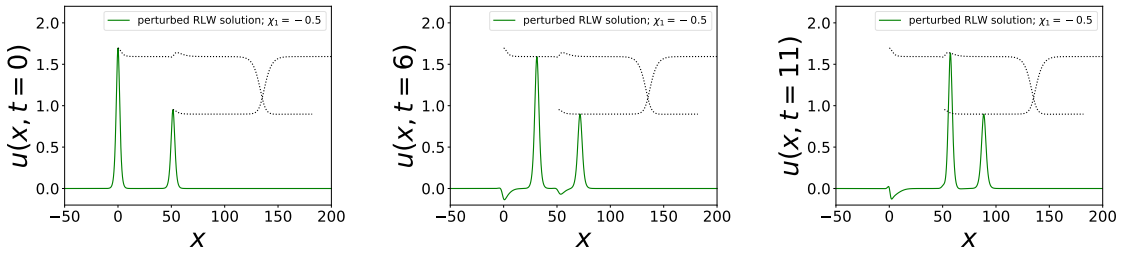

(a) $t = 0$ (b) $t = 6$ (c) $t = 11$

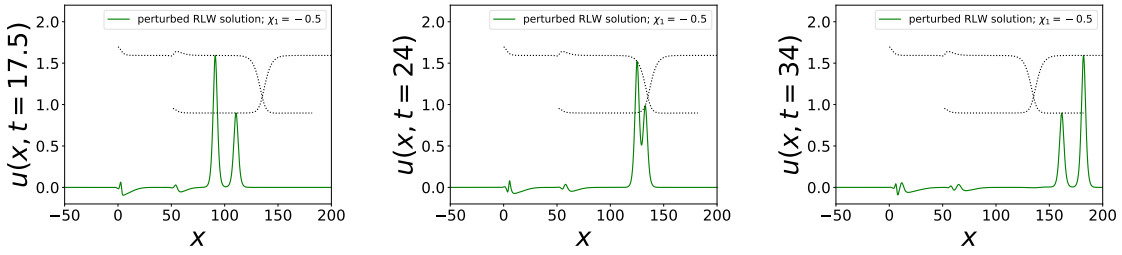

(d) $t = 17.5$ (e) $t = 24$ (f) $t = 34$

Figure 5.24: The time evolution of an RLW two-soliton solution perturbed through $\chi_1 = -0.5$ and $\varepsilon_2 = 0$.

5.2.3 Three-soliton solutions

Finally, in this subsection, we present the numerical time evolution of the RLW three-soliton solutions in the presence of the perturbing terms. In other words, we use the following initial conditions

$$q = \frac{3}{2}\ln\left(1+e^{\Gamma_1}\right) + \frac{3}{2}\ln\left(1+e^{\Gamma_2}\right) + \frac{3}{2}\ln\left(1+e^{\Gamma_3}\right), \tag{5.2.4}$$

and investigate how these systems evolve for non-zero values of χ_1 or ε_2. The simulations corresponding to $\varepsilon_2 = 0.5$ and $\varepsilon_2 = -0.5$, with $\chi_1 = 0$ for both simulations, are shown in figures 5.25 and 5.26, respectively. Furthermore, figures 5.27 and 5.28, show the simulations for $\chi_1 = 0.5$ and $\chi_1 = -0.5$, respectively, with $\varepsilon_2 = 0$ for both simulations. These perturbed three-soliton configurations behave as we expect. Immediately after the start of the simulation, the two largest solitons emit visible radiation while their amplitudes change significantly. Subsequently, the largest soliton interacts with the radiation emitted by the second-largest soliton. Due to the interaction between the soliton-like structure and the radiation-like structure, the amplitude of the soliton field changes slightly, but then returns to the same height it

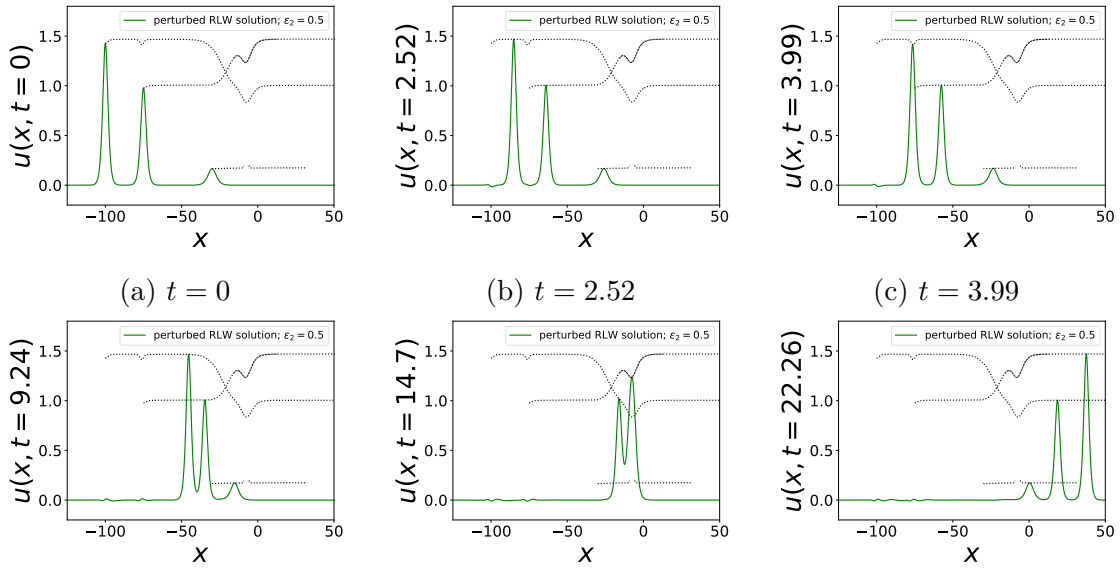

(a) $t = 0$ (b) $t = 2.52$ (c) $t = 3.99$

(d) $t = 9.24$ (e) $t = 14.7$ (f) $t = 22.26$

Figure 5.25: The time evolution of an RLW three-soliton solution perturbed through $\chi_1 = 0$ and $\varepsilon_2 = 0.5$.

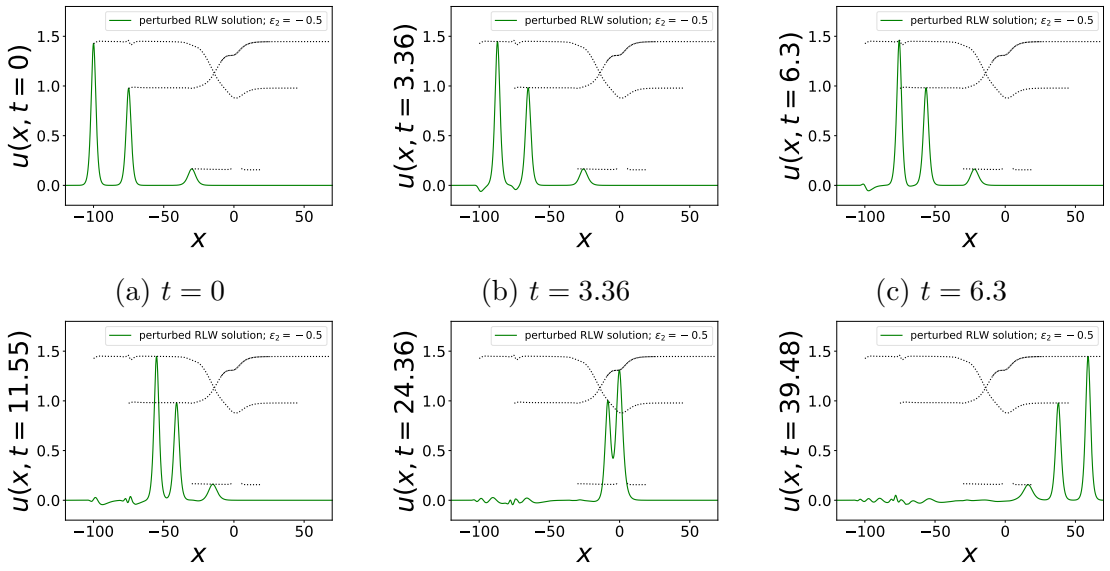

(a) $t = 0$ (b) $t = 3.36$ (c) $t = 6.3$

(d) $t = 11.55$ (e) $t = 24.36$ (f) $t = 39.48$

Figure 5.26: The time evolution of an RLW three-soliton solution perturbed through $\chi_1 = 0$ and $\varepsilon_2 = -0.5$.

had before the interaction. Eventually, the three soliton-like fields interact with each other in a three-body collision. The solution's amplitude during this collision always decreases, and so this interaction is due to nonlinear effects. After the multi-soliton collision, the three solitons propagate to the right unhindered, i.e., they appear to

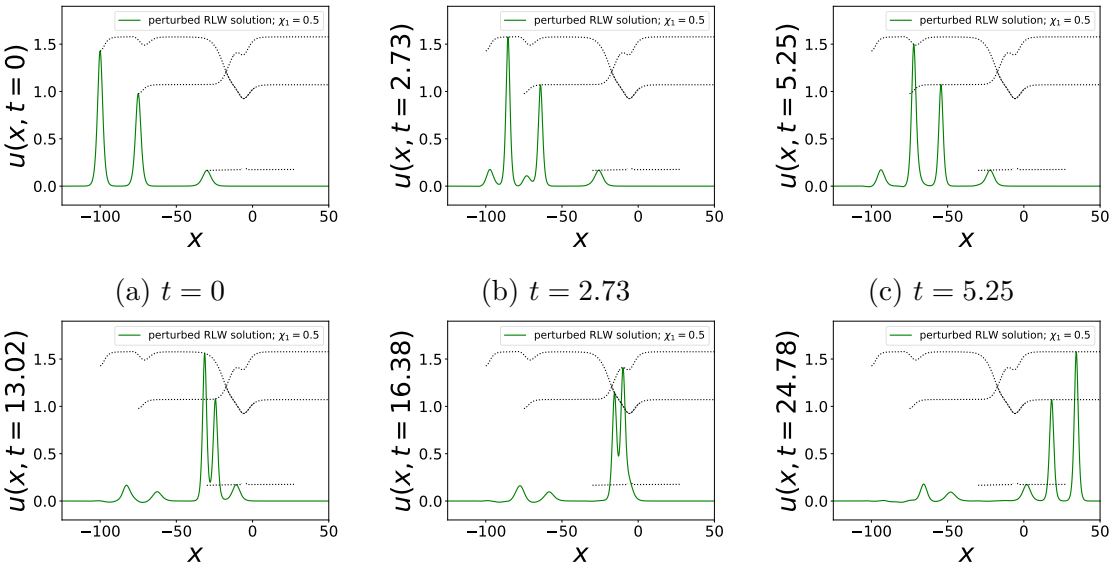

(a) $t = 0$ (b) $t = 2.73$ (c) $t = 5.25$

(d) $t = 13.02$ (e) $t = 16.38$ (f) $t = 24.78$

Figure 5.27: The time evolution of an RLW three-soliton solution perturbed through $\chi_1 = 0.5$ and $\varepsilon_2 = 0$.

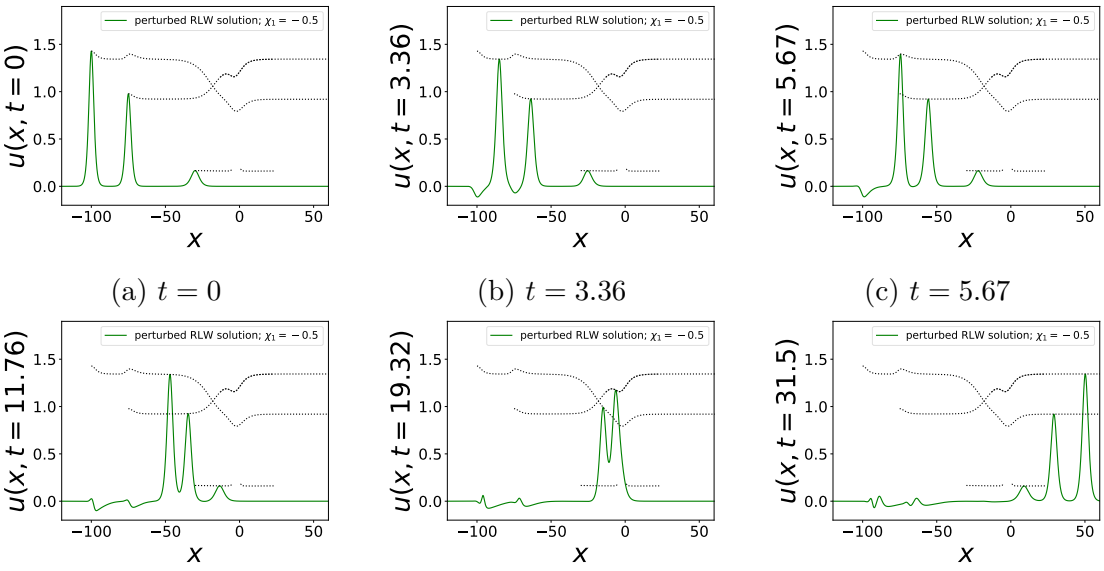

(a) $t = 0$ (b) $t = 3.36$ (c) $t = 5.67$

(d) $t = 11.76$ (e) $t = 19.32$ (f) $t = 31.5$

Figure 5.28: The time evolution of an RLW three-soliton solution perturbed through $\chi_1 = -0.5$ and $\varepsilon_2 = 0$.

be long-lived soliton-like structures.

Chapter 6

Numerical investigations of quasi-integrability

In this chapter, we investigate the quasi-integrability properties of the simulations presented in the previous two chapters. In particular, we have determined the corresponding first three non-trivial $Q^{(-2n-1)}$'s, i.e., $Q^{(-3)}$, $Q^{(-5)}$ and $Q^{(-7)}$, as discussed in subsection 2.2.1. To this end, we first use equation (2.2.33) to determine $\partial_t Q^{(-2n-1)}$. All the simulations we discuss in this chapter start at $t = 0$, and so we integrate $\partial_t Q^{(-2n-1)}$ to find

$$\int_0^t \mathrm{d}t' \, \frac{Q^{(-2n-1)}}{dt'} = Q^{(-2n-1)}(t) - Q^{(-2n-1)}(0)\,. \tag{6.0.1}$$

We only focus on the first non-trivial charge $Q^{(-3)}$. We found that the behaviour of the next charges $Q^{(-5)}$ and $Q^{(-7)}$ are very similar to $Q^{(-3)}$. However, to calculate $Q^{(-5)}$ and $Q^{(-7)}$, we need to calculate terms with higher-order derivatives. As a result, their charge densities (i.e., $X\gamma^{(-5)}$ and $X\gamma^{(-7)}$) suffer from significant numerical errors. Since these errors are random, they essentially cancel each other out when the densities are integrated to calculate $Q^{(-5)}$ and $Q^{(-7)}$. However, they are less reliable, and so we do not discuss them in detail.

Thus, we use $\int_0^t \mathrm{d}t' \, \partial_{t'} Q^{(-3)}$ and $\partial_t Q^{(-3)}$ to investigate the quasi-integrability of the simulations presented in the previous two chapters. In particular, in the first

two sections of this chapter, we investigate the quasi-integrability properties of the multi-soliton mRLW and RLW simulations, as previously discussed in chapter 4.[1] In sections 6.3 and 6.4, we discuss the quasi-integrability properties of the perturbed mRLW and RLW solutions that were presented in chapter 5.

6.1 mRLW solutions

As mentioned above, in this section we investigate the quasi-integrability properties of the multi-soliton simulations presented in section 4.1. First, however, we focus on the two-soliton simulation shown in figure 3.4; figure 6.1 shows how the values of $\int_0^t \mathrm{d}t' \, \partial_{t'} Q^{(-3)}$ and $\partial_t Q^{(-3)}$ vary with respect to time, where the red curves in figure 6.1 represent the values due to the simulation shown by the red curves in figure 3.4 (i.e., the analytical mRLW two-soliton solution), and the green curves in figure 6.1 are due to the simulation shown by the green curves in figure 3.4 (i.e., the numerical mRLW two-soliton simulation). Comparing figure 6.1a with figure 3.4, we see that initially, before the solitons start to interact with each other, the quantity $\int_0^t \mathrm{d}t' \, \partial_{t'} Q^{(-3)}$ is approximately equal to zero. However, as the solitons

[1] We do not discuss the single-soliton simulations for these models, because we know that they will be truly conserved (see subsection 2.3.1).

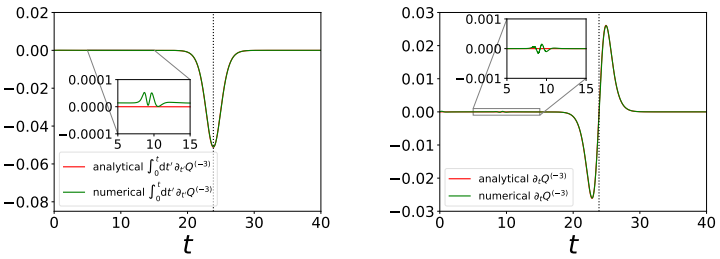

(a) (b)

Figure 6.1: The red curves in figures (a) and (b) show the time-dependence of the quantities $\int_0^t \mathrm{d}t' \, \partial_{t'} Q^{(-3)}$ and $\partial_t Q^{(-3)}$ for the analytical mRLW two-soliton solution presented by the red curves in figure 3.4. Similarly, the green curves in figures (a) and (b) display the time-dependence of $\int_0^t \mathrm{d}t' \, \partial_{t'} Q^{(-3)}$ and $\partial_t Q^{(-3)}$ for the corresponding numerical mRLW two-soliton simulation presented by the green curves in figure 3.4. Finally, the dotted vertical lines in both figures is $t = t_\Delta$, as defined by equation (2.4.6).

start to interact with each other (i.e., at $t \sim 20$, as shown in figure 3.4c), the value of $\int_0^t \mathrm{d}t' \, \partial_{t'} Q^{(-3)}$ starts to decrease until $t = t_\Delta$ (see equation (2.4.6)), which is illustrated by the dotted vertical lines in figure 6.1. Subsequently, the solitons start to move away from each other, and $\int_0^t \mathrm{d}t' \, \partial_{t'} Q^{(-3)}$ starts to increase again until it approximately equals zero. Then, as the solitons continue to move unhindered, the value stays (approximately) constant, and so we see that equation (1.4.2) is satisfied. Thus, we can conclude that $Q^{(-3)}$ is indeed quasi-conserved and, as mentioned in the introduction of this chapter, we found similar properties for $Q^{(-5)}$ and $Q^{(-7)}$. This is not surprising, since we have proved this analytically in section 2.4.

Looking at figure 6.1, we see that the analytical and numerical results are very close together. However, note that from $t \sim 7$ to $t \sim 12$ we see a small disturbance in the numerical results. To illustrate this effect, we have added insets in figure 6.1 that show this region at a much smaller scale. After a careful analysis of the simulations shown in figure 3.4 at a much smaller scale, we found that the numerical solitons initially do emit a tiny amount of radiation. Subsequently, the largest soliton scatters with the radiation emitted by the smallest soliton (in a similar manner as we have observed in chapter 5). The amplitude of the soliton changes slightly during this interaction, which causes the small disturbance displayed by the insets in figure 6.1.

Next, we focus on the quasi-integrability properties of the three-soliton mRLW simulations discussed in subsection 4.1.2. The time-dependence of $\int_0^t \mathrm{d}t' \, \partial_{t'} Q^{(-3)}$ and $\partial_t Q^{(-3)}$ related to figure 4.3 are shown in figure 6.2. We again see that the value

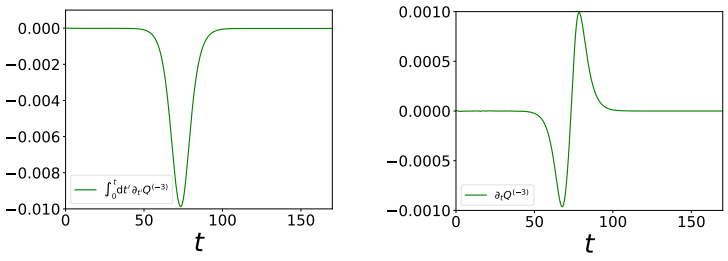

(a) (b)

Figure 6.2: The green curves in figures (a) and (b) show the time-dependence of the quantities $\int_0^t \mathrm{d}t' \, \partial_{t'} Q^{(-3)}$ and $\partial_t Q^{(-3)}$ for the numerical mRLW three-soliton solution presented by the green curves in figure 4.3.

of $\int_0^t \mathrm{d}t' \, \partial_{t'} Q^{(-3)}$ initially is (approximately) equal to zero, and its value decreases as the solitons get closer to each other. At $t \sim 73.5$, the value of $\int_0^t \mathrm{d}t' \, \partial_{t'} Q^{(-3)}$ starts to increase again until it approximates zero, which is when the three solitons have moved away from each other after the interaction. Thus, we can conclude that the charges $Q^{(-2n-1)}$ are also quasi-conserved for this three-soliton simulation.

Similarly, figure 6.3 shows the time-dependence of $\int_0^t \mathrm{d}t' \, \partial_{t'} Q^{(-3)}$ and $\partial_t Q^{(-3)}$ for the simulation corresponding to figure 4.5. We see that the charges $Q^{(-2n-1)}$ for this three-soliton simulation are also quasi-conserved. Just as with the other simulations, the quantity $\int_0^t \mathrm{d}t' \, \partial_{t'} Q^{(-3)}$, which is initially approximately equal to zero, decreases when the three-solitons start to interact with each other. Subsequently, when the solitons start to move away from each other, its value increases again until it approaches zero.

By comparing figure 4.4a with figure 4.6a, we see that the three-soliton interaction shown in figure 4.5 is 'less symmetric' in the sense that the largest two solitons start interacting with each other (and as a result, their shapes and velocities also change) before they scatter with the smallest soliton. Furthermore, when the solitons cease to interact, the largest soliton regains its original shape and velocity while the other two solitons are still interacting with each other. On the other hand, the solitons shown in figure 4.3 start to interact with each other approximately at the same time; and after the interaction they regain their original shape and velocity approximately at the same time. As a result, figure 6.3 shows 'less symmetric' curves than figure 6.2.

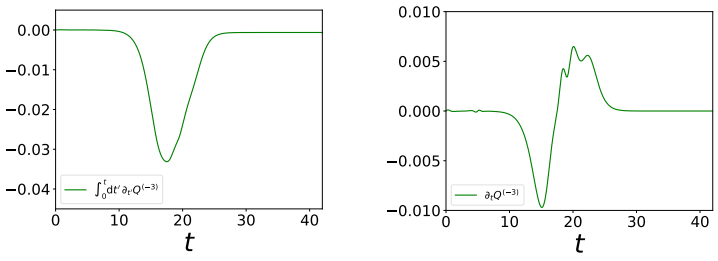

(a) (b)

Figure 6.3: The green curves in figures (a) and (b) show the time-dependence of the quantities $\int_0^t \mathrm{d}t' \, \partial_{t'} Q^{(-3)}$ and $\partial_t Q^{(-3)}$ for the numerical mRLW three-soliton solution presented by the green curves in figure 4.5.

To sum up, these results have shown that the first three non-trivial charges $Q^{(-2n-1)}$ appear to be quasi-conserved for the numerical three-soliton solutions governed by the mRLW equation. Furthermore, as discussed in section 2.4, we have analytically shown that for the exact mRLW two-soliton solutions they are quasi-conserved. We have not investigated any N-soliton interactions for $N > 3$. However, from these observations, we conjecture that the charges are quasi-conserved for any N-soliton mRLW solution, where $N > 1$.

6.2 RLW solutions

In this section, we investigate the quasi-integrability properties of the RLW simulations presented in section 4.2. First, we focus on the simulation shown in figure 4.7; figure 6.4 shows the quantities $\int_0^t \mathrm{d}t'\, \partial_{t'} Q^{(-3)}$ and $\partial_t Q^{(-3)}$ for this simulation. Just as for the mRLW solutions, the quantity $\int_0^t \mathrm{d}t'\, \partial_{t'} Q^{(-3)}$ changes only during the scattering of the two solitons. Furthermore, the value of $\int_0^t \mathrm{d}t'\, \partial_{t'} Q^{(-3)}$ before and after the interaction is approximately the same, and so equation (1.4.2) is satisfied. Thus, the charges $Q^{(-2n-1)}$ for the RLW two-soliton configurations appear to be quasi-conserved as well.

Next, we look at the quasi-integrability properties of the three-soliton RLW simulations shown in figures 4.10 and 4.11. The time-dependence of $\int_0^t \mathrm{d}t'\, \partial_{t'} Q^{(-3)}$ and $\partial_t Q^{(-3)}$ for the three-soliton systems are shown in figures 6.5 and 6.6, respectively.

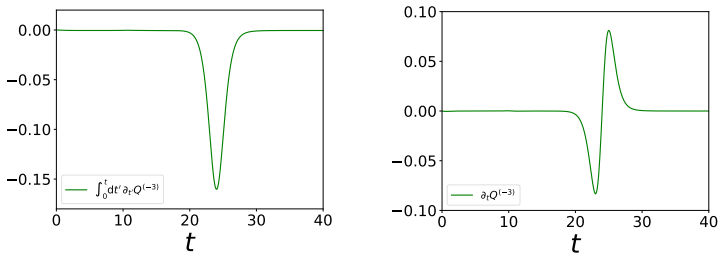

(a) (b)

Figure 6.4: The green curves in figures (a) and (b) show the time-dependence of the quantities $\int_0^t \mathrm{d}t'\, \partial_{t'} Q^{(-3)}$ and $\partial_t Q^{(-3)}$ for the numerical RLW two-soliton solution presented by the green curves in figure 4.7.

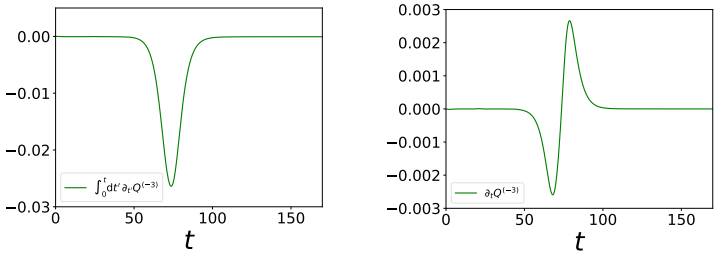

(a) (b)

Figure 6.5: The green curves in figures (a) and (b) show the time-dependence of the quantities $\int_0^t \mathrm{d}t'\, \partial_{t'} Q^{(-3)}$ and $\partial_t Q^{(-3)}$ for the numerical RLW three-soliton solution presented by the green curves in figure 4.10.

We again see that the value of $\int_0^t \mathrm{d}t'\, \partial_{t'} Q^{(-3)}$ only changes during the three-soliton interactions, and after the collision its value returns to the same initial value. In other words, the first three non-trivial charges $Q^{(-2n-1)}$ appear to also be quasi-conserved for the three-soliton solutions governed by the RLW equation. This strongly indicates that the charges are quasi-conserved for any N-soliton solution, provided $N > 1$. Thus, the RLW solutions display the same quasi-integrability properties as the mRLW solutions that we discussed in the previous section.

6.3 Perturbed mRLW solutions

In this section, we discuss the quasi-integrability properties of the perturbed mRLW simulations presented in section 5.1. To be specific, in subsection 6.3.1 we discuss the perturbed one-soliton simulations presented in subsection 5.1.1. Subsequently, in

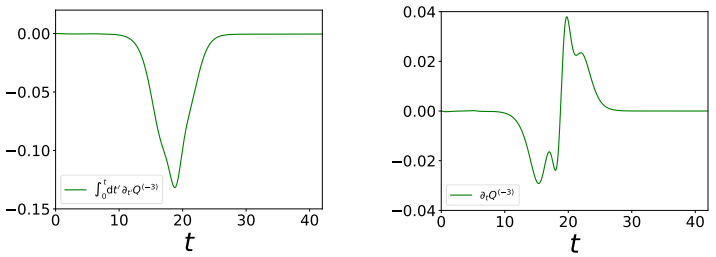

(a) (b)

Figure 6.6: The green curves in figures (a) and (b) show the time-dependence of the quantities $\int_0^t \mathrm{d}t'\, \partial_{t'} Q^{(-3)}$ and $\partial_t Q^{(-3)}$ for the numerical RLW three-soliton solution presented by the green curves in figure 4.11.

the next two subsections, we discuss the two- and three-soliton simulations presented in subsections 5.1.2 and 5.1.3, respectively.

6.3.1 One-soliton solutions

To this end, figure 6.7 shows the time-dependence of $\int_0^t \mathrm{d}t'\, \partial_{t'} Q^{(-3)}$ and $\partial_t Q^{(-3)}$ related to the simulation perturbed through $\chi_2 = 0.5$, as shown in figure 5.3. We see that $\int_0^t \mathrm{d}t'\, \partial_{t'} Q^{(-3)}$ initially increases until it stabilises at $t \sim 2$. Thus, comparing this with figure 5.3, we see that $\int_0^t \mathrm{d}t'\, \partial_{t'} Q^{(-3)}$ stabilises after the initial soliton configuration has emitted its radiation component, and the resulting soliton-like structure has moved away sufficiently far from the radiation.

Figure 6.8 shows the time-dependence of $\int_0^t \mathrm{d}t'\, \partial_{t'} Q^{(-3)}$ and $\partial_t Q^{(-3)}$ for the one-soliton simulation perturbed through $\chi_2 = -0.5$, as shown in figure 5.5. We now see that $\int_0^t \mathrm{d}t'\, \partial_{t'} Q^{(-3)}$ initially decreases until it stabilises around $t \sim 1$. Looking at figure 5.5, we see that this happens when the soliton-like structure and the radiation have stopped interacting with each other.

For the perturbed one-soliton solutions through $\chi_1 = 0.5$, as shown in figures 5.7a to 5.7c, we have displayed the time-dependence of $\int_0^t \mathrm{d}t'\, \partial_{t'} Q^{(-3)}$ and $\partial_t Q^{(-3)}$ in figure 6.9. Just as for the perturbations through χ_2, the quantity $\int_0^t \mathrm{d}t'\, \partial_{t'} Q^{(-3)}$ changes rapidly when the initial soliton splits up in a soliton- and radiation-like component. However, figure 6.9c shows that the value of $\int_0^t \mathrm{d}t'\, \partial_{t'} Q^{(-3)}$ does not stabilise when the two components have moved away from each other. Instead, even

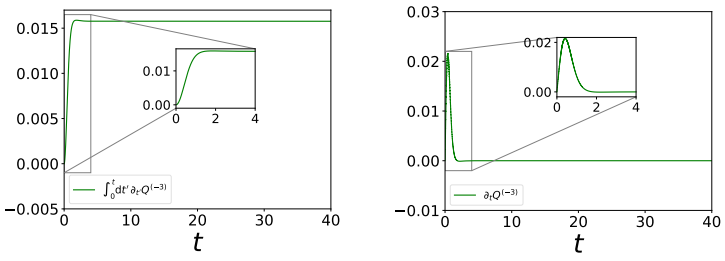

(a) (b)

Figure 6.7: The green curves in figures (a) and (b) show the time-dependence of the quantities $\int_0^t \mathrm{d}t'\, \partial_{t'} Q^{(-3)}$ and $\partial_t Q^{(-3)}$ for the numerical mRLW one-soliton solution perturbed through $\chi_1 = 0$ and $\chi_2 = 0.5$, as presented by the green curves in figure 5.3.

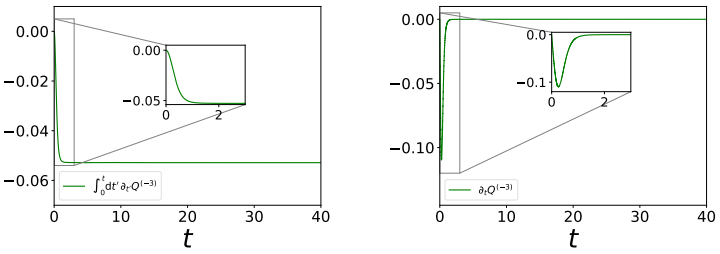

(a) (b)

Figure 6.8: The green curves in figures (a) and (b) show the time-dependence of the quantities $\int_0^t \mathrm{d}t'\, \partial_{t'} Q^{(-3)}$ and $\partial_t Q^{(-3)}$ for the numerical mRLW one-soliton solution perturbed through $\chi_1 = 0$ and $\chi_2 = -0.5$, as presented by the green curves in figure 5.5.

when the structures are far away from each other, its value decreases slowly.

Figure 6.10 shows the time-dependence of $\int_0^t \mathrm{d}t'\, \partial_{t'} Q^{(-3)}$ and $\partial_t Q^{(-3)}$ for the perturbation through $\chi_1 = -0.5$, as shown in figures 5.7d to 5.7f. In this instance, we see that the quantity $\int_0^t \mathrm{d}t'\, \partial_{t'} Q^{(-3)}$ initially decreases rapidly, but then it continues to steadily increase when the soliton-like and radiation-like structure have moved away from each other.

Thus, for perturbations through either χ_1 or χ_2, we see that the value of $\int_0^t \mathrm{d}t'\, \partial_{t'} Q^{(-3)}$ changes rapidly at the beginning of the simulation (i.e., when the soliton- and radiation-like components separate from each other). The main difference between these perturbations is that for χ_2, the value of $\int_0^t \mathrm{d}t'\, \partial_{t'} Q^{(-3)}$ approaches some constant value after the soliton-like structure has ceased interacting with the

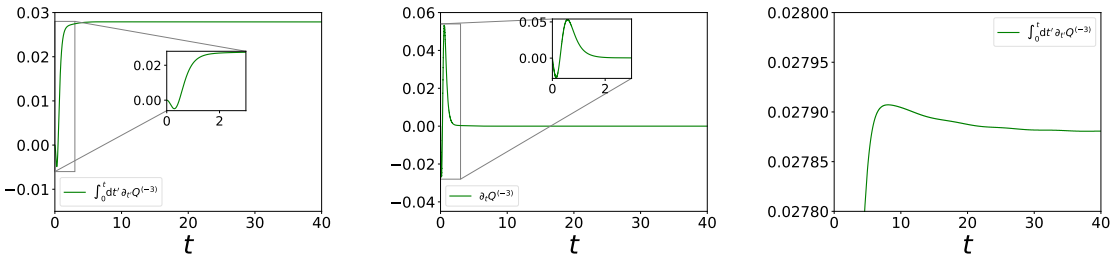

(a) $t = 0$ (b) $t = 2$ (c) $t = 9$

Figure 6.9: The green curves in figures (a) and (b) show the time-dependence of the quantities $\int_0^t \mathrm{d}t'\, \partial_{t'} Q^{(-3)}$ and $\partial_t Q^{(-3)}$ for the numerical mRLW one-soliton solution perturbed through $\chi_1 = 0.5$ and $\chi_2 = 0$, as presented by the green curves in figures 5.7a to 5.7c. Figure (c) shows the same plot as figure (a), but on a much smaller scale.

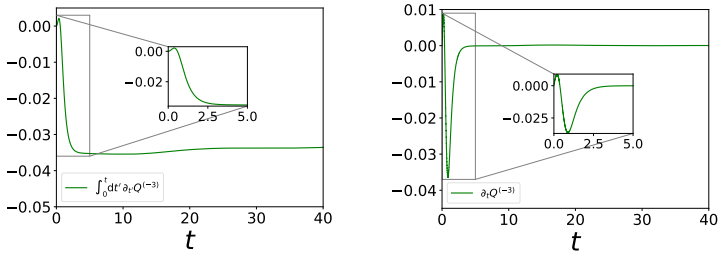

(a) (b)

Figure 6.10: The green curves in figures (a) and (b) show the time-dependence of the quantities $\int_0^t \mathrm{d}t'\, \partial_{t'} Q^{(-3)}$ and $\partial_t Q^{(-3)}$ for the numerical mRLW one-soliton solution perturbed through $\chi_1 = -0.5$ and $\chi_2 = 0$, as presented by the green curves in figures 5.7d to 5.7f.

radiation-like component. On the other hand, for perturbations through χ_1, we see that the value of $\int_0^t \mathrm{d}t'\, \partial_{t'} Q^{(-3)}$ slowly increases or decreases after the components have stopped interacting. In the next two subsections, we will further investigate this by looking at the perturbed mRLW two- and three-soliton simulations.

6.3.2 Two-soliton solutions

The quantities $\int_0^t \mathrm{d}t'\, \partial_{t'} Q^{(-3)}$ and $\partial_t Q^{(-3)}$ presented in figure 6.11 correspond to the two-soliton simulation perturbed through $\chi_2 = 0.5$ (see figure 5.9). These figures show that initially, the value of $\int_0^t \mathrm{d}t'\, \partial_{t'} Q^{(-3)}$ changes rapidly (i.e., when the soliton- and radiation-like components separate from each other), and then from $t \sim 5$ to $t \sim 9$ the value stabilises (i.e., when there are no interactions between the various soliton- and radiation-like components). Subsequently, the value of $\int_0^t \mathrm{d}t'\, \partial_{t'} Q^{(-3)}$

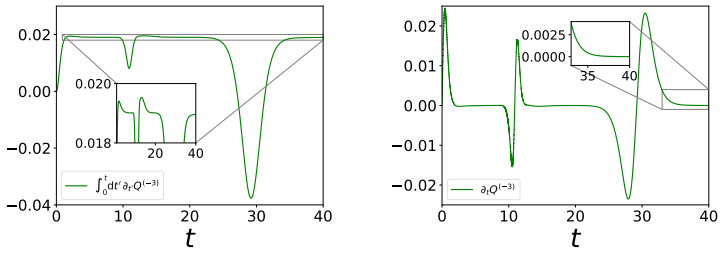

(a) (b)

Figure 6.11: The green curves in figures (a) and (b) show the time-dependence of the quantities $\int_0^t \mathrm{d}t'\, \partial_{t'} Q^{(-3)}$ and $\partial_t Q^{(-3)}$ for the numerical mRLW two-soliton solution perturbed through $\chi_1 = 0$ and $\chi_2 = 0.5$, as presented by the green curves in figure 5.9.

starts to decrease at $t \sim 9$ (i.e., when the largest soliton-like field starts to interact with the radiation emitted by the smallest initial soliton, see for instance figure 5.9c). Next, the value of $\int_0^t \mathrm{d}t' \, \partial_{t'} Q^{(-3)}$ returns to its original value at $t \sim 18$ (i.e., when the soliton-like structure separates from the radiation-like component). Finally, we see that $\int_0^t \mathrm{d}t' \, \partial_{t'} Q^{(-3)}$ changes again during the interaction between the two soliton-like structures, and then returns to its original value after the interaction.

The quantities $\int_0^t \mathrm{d}t' \, \partial_{t'} Q^{(-3)}$ and $\partial_t Q^{(-3)}$ corresponding to $\chi_2 = -0.5$ (see figure 5.10) are shown in figure 6.12. Again, we see that $\int_0^t \mathrm{d}t' \, \partial_{t'} Q^{(-3)}$ only changes initially when the soliton- and radiation-like components separate from each other, and during interactions between these components.

Figures 6.13 displays the values of $\int_0^t \mathrm{d}t' \, \partial_{t'} Q^{(-3)}$ and $\partial_t Q^{(-3)}$ related to the simulation shown in figure 5.11 (i.e., $\chi_1 = 0.5$ and $\chi_2 = 0$), and figure 6.14 shows the values of $\int_0^t \mathrm{d}t' \, \partial_{t'} Q^{(-3)}$ and $\partial_t Q^{(-3)}$ corresponding to figure 5.12 (i.e., $\chi_1 = -0.5$ and $\chi_2 = 0$). Thus, just as for the two-soliton simulations perturbed through χ_2, the value of $\int_0^t \mathrm{d}t' \, \partial_{t'} Q^{(-3)}$ rapidly changes initially and during the interactions. However, the quasi-integrability properties of the perturbation through χ_1 is different, because $\int_0^t \mathrm{d}t' \, \partial_{t'} Q^{(-3)}$ also changes slowly when all the soliton- and radiation-like components are far away from each other, as shown in the insets in figures 6.13a and 6.14a.

The results presented in this subsection are consistent with the results discussed in the previous subsection. We found that for the one- and two-soliton solutions

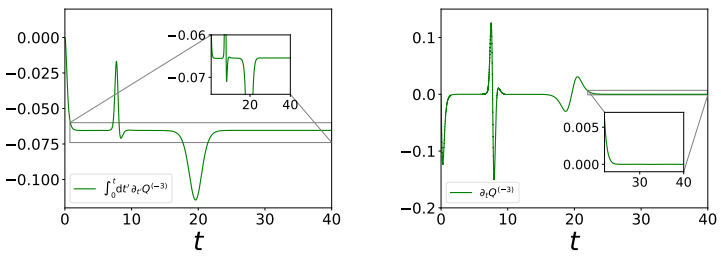

(a) (b)

Figure 6.12: The green curves in figures (a) and (b) show the time-dependence of the quantities $\int_0^t \mathrm{d}t' \, \partial_{t'} Q^{(-3)}$ and $\partial_t Q^{(-3)}$ for the numerical mRLW two-soliton solution perturbed through $\chi_1 = 0$ and $\chi_2 = -0.5$, as presented by the green curves in figure 5.10.

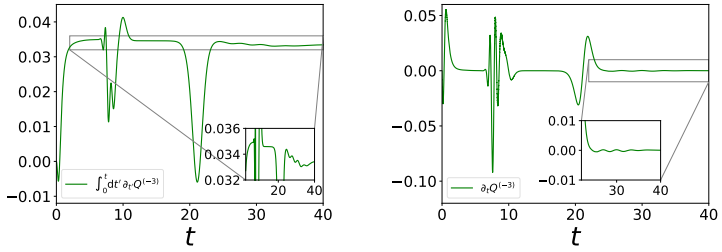

(a) (b)

Figure 6.13: The green curves in figures (a) and (b) show the time-dependence of the quantities $\int_0^t \mathrm{d}t'\, \partial_{t'} Q^{(-3)}$ and $\partial_t Q^{(-3)}$ for the numerical mRLW two-soliton solution perturbed through $\chi_1 = 0.5$ and $\chi_2 = 0$, as presented by the green curves in figure 5.11.

perturbed through $\chi_2 = 0.5$ and $\chi_2 = -0.5$, the value of $\int_0^t \mathrm{d}t'\, \partial_{t'} Q^{(-3)}$ changes for the following two reasons:

(i) immediately at the start of the simulation, i.e., when the soliton-like structures separate from their radiation-like components,

(ii) and during interactions between soliton-like components and other soliton- or radiation-like components.

Furthermore, we saw that the value of $\int_0^t \mathrm{d}t'\, \partial_{t'} Q^{(-3)}$ always approaches some constant value when the soliton-like structures are not interacting with any other soliton- or radiation-like components. On the other hand, for the one- and two-soliton simulations perturbed through $\chi_1 = 0.5$ and $\chi_1 = -0.5$, the value of $\int_0^t \mathrm{d}t'\, \partial_{t'} Q^{(-3)}$ also varies with time when the different components are not interacting with each

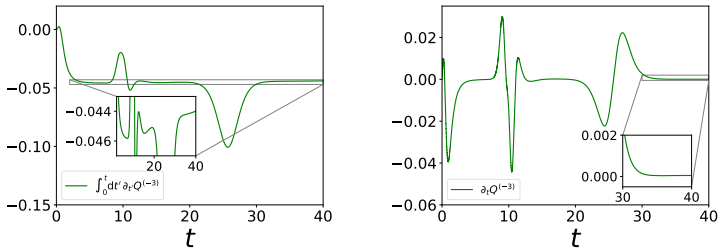

(a) (b)

Figure 6.14: The green curves in figures (a) and (b) show the time-dependence of the quantities $\int_0^t \mathrm{d}t'\, \partial_{t'} Q^{(-3)}$ and $\partial_t Q^{(-3)}$ for the numerical mRLW two-soliton solution perturbed through $\chi_1 = -0.5$ and $\chi_2 = 0$, as presented by the green curves in figure 5.12.

other. We have also observed this for various other values of χ_1 and χ_2, and found similar results.

6.3.3 Three-soliton solutions

Let us now discuss the quasi-integrability properties of the three-soliton simulations presented in subsection 5.1.3. Figures 6.15, 6.16, 6.17 and 6.18 show the time-dependence of $\int_0^t \mathrm{d}t' \, \partial_{t'} Q^{(-3)}$ and $\partial_t Q^{(-3)}$ for the perturbed three-soliton simulations, as shown in figures 5.13, 5.14, 5.15 and 5.16, respectively. Looking at figure 6.15 (perturbed through $\chi_2 = 0.5$), we see that the value of $\int_0^t \mathrm{d}t' \, \partial_{t'} Q^{(-3)}$ initially increases, and then stabilises. Subsequently, $\int_0^t \mathrm{d}t' \, \partial_{t'} Q^{(-3)}$ only changes during the interactions of soliton-like structures and other soliton- and radiation-like components. We see similar behaviour for the quantities $\int_0^t \mathrm{d}t' \, \partial_{t'} Q^{(-3)}$ and $\partial_t Q^{(-3)}$ shown in figure 6.16 (i.e., the simulation with $\chi_2 = -0.5$). On the other hand, the insets in figures 6.17 and 6.18 (i.e., the simulations with $\chi_1 = 0.5$ and $\chi_1 = -0.5$) show that $\int_0^t \mathrm{d}t' \, \partial_{t'} Q^{(-3)}$ changes slowly even when there are no interactions. This is consistent with the results we have seen in the previous two subsections.

To sum up the results of this section, for the two- and three-soliton models perturbed through $\chi_2 = 0.5$ and $\chi_2 = -0.5$, we have seen that the charges $Q^{(-3)}$ are quasi-conserved during interactions between soliton-like structures with other soliton- and radiation-like components. This is the behaviour we would expect from

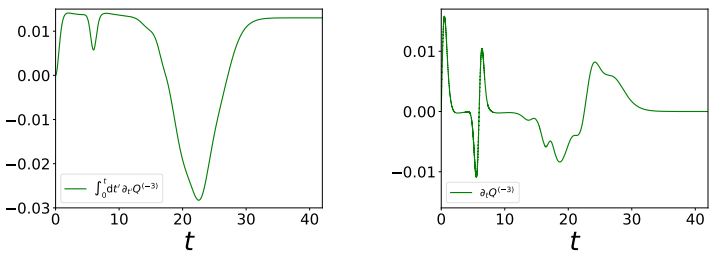

(a) (b)

Figure 6.15: The green curves in figures (a) and (b) show the time-dependence of the quantities $\int_0^t \mathrm{d}t' \, \partial_{t'} Q^{(-3)}$ and $\partial_t Q^{(-3)}$ for the numerical mRLW three-soliton solution perturbed through $\chi_1 = 0$ and $\chi_2 = 0.5$, as presented by the green curves in figure 5.13.

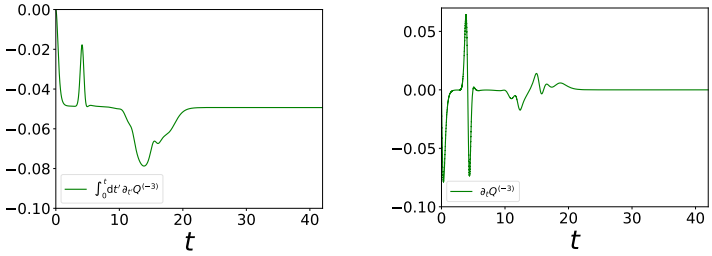

(a) (b)

Figure 6.16: The green curves in figures (a) and (b) show the time-dependence of the quantities $\int_0^t \mathrm{d}t'\, \partial_{t'} Q^{(-3)}$ and $\partial_t Q^{(-3)}$ for the numerical mRLW three-soliton solution perturbed through $\chi_1 = 0$ and $\chi_2 = -0.5$, as presented by the green curves in figure 5.14.

quasi-integrable models. However, this perturbed model is different because $Q^{(-3)}$ initially increases or decreases until the solitons in the initial configuration (i.e., the initial conditions) have emitted some radiation-like component, and so we do not know if equation (1.4.2) is satisfied. Only when the resulting soliton- and radiation-like structures have moved away from each other (i.e. they cease to interact), the quantity $Q^{(-3)}$ stabilises to some constant value. Subsequently, as mentioned, $Q^{(-3)}$ only changes during interactions between the various soliton-like and radiation-like components; and after these interactions, $Q^{(-3)}$ returns to the same value it had before the interactions.

These results suggest that each initial soliton, which is given by the initial conditions, forms an interaction between some (numerical) one-soliton solution of the perturbed model and some radiation-like component. Subsequently, following

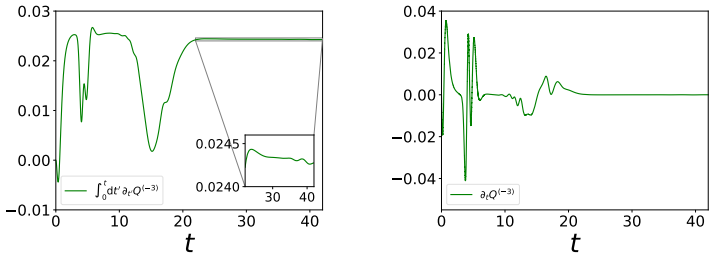

(a) (b)

Figure 6.17: The green curves in figures (a) and (b) show the time-dependence of the quantities $\int_0^t \mathrm{d}t'\, \partial_{t'} Q^{(-3)}$ and $\partial_t Q^{(-3)}$ for the numerical mRLW three-soliton solution perturbed through $\chi_1 = 0.5$ and $\chi_2 = 0$, as presented by the green curves in figure 5.15.

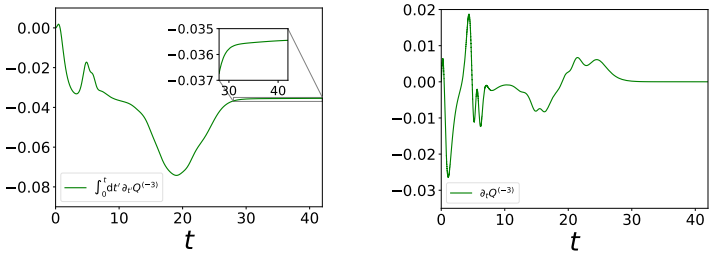

(a) (b)

Figure 6.18: The green curves in figures (a) and (b) show the time-dependence of the quantities $\int_0^t \mathrm{d}t'\, \partial_{t'} Q^{(-3)}$ and $\partial_t Q^{(-3)}$ for the numerical mRLW three-soliton solution perturbed through $\chi_1 = -0.5$ and $\chi_2 = 0$, as presented by the green curves in figure 5.16.

off this assumption, one might deduce that as $t \to -\infty$, the value of $Q^{(-3)}$ returns to the same aforementioned constant, and so equation (1.4.2) would be satisfied. However, more work has to be done to investigate this conjecture.

6.4 Perturbed RLW solutions

Let us now briefly discuss the quasi-integrability properties of the perturbed RLW simulations presented in section 5.2. We found that the properties of these systems are very similar to the results discussed in the previous section. Therefore, for brevity, we only discuss the one-soliton simulations.

Namely, figure 6.19 shows the time-dependence of $\int_0^t \mathrm{d}t'\, \partial_{t'} Q^{(-3)}$ and $\partial_t Q^{(-3)}$ related to the simulation shown in figures 5.17a to 5.17c (i.e., $\varepsilon_2 = 0.5$). This shows

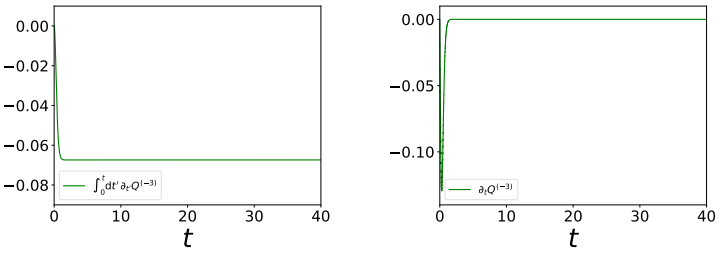

(a) (b)

Figure 6.19: The green curves in figures (a) and (b) show the time-dependence of the quantities $\int_0^t \mathrm{d}t'\, \partial_{t'} Q^{(-3)}$ and $\partial_t Q^{(-3)}$ for the numerical RLW one-soliton solution perturbed through $\chi_1 = 0$ and $\varepsilon_2 = 0.5$, as presented by the green curves in figures 5.17a to 5.17c.

that the value of $\int_0^t \mathrm{d}t' \, \partial_{t'} Q^{(-3)}$ only changes initially when the initial soliton splits up in a soliton-like and a radiation-like component. After they cease interacting with each other, the value approaches a constant value. Similarly, figure 6.20 shows the time-dependence of $\int_0^t \mathrm{d}t' \, \partial_{t'} Q^{(-3)}$ and $\partial_t Q^{(-3)}$ related to the simulation shown in figures 5.17d to 5.17f (i.e., $\varepsilon_2 = -0.5$). We again see that $\int_0^t \mathrm{d}t' \, \partial_{t'} Q^{(-3)}$ only changes initially, and subsequently stabilises when the soliton-like structure has moved away from the radiation-like component.

Next, we focus on the two one-soliton RLW simulations perturbed through χ_1, as shown in figure 5.19. To be specific, figure 6.21 shows the time-dependence of $\int_0^t \mathrm{d}t' \, \partial_{t'} Q^{(-3)}$ and $\partial_t Q^{(-3)}$ related to the simulation perturbed through $\chi_1 = 0.5$, and figure 6.22 shows the time-dependence of $\int_0^t \mathrm{d}t' \, \partial_{t'} Q^{(-3)}$ and $\partial_t Q^{(-3)}$ related to the simulation perturbed through $\chi_1 = -0.5$. We see that the value of $\int_0^t \mathrm{d}t' \, \partial_{t'} Q^{(-3)}$ for both simulations changes quite rapidly initially, i.e., when the initial soliton splits up into a soliton- and radiation-like structure. However, even after the components have moved away from each other, the value of $\int_0^t \mathrm{d}t' \, \partial_{t'} Q^{(-3)}$ changes slowly. This is similar to the mRLW solitons perturbed through χ_1, as discussed in the previous section.

Armed with these observations, we found that the quasi-integrability properties of the multi-soliton simulations presented in subsections 5.2.2 and 5.2.3 are as expected. That is, for the simulations perturbed through $\varepsilon_2 = 0.5$ and $\varepsilon_2 = -0.5$, the value of

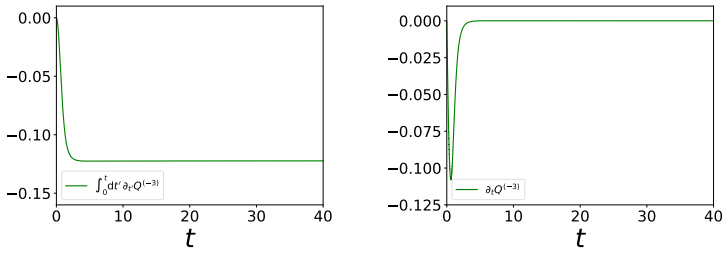

(a) (b)

Figure 6.20: The green curves in figures (a) and (b) show the time-dependence of the quantities $\int_0^t \mathrm{d}t' \, \partial_{t'} Q^{(-3)}$ and $\partial_t Q^{(-3)}$ for the numerical RLW one-soliton solution perturbed through $\chi_1 = 0$ and $\varepsilon_2 = -0.5$, as presented by the green curves in figures 5.17d to 5.17f.

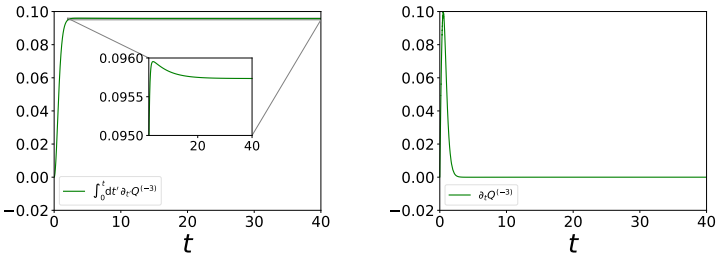

(a) (b)

Figure 6.21: The green curves in figures (a) and (b) show the time-dependence of the quantities $\int_0^t dt' \, \partial_{t'} Q^{(-3)}$ and $\partial_t Q^{(-3)}$ for the numerical RLW one-soliton solution perturbed through $\chi_1 = 0.5$ and $\varepsilon_2 = 0$, as presented by the green curves in figures 5.19a to 5.19c.

$\int_0^t dt' \, \partial_{t'} Q^{(-3)}$ only changes initially and during the interactions between the various soliton- and radiation-like structures. For the simulations perturbed through $\chi_1 = 0.5$ and $\chi_1 = -0.5$, we found that the value of $\int_0^t dt' \, \partial_{t'} Q^{(-3)}$ additionally changes when the various soliton- and radiation-like structures are not interacting with each other.

Thus, we see that the RLW simulations perturbed through ε_2 share similar quasi-integrability properties as the mRLW simulations perturbed through χ_2, and the RLW simulations perturbed through χ_1 share similar quasi-integrability properties as the mRLW simulations perturbed through χ_1. Just as for the perturbed mRLW simulations, it will be interesting to study the time evolution of the perturbed RLW simulations as $t \to -\infty$. This will allow us to test if equation (1.4.2) is satisfied for the perturbations through ε_2.

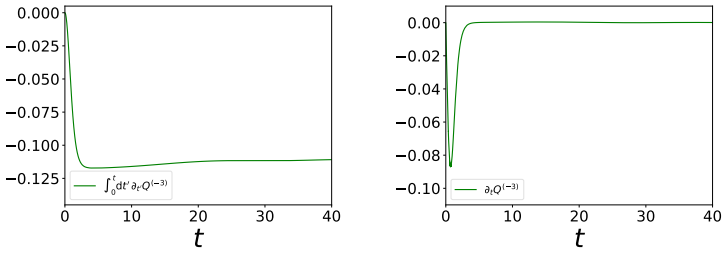

(a) (b)

Figure 6.22: The green curves in figures (a) and (b) show the time-dependence of the quantities $\int_0^t dt' \, \partial_{t'} Q^{(-3)}$ and $\partial_t Q^{(-3)}$ for the numerical RLW one-soliton solution perturbed through $\chi_1 = -0.5$ and $\varepsilon_2 = 0$, as presented by the green curves in figures 5.19d to 5.19f.

Chapter 7

Conclusions and future work

In this thesis, we investigated the integrability properties of the perturbed KdV equation, which includes the RLW and mRLW equations as special cases. In chapter 2, we introduced the anomalous curvature equation, which is based on the same Lax potential A_x that is used to construct the well-known infinite amount of conserved charges for the KdV equation. This anomalous curvature equation results in an infinite amount of potentially quasi-conserved quantities $Q^{(-2n-1)}$ for the perturbed KdV equation. Using parity arguments, we proved that these quantities are truly quasi-conserved for the exact mRLW two-soliton solutions, which is the first analytic proof of quasi-integrability for any family of two-soliton solutions.

In section 2.5, we showed that the analytical KdV two- and three-soliton solutions are even under the space-time parity operator, provided that the (three) solitons scatter at the same point in space-time. Furthermore, in section 2.6, we argued that an expansion of the u-field around some exact KdV solution preserves quasi-integrability, on the assumption that u solves the perturbed KdV equation and that the exact KdV solution is even under the space-time operator. This seems to suggest that the perturbed KdV model in some sense favours solutions that satisfy the quasi-conservation laws. It will be interesting to develop a method in the future that allows us to test this conjecture.

Next, we developed a first- and second-order finite difference scheme to numeric-

ally investigate the perturbed KdV model. The schemes involve implicit methods that are based on the algorithms discussed in [7], where we appropriately adapted them to solve the perturbed KdV equation. These schemes have been extensively tested by comparing numerical soliton solutions with their corresponding analytical values. The results for the second-order scheme showed that they were essentially indistinguishable, which reassured us that the numerical simulations could be trusted.

We then used this scheme to simulate three-soliton configurations governed by the mRLW equation. We found that the three solitons evolve smoothly and do not emit any visible radiation. Furthermore, they re-emerge from the three-soliton interaction with the same initial shape and velocity. In fact, the only noticeable result of the three-soliton interaction is the phase shift that each soliton experiences, which is equal (within a numerical error of less than 6%) to the sum of pairwise phase shifts. Thus, these numerical solutions appear to share many of the same properties that integrable solitons possess.

Furthermore, we used the second-order scheme to study the time evolution of mRLW soliton solutions in the presence of external perturbing terms. Provided the perturbations are small enough, the perturbed systems resulted in long-lived localised structures, which can be interpreted as soliton-like components, with additional radiation-like components. This indicates that the mRLW solitons are very stable, which is another feature the model shares with integrable systems.

Thus, both the perturbed and unperturbed mRLW systems share many features of integrable solitons. To further investigate this, we numerically evolved an arbitrary initial pulse with finite energy to test the soliton resolution conjecture. We found that the system blows up, and so the conjecture does not hold for the mRLW equation. Numerically, this is the only property of this partial integrable model whose behaviour differs from integrable models such as the KdV equation.

For future work, it would therefore be interesting to study other nonintegrable systems which do not possess a Hamiltonian structure but do admit one- and two-soliton Hirota solutions. One could test if such systems admit numerical three-soliton

configurations in which the time-evolved solitons behave similar to integrable solitons, and also test the soliton resolution conjecture. This could shine new light on the connection between (Hirota) integrability and the soliton resolution conjecture.

We have performed the same tests with the RLW model. Since the RLW equation only admits one-soliton solutions, we investigated the two- and three-soliton RLW configurations. The simulations showed that the solitons emit a small amount of visible radiation when they scatter. Furthermore, for the three-soliton interactions, the phase shift that each numerical soliton experiences is not equal to the sum of the pairwise phase shifts. Simulating RLW soliton configurations in the presence of perturbing terms showed that they resulted in soliton- and radiation-like components, similar to the perturbed mRLW solutions. On the other hand, we found that the time evolution of various arbitrary initial pulses did not blow up, which suggests that the soliton resolution conjecture may hold for the RLW equation. To sum up, we see that the numerical results for the RLW simulations are significantly different than for the mRLW simulations.

We also numerically calculated various $Q^{(-2n-1)}$ quantities for all of the aforementioned simulations to investigate their quasi-integrability properties. We found that the $Q^{(-3)}$ quantity is quasi-conserved for both the two- and three-soliton solutions governed by the mRLW equation. Moreover, $Q^{(-3)}$ is also quasi-conserved for the RLW two- and three-soliton simulations. These numerical results are the strongest support for our working definition of quasi-integrability. Namely, we observed that $Q^{(-3)}$ only changes value when the solitons scatter with each other, and remains constant when the solitons are far away from each other. This behaviour has also been observed for other (quasi-integrable) models.

To our knowledge, this is the first time that the quasi-integrability properties of three-soliton interactions have been investigated. Note that the parity argument for three-soliton solutions is much more involved. Since we observed that $Q^{(-3)}$ is quasi-conserved for two-soliton interactions, we would expect $Q^{(-3)}$ to also be quasi-conserved when three solitons scatter pairwise. However, when the three solitons

scatter with each other at the same time, we cannot make this assumption due to the possible 'many-particle' effects.

Furthermore, we investigated the quasi-integrability properties of the aforementioned perturbed simulations. For both the mRLW and RLW simulations perturbed through ε_2, we observed that $Q^{(-3)}$ changes at the start of the simulation, i.e., when the soliton- and radiation-like components separate from each other. Subsequently, after this initial change in the value of $Q^{(-3)}$, it appears that the system is quasi-integrable in the sense that the value of $Q^{(-3)}$ only changes when the various structures scatter with each other; and after such an interaction, it returns to the same value it had before the scattering. In other words, the results show that the soliton-radiation interactions respect our working definition of quasi-integrability. This raises the question if we can consider the initial solitons, i.e., the initial conditions, as the interaction of some (numerical) soliton-like solution with some additional radiation-like components. Assuming this is true, we would expect that equation (1.4.2) is satisfied. Therefore, we can test this conjecture by developing an algorithm that allows us to run simulations backwards in time in order to determine the time-dependence of $Q^{(-3)}$ as $t \to -\infty$. Finally, note that since the usual parity arguments do not apply to such an interaction, at this stage we do not understand why quasi-integrability is respected for such soliton-radiation interactions.

Finally, note that the finite difference methods as discussed in chapter 3 approximate equation (1.3.23), which we use to calculate the u-field (see equation (1.3.21)). This implies that we cannot use these methods to simulate an exact KdV soliton solution that is governed by the KdV equation in the presence of additional perturbing terms. We believe that it might be fruitful to investigate the quasi-integrability properties of such perturbed simulations in the future.

Appendix A

Simulation parameters

Tables A.1 to A.11 summarise the values of the parameters that were used to produce the simulations that are presented in this thesis.

Table A.1: Summary of the parameters used to produce figure 2.1, and figures 3.1 to 3.4.

	Figure 2.1	Figures 3.1 and 3.3	Figures 3.2 and 3.4
α	8	8	8
ε_1	1	1	1
ε_2	1	1	1
x_0	98.9	-50	-50
x_N	168.9	300	300
h	N/A	0.1	0.1
t_0	18.9	0	0
t_K	28.9	40	40
τ	N/A	0.001	0.001
ω_1	5.00	5.00	5.00
δ_1	0.00	0.00	0.00
ω_2	3.00	N/A	3.00
δ_2	-40.00	N/A	-40.00

Table A.2: Summary of the parameters used to produce figures 4.1, 4.3 and 4.5.

	Figure 4.1 (red curve)	Figure 4.3	Figure 4.5
α	8	8	8
ε_1	1	1	1
ε_2	1	1	1
x_0	-50	-220	-125
x_N	300	250	175
h	0.1	0.1	0.1
t_0	0	0	0
t_K	40	170	42
τ	0.001	0.001	0.001
ω_1	5.00	0.80	0.80
δ_1	0.00	66.51	16.63
ω_2	3.00	1.33	3.07
δ_2	-43.63	110.90	63.77
ω_3	N/A	1.84	4.28
δ_3	N/A	152.88	89.00

Table A.3: Summary of the parameters used to produce figure 4.7, and figures 4.10 to 4.12.

	Figure 4.7	Figure 4.10	Figure 4.11	Figure 4.12
α	8	8	8	8
ε_1	1	1	1	1
ε_2	0	0	0	1
x_0	-50	-220	-125	-150
x_N	300	400	175	350
h	0.1	0.1	0.1	0.1
t_0	0	0	0	1
t_K	40	170	42	81
τ	0.001	0.001	0.001	0.001
ω_1	5.00	0.80	0.80	N/A
δ_1	0.00	66.51	16.63	N/A
ω_2	3.00	1.33	3.07	N/A
δ_2	-43.63	110.90	63.77	N/A
ω_3	N/A	1.84	4.28	N/A
δ_3	N/A	152.88	89.00	N/A

Table A.4: Summary of the parameters used to produce the three simulations shown in figure 5.1.

	Figures 5.1a to 5.1c	Figures 5.1d to 5.1f	Figures 5.1g to 5.1i
α	8	8	8
ε_1	1	1	1
ε_2	0.9	0.3	0
x_0	-50	-50	-50
x_N	300	300	300
h	0.1	0.1	0.1
t_0	0	0	0
t_K	40	40	40
τ	0.001	0.001	0.001
ω_1	5.00	5.00	5.00
δ_1	0.00	0.00	0.00

Table A.5: Summary of the parameters used to produce figures 5.3, 5.5 and 5.6.

	Figure 5.3	Figure 5.5	Figure 5.6
α	8	8	8
ε_1	1	1	1
ε_2	0.5	1.5	1.9
x_0	-50	-50	-350
x_N	300	300	400
h	0.1	0.1	0.1
t_0	0	0	0
t_K	40	40	40
τ	0.001	0.001	0.001
ω_1	5.00	5.00	5.00
δ_1	0.00	0.00	0.00

Table A.6: Summary of the parameters used to produce figures 5.7, 5.9 and 5.10.

	Figures 5.7a to 5.7c	Figures 5.7d to 5.7f	Figure 5.9	Figure 5.10
α	8	8	8	8
ε_1	0.5	1.5	1	1
ε_2	1	1	0.5	1.5
x_0	-100	-50	-50	-50
x_N	300	300	300	300
h	0.1	0.1	0.1	0.1
t_0	0	0	0	0
t_K	40	40	40	40
τ	0.001	0.001	0.001	0.001
ω_1	5.00	5.00	5.00	5.00
δ_1	0.00	0.00	0.00	0.00
ω_2	N/A	N/A	3.00	3.00
δ_2	N/A	N/A	-40.00	-40.00

Table A.7: Summary of the parameters used to produce figures 5.11 to 5.15.

	Figure 5.11	Figure 5.12	Figure 5.13	Figure 5.14	Figure 5.15
α	8	8	8	8	8
ε_1	0.5	1.5	1	1	0.5
ε_2	1	1	0.5	1.5	1
x_0	-50	-50	-125	-125	-225
x_N	300	300	275	275	275
h	0.1	0.1	0.1	0.1	0.1
t_0	0	0	0	0	0
t_K	40	40	42	42	42
τ	0.001	0.001	0.001	0.001	0.001
ω_1	5.00	5.00	0.80	0.80	0.80
δ_1	0.00	0.00	16.63	16.63	16.63
ω_2	3.00	3.00	3.07	3.07	3.07
δ_2	-40.00	-40.00	63.77	63.77	63.77
ω_3	N/A	N/A	4.28	4.28	4.28
δ_3	N/A	N/A	89.00	89.00	89.00

Table A.8: Summary of the parameters used to produce figures 5.16 and 5.17.

	Figure 5.16	Figures 5.17a to 5.17c	Figures 5.17d to 5.17f
α	8	8	8
ε_1	1.5	1	1
ε_2	1	0.5	-0.5
x_0	-125	-50	-50
x_N	275	300	300
h	0.1	0.1	0.1
t_0	0	0	0
t_K	42	40	40
τ	0.001	0.001	0.001
ω_1	0.80	5.00	5.00
δ_1	16.63	0.00	0.00
ω_2	3.07	N/A	N/A
δ_2	63.77	N/A	N/A
ω_3	4.28	N/A	N/A
δ_3	89.00	N/A	N/A

Table A.9: Summary of the parameters used to produce figures 5.19, 5.21 and 5.22.

	Figures 5.19a to 5.19c	Figures 5.19d to 5.19f	Figure 5.21	Figure 5.22
α	8	8	8	8
ε_1	0.5	1.5	1	1
ε_2	0	0	0.5	-0.5
x_0	-50	-50	-50	-50
x_N	300	300	400	300
h	0.1	0.1	0.1	0.1
t_0	0	0	0	0
t_K	40	40	40	40
τ	0.001	0.001	0.001	0.001
ω_1	5.00	5.00	5.00	5.00
δ_1	0.00	0.00	0.00	0.00
ω_2	N/A	N/A	3.00	3.00
δ_2	N/A	N/A	-43.63	-43.63

Table A.10: Summary of the parameters used to produce figures 5.23 to 5.27.

	Figure 5.23	Figure 5.24	Figure 5.25	Figure 5.26	Figure 5.27
α	8	8	8	8	8
ε_1	0.5	1.5	1	1	0.5
ε_2	0	0	0.5	-0.5	0
x_0	-50	-50	-125	-125	-125
x_N	300	300	275	175	175
h	0.1	0.1	0.1	0.1	0.1
t_0	0	0	0	0	0
t_K	40	40	42	42	42
τ	0.001	0.001	0.001	0.001	0.001
ω_1	5.00	5.00	0.80	0.80	0.80
δ_1	0.00	0.00	16.63	16.63	16.63
ω_2	3.00	3.00	3.07	3.07	3.07
δ_2	-43.63	-43.63	63.77	63.77	63.77
ω_3	N/A	N/A	4.28	4.28	4.28
δ_3	N/A	N/A	89.00	89.00	89.00

Table A.11: Summary of the parameters used to produce figure 5.28.

	Figure 5.28
α	8
ε_1	1.5
ε_2	0
x_0	-125
x_N	175
h	0.1
t_0	0
t_K	42
τ	0.001
ω_1	0.80
δ_1	16.63
ω_2	3.07
δ_2	63.77
ω_3	4.28
δ_3	89.00

Bibliography

[1] Ablowitz, M. J., and H. Segur. 1981. *Solitons And The Inverse Scattering Transform*. SIAM.

[2] Benjamin, T. B., J. L. Bona, and J. J. Mahony. 1972. "Model equations for long waves in nonlinear dispersive systems", *Philosophical Transactions Of The Royal Society A: Mathematical, Physical And Engineering Sciences* 272 (1220): 47-78.

[3] Bona, J. L., W. G. Pritchard, and L. R. Scott. 1980. "Solitary-Wave Interaction". Physics Of Fluids 23 (3): 438-441.

[4] ter Braak, F., L. A. Ferreira, and W. J. Zakrzewski. 2017. "Quasi-integrability of deformations of the KdV equation". arXiv:1710.00918 [hep-th].

[5] ter Braak, F., and W. J. Zakrzewski. 2017. "Aspects of the modified regularized long-wave equation". arXiv:1707.00669 [nlin.PS].

[6] Bryan, A. C., and A. E. G. Stuart. 1996. "Solitons And The Regularized Long Wave Equation: A Nonexistence Theorem". *Chaos, Solitons & Fractals* 7 (11): 1881-1886.

[7] Eilbeck, J. C., and G. R. McGuire. 1975. "Numerical Study Of The Regularized Long-Wave Equation I: Numerical Methods". *Journal Of Computational Physics* 19 (1): 43-57.

[8] Eilbeck, J. C., and G. R. McGuire. 1977. "Numerical Study Of The Regularized Long-Wave Equation. II: Interaction Of Solitary Waves". *Journal Of Computational Physics* 23 (1): 63-73.

[9] Faddeev, L. D., and L. A. Tachtadžjan. 1987. *Hamiltonian Methods In The Theory Of Solitons*. Springer.

[10] Faddeev, L. D., and V. E. Zakharov. 1972. "Korteweg-De Vries Equation: A Completely Integrable Hamiltonian System". *Functional Analysis And Its Applications* 5 (4): 280-287. [In English.]

[11] Ferreira, L. A., G. Luchini, and W. J. Zakrzewski. 2013. "The Concept Of Quasi-Integrability". *AIP Conference Proceedings* 1562 (1): 43-49.

[12] Ferreira, L. A., and W. J. Zakrzewski. 2011. "The Concept Of Quasi-Integrability: A Concrete Example". *Journal Of High Energy Physics* 2011 (5).

[13] Ferreira, L. A., and W. J. Zakrzewski. 2014. "Numerical And Analytical Tests Of Quasi-Integrability In Modified Sine-Gordon Models". *Journal Of High Energy Physics* 2014 (1).

[14] Gardner, C. S., J. M. Greene, M. D. Kruskal, and R. M. Miura. 1967. "Method For Solving The Korteweg-Devries Equation". *Physical Review Letters* 19 (19): 1095-1097.

[15] Gibbon, J. D., J. C. Eilbeck, and R. K. Dodd. 1976. "A Modified Regularized Long-Wave Equation With An Exact Two-Soliton Solution". *Journal Of Physics A: Mathematical And General* 9 (10): L127-L130.

[16] Hietarinta, J. 2002. "Scattering of solitons and dromions". In *Scattering*. Academic Press.

[17] Hietarinta, J. 2009. "Hirota's Bilinear Method and Its Connection with Integrability". In *Integrability*. Springer Berlin Heidelberg.

[18] Hirota, R. 2004. *The Direct Method in Soliton Theory*. Cambridge University Press.

[19] Korteweg, D. J., and G. de Vries. 1895. "On The Change Of Form Of Long Waves Advancing In A Rectangular Canal, And On A New Type Of Long Stationary Waves". *Philosophical Magazine Series 5* 39 (240): 422-443.

[20] Kutluay, S., and A. Esen. 2006. "A Finite Difference Solution Of The Regularized Long-Wave Equation". *Mathematical Problems In Engineering* 2006: 1-14.

[21] Kruskal, M. D., and N. J. Zabusky. 1965. "Interaction Of "Solitons" In A Collisionless Plasma And The Recurrence Of Initial States". *Physical Review Letters* 15 (6): 240-243.

[22] Manakov, S. V., S. Novikov, L. P. Pitaevskii, and V. E. Zakharov. 1984. *Theory Of Solitons*. Consultants Bureau.

[23] Olver, P. J. 1979. "Euler Operators And Conservation Laws Of The BBM Equation". *Mathematical Proceedings Of The Cambridge Philosophical Society* 85 (01): 143.

[24] Peregrine, D. H. 1966. "Calculations Of The Development Of An Undular Bore". *Journal Of Fluid Mechanics* 25 (02): 321.

[25] Schay, G. 2012. *A Concise Introduction To Linear Algebra*. Birkhäuser Boston.

[26] Soomere, T. 2009. "Solitons Interactions". In *Mathematics Of Complexity And Dynamical Systems*. Springer New York.

[27] Tao, T. 2008. "Why Are Solitons Stable?". *Bulletin Of The American Mathematical Society* 46 (1): 1-33.

[28] Yang, J. 2010. *Nonlinear Waves In Integrable And Nonintegrable Systems*. Philadelphia, Pa.: Society for Industrial and Applied Mathematics.